Université catholique de Louvain
École polytechnique de Louvain
Institut de Mécanique, Matériaux et génie Civil

Finite element modeling of sediment dynamics in the Scheldt

Doctoral dissertation presented by

Olivier Gourgue

in partial fulfillment of the requirements for the degree of

Docteur en Sciences de l'Ingénieur

Thesis committee :

Pr Willy Baeyens, Vrije Universiteit Brussel
Pr Eric Deleersnijder, Université catholique de Louvain (Advisor)
Pr Eric Delhez, Université de Liège
Pr Marc Elskens, Vrije Universiteit Brussel
Pr Thierry Fichefet, Université catholique de Louvain
Pr Vincent Legat, Université catholique de Louvain (Advisor)
Pr Thomas Pardoen, Université catholique de Louvain (President)

Louvain-la-Neuve, 9 December 2011

Contents

Chapter 1

Introduction

1.1 Motivations

Estuaries and continental shelf areas comprise 5.2 % of the Earth's surface, and only 0.2 % of the oceans' volume. However, throughout human history, estuaries and coasts have been among the most populated areas of the world (60 % of the world's population at present). This is because people used them as transport routes, and because of their high biological productivity sustaining a high level of food production (Wolanski, 2007). As a consequence, these areas were the place for an important development of industrial, farming and fishing activities, putting a hard pressure on the environment. To take advantage of the local resources, both inland and into the sea, is the main reason why people settled there. Therefore, understanding the estuarine and coastal phenomena, as the influence of human activities on them, is of crucial importance to preserve these resources.

The Scheldt Estuary (Figure 1.1) is a good illustration of that, as the river takes its source in France and flows through Belgium and the Netherlands, the two most densely populated countries of Western Europe, before discharging into the North Sea near Vlissingen. Its catchment basin comprises some important cities such as Brussels, Antwerp, Ghent and Lille. In total, more than 10 millions inhabitants pour out their waste water into the Scheldt. Moreover, an important source of

Figure 1.1: Coastal water entities from South to North : the Western Scheldt (simply called the Scheldt Estuary in this thesis), the Eastern Scheldt (not connected to any continental river anymore) and the Rhine/Meuse Delta.

pollution is the considerable and direct supply of toxic non-organic pollutants occurring as a result of the diverse activities by the industrial areas concentrated near Lille, Antwerp, along the canal from Ghent to Terneuzen, and near Vlissingen.

The Scheldt Estuary is known to be highly polluted by industrial and domestic waste waters, containing suspended matter that are among others enriched by trace metals (De Smedt et al., 1998). Pollution by toxic metals is one of the major threats to the estuarine ecosystem. Concentrations of dissolved trace metals are about two times higher than in the marine water mass of the Belgian coastal zone, and an order of magnitude higher than ocean values (Baeyens et al., 1998c). Trace metals exist in two phases in estuarine waters: the dissolved phase and the particulate phase adsorbed on sediments. Contaminated sediments are a threat to the aquatic environment and ecosystem since their resuspension, caused by strong tidal currents or dredging operations, releases a significant amount of trace metals into the water column (Baeyens et al.,

1998a). A better understanding of the trace metal dynamics, with emphasis on the basic governing processes is therefore essential to protect the high species diversity of the estuary and its valuable natural areas, some of which are protected.

In 2007, the interdisciplinary network TIMOTHY[1] started with the aim to study the modifications of the Scheldt Basin system in response to natural and anthropogenic changes. The role of our team is to develop modeling applications in the tidal part of the basin using the finite element model SLIM[2], itself being under development. Among other things, trace metals appeared to be an interesting but challenging subject of study. Indeed, together with biological processes (production and biodegradation), water and sediment circulation contribute largely to their dynamics. While it is possible to analyze the influence of biology locally, water and sediment circulation are global processes, for which a numerical model can be very useful.

The objective of this thesis is the development of the two-dimensional component of the finite element model SLIM in order to make possible such relatively long-term environmental simulations (several years). To that end, the hydrodynamics, the tracer processes et the sediment dynamics of the Scheldt Estuary must be accurately represented, using a model whose computational cost is not too high. Most of the environmental simulations of the Scheldt Estuary were carried out using dispersion box-models (Vuksanovic et al., 1996; Baeyens et al., 1998b; De Smedt et al., 1998; Ouboter et al., 1998; Steen et al., 2002; Vanderborght et al., 2002). These models have the advantage of a low computational cost, but they do not take the tidal dynamics into account, and they are not able to represent the variability of the bathymetry across the section. This approach is therefore too simplified in comparison with our objectives. Recently, a few environmental studies were carried out using two-dimensional depth-averaged models (Vanderborght et al., 2007), sometimes associated with a sediment module (Arndt et al., 2007, 2009). Our approach is rather similar. However, unlike those previous studies, we use a finite element model that enables the use of unstructured grids, which allow to spatially modulate the resolution in a flexible way. So far, even if three-dimensional models of the Scheldt Estuary exist (Can-

[1]TIMOTHY: Tracing and Integrated Modeling of Natural and Anthropogenic Effects on Hydrosystems : The Scheldt River basin and adjacent coastal North Sea, www.climate.be/TIMOTHY.

[2]SLIM: Second-generation Louvain-la-Neuve Ice-ocean Model, www.climate.be/SLIM.

S0	Terneuzen
S1	Overloop van Hansweert
S2	Baalhoek
S3	Buoy 87
S4	Buoy 92
S5	Buoy 105
S6	Antwerp
S7	Kruibeke
S8	Bazel
S9	Steendorp
S10	Temse
S11	Mariekerke
S12	Vlassenbroek
S13	Dendermonde
S14	St. Onolfs
S15	Appels
S16	Uitbergen
S17	Wetteren

Table 1.1: Names of the measurement stations displayed on Figure 1.2.

cino and Neves, 1999; van Kessel et al., 2011), they are restricted to the study of sediment dynamics, because of their high computational cost.

1.2 Hydrology of the Scheldt

The aim of this section is to describe the model domain and its hydrological characteristics that need to be satisfactorily simulated in order to reach the objective of the thesis presented in the previous section, i.e. make environmental studies possible. The model mesh is presented in Figure 1.2. The lower part shows the tidal part of the Scheldt Basin, which is the domain of interest. It can be divided into two subdomains: the estuary from the mouth to the confluence with the Rupel, and the tidal river network (up to Ghent for the Scheldt). The model domain is extended downstream to the shelf break in order to include the external meteorological forcings in a proper way.

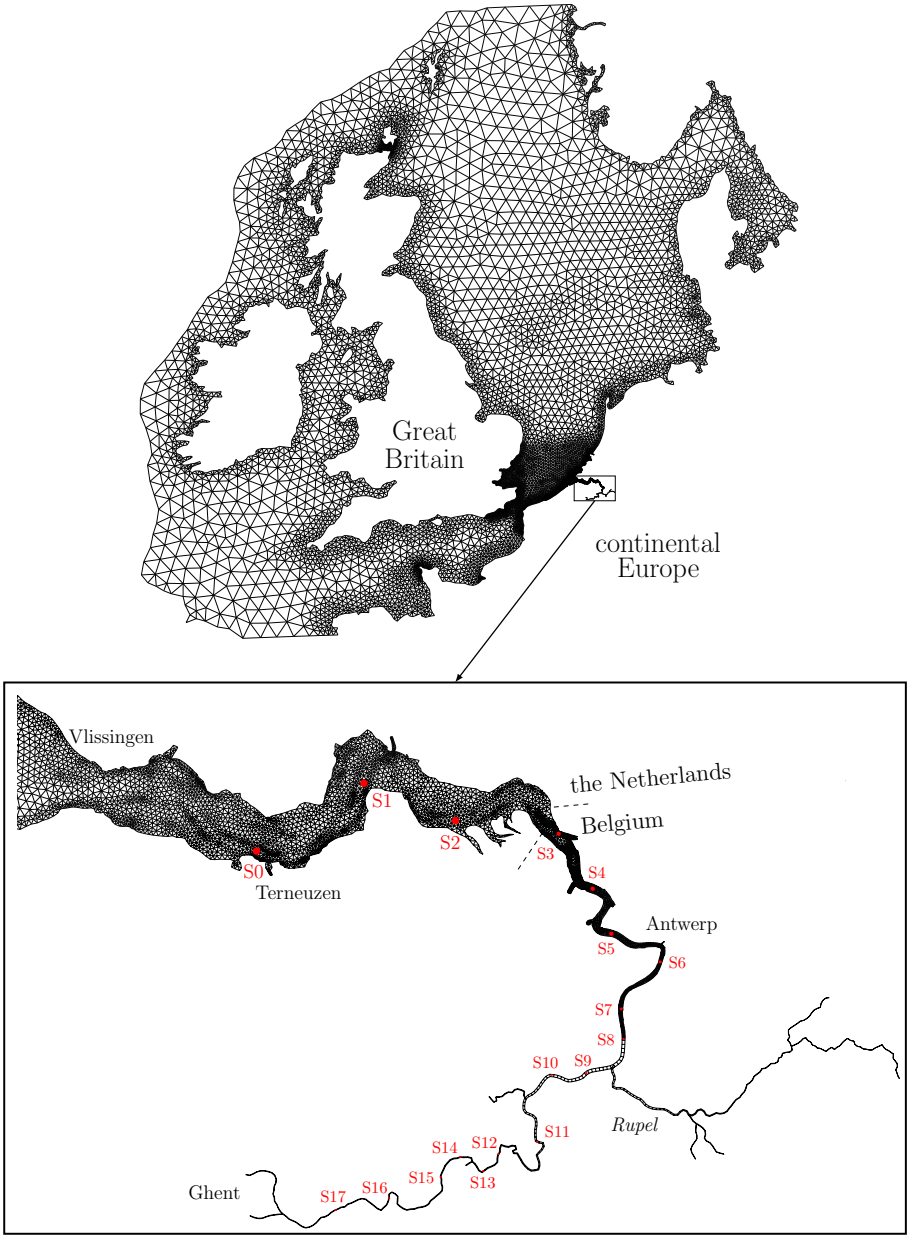

Figure 1.2: Typical mesh for the Scheldt Estuary simulations, including the Northwestern European continental shelf, the Scheldt Estuary and the tidal rivers of the Scheldt Basin (about 22000 triangles and 350 segments), in red, locations of measurement stations that provided data used in this thesis (Table 1.1).

Figure 1.3: Satellite view of the Scheldt Estuary (from Google Earth^{TM} mapping service); the tidal flats are the emerging lands between the mouth and the area of the port of Antwerp.

The Scheldt is a macrotidal estuary: the amount of water entering and leaving the estuary during one M_2 tidal cycle is approximately 200 times higher than the mean river discharge during the same period (Gourgue et al., 2009). The tidal range is about 4 m at Vlissingen, 5 m at Antwerp and 2 m at Ghent (where sluices prevent the tide from propagating upstream). The tide constitutes therefore the main forcing of our domain of interest. That is why the model domain is extended to the shelf break, in order to impose the tidal signal properly. As a consequence of the relatively small river discharge compared to the strong tides, the water column is generally well mixed (Baeyens et al., 1998c), implying that it is appropriate to use a two-dimensional depth-averaged model to study the Scheldt Estuary (Vanderborght et al., 2007).

The important tidal amplitude has another important consequence. Except two deep ebb and flood channels, the estuarine part is generally very shallow and features large tidal flats and sand banks (Figure 1.3). Each tidal cycle, approximately 110 km^2 of the estuarine surface are emerging during the ebbing phase (Arndt et al., 2007). Modeling the wetting and drying processes has always been a challenge in estuarine and coastal modeling. The Scheldt no exception (Gourgue et al., 2009; Kärnä et al., 2011a).

The Scheldt and its tributaries are rain-fed, in that their discharge vary considerably according to seasons: from $20 - 50\,\mathrm{m^3\,s^{-1}}$ in summer and autumn to $200 - 600\,\mathrm{m^3\,s^{-1}}$ in winter and spring, with an annual average between 100 and $200\,\mathrm{m^3\,s^{-1}}$ (Fettweis et al., 1998; Chen et al., 2005b; van der Wal et al., 2010). Even if it does not influence that much the estuarine hydrodynamics, it plays an important role in the horizontal transport of passive tracers (such as salinity) or dissolved contaminants (such as the dissolved phase of trace metals). For example, the salinity shift during a tidal period is much smaller than the salinity shift between high and low river discharges (Baeyens et al., 1998c).

The Scheldt is a relatively turbid estuary with three estuarine turbidity maxima (Chen et al., 2005b). The most important one occurs in the area of Antwerp and a second one is located in the riverine part. The third one is located downstream of the mouth, in front of the Belgian–Dutch coast, but therefore outside of our domain of interest. The suspended sediment concentrations feature variations at the tidal and spring/neap cycle scales that are closely linked to the hydrodynamic regime (Chen et al., 2005b; Arndt et al., 2007). They also undergo seasonal variations (the turbidity is higher in winter than in summer). However, as the currents induced by the tides are so much higher than the residual current, the seasonal variations of the river discharge have virtually no influence on the seasonal variations of the sediment dynamics. Other physico-chemical processes are therefore involved in that phenomenon (Chen et al., 2005b; van der Wal et al., 2010; Gourgue et al., 2011a).

Most environmental studies involve the transport of contaminants dissolved in the water column and adsorbed on suspended sediments. It is anyway the case for the trace metal pollution. All the hydrological characteristics mentioned above must therefore be accurately simulated before starting them. Once again, the subject of this thesis is the development of the finite element model SLIM in order to attain this objective.

1.3 SLIM: a finite element model

Resolution is a primary determinant of model accuracy. However, the wide range of space scales acting in the estuarine-coastal-open sea gradient makes uniform resolution inefficient. Besides nesting between models

of different grid resolution, unstructured grid models offer an attractive solution. Moreover, they allow a better representation of the coastlines.

However, traditionally, marine and ocean models are based on finite differences schemes on Cartesian grids (Griffies et al., 2000). It is only recently that unstructured grid methods are used in ocean and coastal modeling. They are based on finite volume (Casulli and Zanolli, 2002; Chen et al., 2003; Ham et al., 2005; Fringer et al., 2006), continuous finite element (Danilov et al., 2005; Walters, 2005, 2006; Piggott et al., 2008; Le Bars et al., 2010) and discontinuous finite element (Aizinger and Dawson, 2002, 2007; Dawson and Aizinger, 2005; Kubatko et al., 2006) techniques. Based on the finite element method, SLIM is one of these unstructured-grid models.

At the origin, SLIM was intended to become a three-dimensional baroclinic model of the world ocean. However, so far, it is still a work under development, although the three-dimensional component of SLIM is already able to solve accurately some academic barotropic (White et al., 2008a) and baroclinic (Blaise et al., 2010a; Comblen et al., 2010a; Kärnä et al., 2011b) test cases. On the other hand, the two-dimensional depth-averaged component of SLIM is already applied on real domains: the Great Barrier Reef in Australia (Lambrechts et al., 2008b), the Mahakam Delta in Indonesia (de Brye et al., 2011b), and even Lake Tanganyika in central Africa (Gourgue et al., 2007) with a reduced-gravity version of the two-dimensional component.

In this thesis, the Scheldt Estuary is studied using the combination of the two-dimensional depth-averaged and one-dimensional section-averaged components of SLIM. The tide is imposed on the shelf break and propagates across the Northwestern European continental shelf, including the Scheldt Estuary. The two-dimensional component is used up to Antwerp, while the one-dimensional component is used upstream in the Scheldt River and its tributaries up to the limit of the tidal influence. A typical mesh for the Scheldt simulations is presented in Figure 1.2. As already stated above, a consequence of the relatively small river discharge compared to the strong tides is that the water column is generally well mixed (Baeyens et al., 1998c), implying that it is appropriate to use a two-dimensional depth-averaged model to study the Scheldt Estuary (Vanderborght et al., 2007). Moreover, another consequence is the relatively long exposure time of water, which is about two to three months (Soetaert and Herman, 1995; Baeyens et al., 1998c; Blaise et al., 2010b; Arndt et al., 2007; de Brauwere et al., 2011a; de Brye et al., 2011a). The exposure time of suspended particles is even higher,

considering that they may settle and remain some time on the bottom (Delhez and Wolk, 2011). Comparing with the short-term processes of the hydrodynamics and the sediment dynamics (a few hours), this may lead to relatively long-term simulations (at least a few months). The computer cost for such simulations may be too high with modern three-dimensional models. It is less so with two-dimensional models. We therefore believe that the choice of using the combination of a two-dimensional model (almost everywhere) and a one-dimensional model (for the upstream tidal river network) is a sensible option.

First studies on the Scheldt Estuary using SLIM concerned the development of wetting-drying methods (Gourgue et al., 2009; Kärnä et al., 2011a), the validation of the hydrodynamic simulations (de Brye et al., 2010), and the evaluation of transport timescales (Blaise et al., 2010b; de Brauwere et al., 2011a; de Brye et al., 2011a). The first environmental application is the study of the fecal bacteria pollution using a model that does not take into account explicitly the sediment-related processes (de Brauwere et al., 2009, 2011b). The recent developments of the sediment module (Gourgue et al., 2011a) are already of use to improve the quality of the fecal bacteria simulations (de Brauwere et al., 2011c).

1.4 Main contributions

I entered the group SLIM with the aim to develop a eco-hydrodynamic finite element model of Lake Tanganyika (Central Africa) in collaboration with people involved in the project CLIMFISH[3]. After the termination of the project, only little collaboration was still possible. That is why I switched to the project TIMOTHY and the Scheldt Estuary. Although it has been decided not to include it in the present dissertation, the work carried out in this first period of my PhD thesis led to two publications (Gourgue et al., 2007, 2011b).

On the other hand, the development of SLIM in order to make possible complex environmental studies of the Scheldt Estuary is a 5-year team work. Each contribution has been brought in collaboration, sometimes with people not directly involved in the project TIMOTHY. This also led me to collaborate to studies applied on other domains, such as the Great Barrier Reef (Lambrechts et al., 2010). Nevertheless, in this

[3]CLIMFISH: Climate change impact on sustainable use of Lake Tanganyika fisheries.

section I want to point out two major developments that may constitute my main contributions to the project TIMOTHY.

The flux-limiting wetting-drying method

The first major contribution focuses on numerics. As mentioned above, the Scheldt Estuary features large shallow areas that are periodically emerging at low tide. This phenomenon has always been a numerical challenge in estuarine modeling because the classical discretizations of the governing equations are intrinsically unable to deal with areas where the water thickness may become zero. The solution proposed here is exclusively designed for finite element models using linear discontinuous spatial discretization methods and explicit time integration methods. Section 3.2.2 demonstrates its very good performance on standard academic test cases, and its application to the Scheldt Estuary leads to promising results (Gourgue et al., 2009).

However, explicit time integration methods restrict the time step to rather small values. As the current stable version of SLIM is not optimized for computational efficiency, the flux-limiting method cannot be used for long-term simulations. To circumvent this problem, the modified bathymetry method has been proposed (Kärnä et al., 2011a). It is designed for any time integration scheme, but with the drawback to be less accurate than the flux-limiting method in some specific situations. This is nevertheless the method used for the long-term simulations of this thesis.

As long as implicit time integration methods are mandatory, the flux-limiting method cannot be used. However, the new version of SLIM is designed to increase the computational efficiency of explicit methods. The flux-limiting method could therefore become an attractive solution for this new version. Moreover, only explicit schemes benefit from large parallel computing that are necessary when considering three-dimensional simulations of real applications. The wetting-drying method for the three-dimensional component of SLIM could therefore be based on the flux-limiting method.

The sediment module

The second major contribution is concerning the physics. As mentioned many times above, in order to undertake complex environmental studies, an accurate sediment module had to be developed in SLIM. Modeling

the sediment dynamics using a two-dimensional depth-averaged model is also a challenge, as it is essentially a vertical phenomenon. Besides building a functioning sediment transport model, the aim of this study research was to identify, parametrize and quantify the key processes that are necessary to represent satisfactorily the suspended sediment dynamics in the Scheldt Estuary and tidal river network.

The results presented in Chapter 5 point out some important aspects. Firstly, the settling velocity of suspended sediments is influenced by flocculation. The most important factor governing this process is the suspended sediment concentration itself, but the influence of the salinity and the biological activity must also be taken into account to allow a correct representation of the suspended sediment concentration variability over a wide range of timescales. Secondly, to represent satisfactorily the seasonal variations of the suspended sediment concentration, the influence of the biological activity on the bottom erodibility has to be taken into account. The distribution of sediment types along the estuary must also be considered to obtain an accurate longitudinal turbidity profile.

The computer cost of a two-dimensional model is significantly smaller than that of three-dimensional models traditionally deemed indispensable in sediment transport modeling. The good behavior of our two-dimensional model SLIM, even comparing with the results of a three-dimensional one, is probably one of the main achievements of this study.

1.5 Outline

Chapter 2 presents the bases of the hydrodynamic module of SLIM. Using suitable hypotheses, the two-dimensional depth-averaged shallow water equations are established starting from the generic three-dimensional equations of continuum mechanics. Their numerical finite element formulation is then detailed. Preliminary results are shown to illustrate the good behavior of the model to represent the tidal motion in the North Sea, the major forcing of the Scheldt Estuary.

In order to simulate accurately the hydrodynamics in the Scheldt Estuary itself, a specific treatment is needed to deal with the wetting and drying processes occurring in the shallow zones. **Chapter 3** presents two methods designed for this purpose that are implemented into SLIM. Simulations of the Scheldt Estuary hydrodynamics are presented at the end of the chapter.

Chapter 4 is devoted to the tracer transport modeling. As a simple passive tracer that can only be transported according to the flow, salinity is perfect to calibrate the transport processes of the model. Using hypotheses similar to the hydrodynamic module, the passive tracer transport equation is deduced from the generic three-dimensional advection-diffusion equation. Its numerical finite element formulation is then presented. The chapter ends with the simulation of the Scheldt Estuary salinity dynamics.

The sediment module is presented in **Chapter 5**, starting with the presentation of the governing equations and their numerical implementation. The choice of suitable parametrizations and their calibration to represent accurately the sediment dynamics of the Scheldt Estuary are then discussed. This constitutes the final step in order to make possible environmental studies with SLIM.

The conclusions are drawn in **Chapter 6**, which finishes with some perspectives about future trace metal simulations.

1.6 Supporting publications

1. **Gourgue, O.**, Deleersnijder, E., and White, L. (2007). Toward a generic method for studying water renewal, with application to the epilimnion of Lake Tanganyika. *Estuarine, Coastal and Shelf Science*, 74:628–640.

2. **Gourgue, O.**, Comblen, R., Lambrechts, J., Kärnä, T., Legat, V., and Deleersnijder, E. (2009). A flux-limiting wetting-drying method for finite-element shallow-water models, with application to the Scheldt Estuary. *Advances in Water Resources*, 32:1726-1739.

3. de Brauwere, A., De Ridder, F., **Gourgue, O.**, Lambrechts, J., Comblen, R., Pintelon, R., Passerat, J., Servais, P., Elskens, M., Baeyens, W., Kärnä, T., de Brye, B., and Deleersnijder, E. (2009). Design of a sampling strategy to optimally calibrate a reactive transport model: Exploring the potential for Escherichia coli in the Scheldt Estuary. *Environmental Modelling & Software*, 24:969–981.

4. de Brye, B., de Brauwere, A., **Gourgue, O.**, Kärnä, T., Lambrechts, J., Comblen, R., Deleersnijder, E. (2010) A finite-element, multi-scale model of the Scheldt tributaries, river, estuary and ROFI. *Coastal Engineering*, 57:850-863.

5. Lambrechts, J., Humphrey, C., McKinna, L., **Gourgue, O.**, Fabricius, K. E., Mehta, A. J., Lewis, S., and Wolanski, E. (2010). Importance of wave-induced bed liquefaction in the fine sediment budget of Cleveland Bay, Great Barrier Reef. *Estuarine, Coastal and Shelf Science*, 89:154–162.

6. Kärnä, T., de Brye, B., **Gourgue, O.**, Lambrechts, J., Comblen, R., Legat, V., and Deleersnijder, E. (2011). A fully implicit wetting-drying method for DG-FEM shallow water models, with an application to the Scheldt Estuary. *Computer Methods in Applied Mechanics and Engineering*, 200:509–524.

7. **Gourgue, O.**, Deleersnijder, E., Legat, V., Marchal, E., and White, L. (2011). Free and forced thermocline oscillations in Lake Tanganyika. In Alpert, P. and Sholokhman, T., editors, *Factor separation in the atmosphere: applications and future prospects*, chapter 9, pages 146–162. Cambridge University Press.

8. de Brye, B., de Brauwere, A., **Gourgue, O.**, Delhez, E.J.M., and Deleersnijder, E. Water renewal timescales in the Scheldt Estuary. *Journal of Marine Systems* (accepted for publication).

9. **Gourgue, O.**, Baeyens, W., Chen, M., de Brauwere, A., de Brye, B., Deleersnijder, E., Elskens, M., and Legat, V. A depth-averaged sediment transport model for environmental studies in the Scheldt Estuary and tidal river network. *Journal of Marine Systems* (submitted).

10. de Brauwere, A., **Gourgue, O.**, de Brye, B., Servais, P., Ouattara, N. K., and Deleersnijder, E. Modelling *Escherichia coli* dynamics in the Scheldt land-sea continuum. Part II. The tidal Scheldt River and Estuary. *Journal of Marine Systems* (in preparation).

Chapter 2

Hydrodynamics

2.1 Introduction

Marine flows are taking place in shallow domains, i.e. the thickness of the fluid layer is small compared with the typical horizontal length scales. Considering, moreover, that the water density variations are small and that the pressure is hydrostatic, the flow is then governed by the three-dimensional baroclinic equations. They are the basis of the three-dimensional component of SLIM that is still under development (Blaise et al., 2010b; Comblen et al., 2010a; Kärnä et al., 2011b). Finally, if the density variations have little influence on the pressure variations and if the flow is vertically well-mixed, the three-dimensional equations may be integrated over the water column to obtain the so-called shallow-water equations. These depth-averaged equations are the basis of the two-dimensional component of SLIM, which is widely used in this doctoral dissertation.

In Section 2.2, the different governing equations are derived from the general budget equations of continuum mechanics, and section 2.3 describes how the shallow water equations are discretized in a finite element framework. At this stage, however, the model is not fully equipped to undertake simulations of the hydrodynamics of the Scheldt Estuary, which is subject to periodic wetting and drying of shallow areas that require a specific treatment (Chapter 3). Nevertheless, the results pre-

sented in Section 2.4 show that it is already quite accurate in simulating the tidal motion in the North Sea.

2.2 Governing equations

In continuum fluid mechanics, in a rotating framework, the differential equations derived from the mass and momentum budgets are expressed as follows (Kundu and Cohen, 2002):

$$\frac{\partial \rho}{\partial t} + \boldsymbol{\nabla} \cdot (\rho \boldsymbol{v}) = 0, \tag{2.1}$$

$$\rho \frac{\partial \boldsymbol{v}}{\partial t} + \rho \boldsymbol{v} \cdot \boldsymbol{\nabla} \boldsymbol{v} + \rho \boldsymbol{a} = \rho \boldsymbol{g} + \boldsymbol{\nabla} \cdot \boldsymbol{\sigma}, \tag{2.2}$$

where the variables ρ and $\boldsymbol{v}$ are the density and velocity fields, respectively, t is the time, $\boldsymbol{\nabla}$ is the del operator, $\boldsymbol{a}$ is the acceleration induced by the Earth rotation, $\boldsymbol{g}$ is the gravitational acceleration, and $\boldsymbol{\sigma}$ is the stress tensor, which must be symmetric. Equations (2.1) and (2.2) are called the continuity equation and the momentum budget equation, respectively.

Boussinesq approximation in the continuity equation

The continuity equation (2.1) can be rewritten as follows:

$$\frac{\partial \rho}{\partial t} + \boldsymbol{v} \cdot \boldsymbol{\nabla} \rho + \rho \boldsymbol{\nabla} \cdot \boldsymbol{v} = 0, \tag{2.3}$$

In most geophysical flows the water density may be decomposed into a mean constant value ρ_0 and a small variation ρ' about it (Cushman-Roisin, 1994; Kundu and Cohen, 2002):

$$\rho = \rho_0 + \rho', \qquad \rho' \ll \rho_0, \tag{2.4}$$

where ρ_0 is a constant and ρ' varies in space and time. Even in estuaries, where fresh river waters are mixing with salty sea waters, the density variations are less than a few percents (Cushman-Roisin, 1994).

It is therefore clear that the second term of equation (2.3) is much smaller than the third one. Moreover, the first term is also quite small when restricting to flows with large characteristic timescales, and therefore ignoring the propagation of sound waves. So, the continuity equation reduces to

$$\boldsymbol{\nabla} \cdot \boldsymbol{v} = 0. \tag{2.5}$$

The Boussinesq approximation leads therefore to consider the incompressibility of the flow.

Constitutive equation for a Newtonian fluid

A constitutive equation is the relation between stress and deformation in a continuum. In this section, an equation that linearly relates the stress and rate of strain is examined. For a moving fluid, the stress tensor $\boldsymbol{\sigma}$ may be split into an isotropic part $-p\boldsymbol{\delta}$ that would exist if the fluid were at rest, and a non-isotropic part $\boldsymbol{\tau}$ due to the fluid motion alone (Kundu and Cohen, 2002):

$$\boldsymbol{\sigma} = -p\boldsymbol{\delta} + \boldsymbol{\tau}, \tag{2.6}$$

where $\boldsymbol{\delta}$ is the Kronecker tensor, whose components are defined as follows:

$$\delta_{ij} = \begin{cases} 1 & \text{if } i = j \\ 0 & \text{if } i \neq j. \end{cases} \tag{2.7}$$

In the case of a Newtonian incompressible fluid, the non isotropic part $\boldsymbol{\tau}$ is called the viscous stress tensor and is defined as

$$\boldsymbol{\tau} = 2\mu\boldsymbol{d}, \tag{2.8}$$

where μ is the dynamic viscosity, and $\boldsymbol{d}$ is the strain rate tensor, defined as

$$\boldsymbol{d} = \frac{1}{2}\big((\boldsymbol{\nabla v})^t + (\boldsymbol{\nabla v})\big). \tag{2.9}$$

The equation of motion for a Newtonian fluid is obtained by introducing the constitutive equation (2.6) into the momentum budget equation (2.2):

$$\rho\frac{\partial \boldsymbol{v}}{\partial t} + \rho\boldsymbol{v}\cdot\boldsymbol{\nabla v} + \rho\boldsymbol{a} = -\boldsymbol{\nabla}p + \rho\boldsymbol{g} + \boldsymbol{\nabla}\cdot(2\mu\boldsymbol{d}). \tag{2.10}$$

This is the general form of the Navier-Stokes equation for incompressible flows, in a rotating framework. In this equation, the viscosity μ is a function of the thermodynamic state, and indeed, μ displays a rather strong dependence on temperature. However, temperature differences

are rather small in sea water, so that μ can be taken outside the derivative (Kundu and Cohen, 2002). Using the continuity equation (2.5), the Navier-Stokes equation (2.10) reduces to:

$$\rho\frac{\partial \boldsymbol{v}}{\partial t} + \rho\boldsymbol{v}\cdot\boldsymbol{\nabla}\boldsymbol{v} + \rho\boldsymbol{a} = -\boldsymbol{\nabla}p + \rho\boldsymbol{g} + \mu\nabla^2\boldsymbol{v}, \tag{2.11}$$

where $\nabla^2 = \boldsymbol{\nabla}\cdot\boldsymbol{\nabla}$ is the Laplacian operator. Nevertheless, even if the spatial variations of μ are small, the following form is generally preferred:

$$\rho\frac{\partial \boldsymbol{v}}{\partial t} + \rho\boldsymbol{v}\cdot\boldsymbol{\nabla}\boldsymbol{v} + \rho\boldsymbol{a} = -\boldsymbol{\nabla}p + \rho\boldsymbol{g} + \boldsymbol{\nabla}\cdot(\mu\boldsymbol{\nabla}\boldsymbol{v}). \tag{2.12}$$

Boussinesq approximation in the momentum budget equation

As a reminder, the main hypothesis beyond the Boussinesq approximation is that the density variation ρ' is much smaller that the mean density ρ_0, which is illustrated by equation (2.4). However, this does not mean that the density variations can be neglected in all terms of the momentum budget equation (2.12).

Considering the static state in which the density is ρ_0 everywhere, the pressure $p_0(z)$ would be such that

$$\boldsymbol{\nabla}p_0 = \rho_0\boldsymbol{g}. \tag{2.13}$$

Subtracting the static state and dividing by ρ_0, the momentum budget equation (2.12) reduces to

$$\left(1+\frac{\rho'}{\rho_0}\right)\left(\frac{\partial \boldsymbol{v}}{\partial t} + \boldsymbol{v}\cdot\boldsymbol{\nabla}\boldsymbol{v} + \boldsymbol{a}\right) = -\frac{1}{\rho_0}\boldsymbol{\nabla}p' + \frac{\rho'}{\rho_0}\boldsymbol{g} + \boldsymbol{\nabla}\cdot(\nu\boldsymbol{\nabla}\boldsymbol{v}), \tag{2.14}$$

where $p' = p - p_0$, and $\nu = \mu/\rho_0$ is the kinematic viscosity.

In the left-hand part of equation (2.14), the factor ρ'/ρ_0 is added to 1, which is much larger. The density variations can therefore be neglected in the inertia terms. However, the same ratio appears alone in the gravity term, which is still very large. As a consequence, the density variations are negligible in the momentum budget equation, except when ρ is multiplied by g (Kundu and Cohen, 2002). Therefore, re-adding the static state, the momentum budget equation reads:

$$\frac{\partial \boldsymbol{v}}{\partial t} + \boldsymbol{v}\cdot\boldsymbol{\nabla}\boldsymbol{v} + \boldsymbol{a} = -\frac{1}{\rho_0}\boldsymbol{\nabla}p + \frac{\rho}{\rho_0}\boldsymbol{g} + \boldsymbol{\nabla}\cdot(\nu\boldsymbol{\nabla}\boldsymbol{v}). \tag{2.15}$$

Taking the density variations into account only in the gravity term of the momentum budget equation is called the Boussinesq approximation and is commonly used in geophysical flow modeling (Cushman-Roisin, 1994; Kundu and Cohen, 2002).

Rotating framework

The acceleration $\boldsymbol{a}$ appears because the equations (2.1) and (2.2) are written in a non-inertial rotating framework linked to the Earth. It may be decomposed into the sum of the Coriolis and centripetal accelerations (Cushman-Roisin, 1994; Kundu and Cohen, 2002):

$$\boldsymbol{a} = \underbrace{2\boldsymbol{\Omega} \times \boldsymbol{v}}_{\text{Coriolis}} + \underbrace{\boldsymbol{\Omega} \times (\boldsymbol{\Omega} \times \boldsymbol{x})}_{\text{centripetal}}, \tag{2.16}$$

where $\boldsymbol{\Omega}$ is the Earth rotation vector and $\boldsymbol{x}$ is the position vector from the center of the Earth. When placed on the right-hand side of the momentum budget equation (2.15), these terms can be assimilated to fictitious forces that are called the Coriolis and centrifugal forces, respectively.

In the absence of rotation, gravitational forces keep the matter of a planet together to form a spherical body. The outward pull caused by the centrifugal force distorts this spherical equilibrium, and the planet assumes a slightly flattened shape. Actually, at equilibrium, the surface of the planet is such that gravitational and local centrifugal forces combine into a net force everywhere aligned with the local normal to the surface (Figure 2.1). This net force is called the effective gravity force (Kundu and Cohen, 2002). In what follows, $\boldsymbol{g}$ is understood as the effective gravity force, so that the momentum budget equation may be rewritten as follows:

$$\frac{\partial \boldsymbol{v}}{\partial t} + \boldsymbol{v} \cdot \boldsymbol{\nabla} \boldsymbol{v} + 2\boldsymbol{\Omega} \times \boldsymbol{v} = -\frac{1}{\rho_0} \boldsymbol{\nabla} p + \frac{\rho}{\rho_0} \boldsymbol{g} + \boldsymbol{\nabla} \cdot (\nu \boldsymbol{\nabla} \boldsymbol{v}). \tag{2.17}$$

Using the non-inertial local basis $(\boldsymbol{e}_x, \boldsymbol{e}_y, \boldsymbol{e}_z)$ depicted in Figure 2.2, the Earth rotation vector $\boldsymbol{\Omega}$ can be decomposed into two parts:

$$\boldsymbol{\Omega} = \Omega \cos(\phi) \boldsymbol{e}_y + \Omega \sin(\phi) \boldsymbol{e}_z, \tag{2.18}$$

where $\Omega = \|\boldsymbol{\Omega}\|$ is the Earth rotation rate, and ϕ is the latitude. The Coriolis acceleration becomes

$$\begin{aligned} 2\boldsymbol{\Omega} \times \boldsymbol{v} &= 2\Omega \cos(\phi) \boldsymbol{e}_y \times \boldsymbol{v} + 2\Omega \sin(\phi) \boldsymbol{e}_z \times \boldsymbol{v} \\ &\triangleq f_* \boldsymbol{e}_y \times \boldsymbol{v} + f \boldsymbol{e}_z \times \boldsymbol{v}, \end{aligned} \tag{2.19}$$

where the coefficients f and f_* are called the Coriolis and reciprocal Coriolis parameters, respectively.

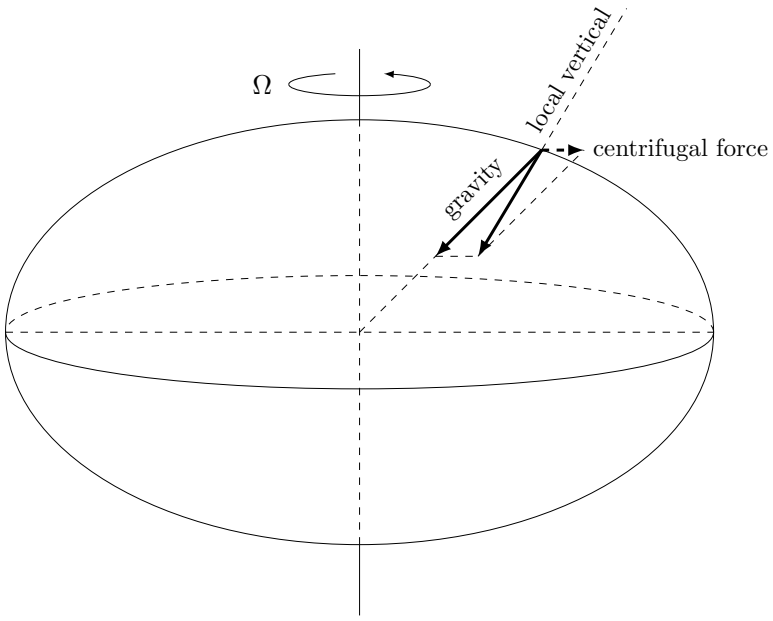

Figure 2.1: How the flattening of a rotating body causes the gravitational and centrifugal forces to combine into a force aligned with the local vertical, so that equilibrium is reached; to illustrate this phenomenon, the effect is grossly exaggerated compared to the Earth situation.

Reynolds equations for turbulent flows

Most marine flows must be regarded as turbulent, i.e. composed of stochastic motions or eddies on widely varying scales. Although the Navier-Stokes equations are generally believed to describe turbulence, that is not particularly useful as the focus is usually on larger scale features (Vreugdenhil, 1994; Kundu and Cohen, 2002). In order to isolate those large scale features, each variable is split into a slowly varying mean value, which as to be regarded as an ensemble average, and a random variation about it. For example:

$$\boldsymbol{v} = \overline{\boldsymbol{v}} + \boldsymbol{v}'. \tag{2.20}$$

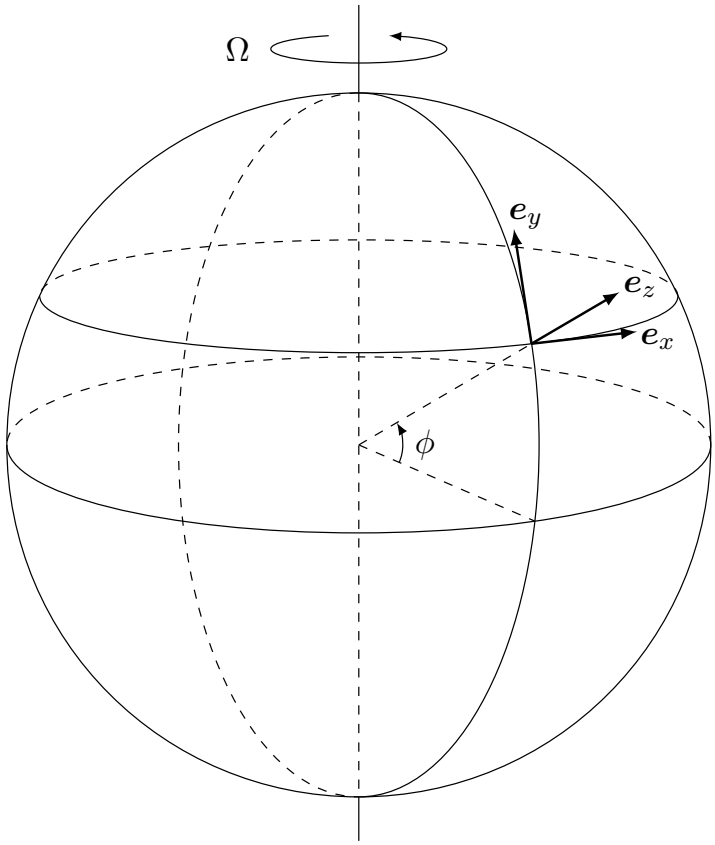

Figure 2.2: Rotating framework of the Earth and its local non-inertial cartesian basis $(\boldsymbol{e}_x, \boldsymbol{e}_y, \boldsymbol{e}_z)$; $\boldsymbol{e}_x$ is aligned eastward, $\boldsymbol{e}_y$ northward and $\boldsymbol{e}_z$ upward; the angle ϕ gives the latitude.

It is important to note that the mean of a product is not the product of the means (Vreugdenhil, 1994; Kundu and Cohen, 2002):

$$\overline{\boldsymbol{v}\boldsymbol{v}} = \overline{\boldsymbol{v}}\,\overline{\boldsymbol{v}} + \overline{\boldsymbol{v}'\boldsymbol{v}'}. \tag{2.21}$$

Introducing the splitting for each quantity in equations (2.5) and (2.17), and taking the ensemble average, leads to the so-called Reynolds equations for the statistical average of a turbulent flow (Vreugdenhil, 1994). They are very similar as the original equations (2.5) and (2.17). The major difference is the presence of an additional term $\boldsymbol{\nabla} \cdot (\overline{\boldsymbol{v}'\boldsymbol{v}'})$ in the left-hand side of the momentum budget equation. When placed in the right-hand side, the tensor $-\overline{\boldsymbol{v}'\boldsymbol{v}'}$ can be seen as an additional stress

and is called the Reynolds stress tensor. It represents the exchange of momentum between fluid elements by turbulent motion (Vreugdenhil, 1994). It is a priori unknown and has to be parameterized in terms of the mean motion to obtain a closed system of equations.

One of the simplest approach is the Boussinesq eddy viscosity model in which the transfer of momentum caused by turbulent motions is modeled with an effective eddy viscosity in a similar way as the momentum transfer caused by friction is modeled with a molecular viscosity:

$$-\overline{\boldsymbol{v}'\boldsymbol{v}'} \triangleq 2\nu_{\mathrm{t}}\overline{\boldsymbol{d}} - \frac{2}{3}k\boldsymbol{\delta}, \tag{2.22}$$

where ν_{t} is the turbulence eddy viscosity, $\overline{\boldsymbol{d}}$ is the mean strain rate tensor and k is the turbulent kinetic energy (e.g. Speziale, 1991). The eddy viscosity is not constant and may actually vary greatly over the same domain. Indeed, it is no longer a fluid property, it rather depends on the local flow state. Typical values of ν_{t} range from 10^{-5} to 10^{-1} $\mathrm{m^2\,s^{-1}}$ in marine applications. In comparison, the molecular kinematic viscosity $\nu \sim 10^{-6}$ $\mathrm{m^2\,s^{-1}}$ is generally small, so that its effect is neglected. The term $-\frac{2}{3}k\boldsymbol{\delta}$ is necessary for consistency with the definition of the kinetic energy (Speziale, 1991):

$$k = \frac{1}{2}\overline{\boldsymbol{u}' \cdot \boldsymbol{u}'}, \tag{2.23}$$

and it acts as an effective pressure. However, when equation (2.22) is substituted into the mean momentum budget equation, this term can be absorbed in the pressure gradient term (Garcia, 2006).

In what follows, the bars are omitted, and the continuity equation (2.5) and the momentum budget equation (2.17) are still used. However, it has to be remembered that all variables are now Reynolds-averaged quantities, and that the viscosity is now the turbulence eddy viscosity ν_{t}, which is not constant.

Typical scales and simplification of the equations

In this section, equations (2.5) and (2.17) are developed in terms of their components in the non-inertial local basis[1], and the order of magnitude of each term is estimated in order to eliminate the smallest ones. To

[1]For the sake of simplicity, the extraneous curvature terms are neglected; doing so is correct when dealing with horizontal length scales substantially shorter than the radius of the Earth.

variables	scales	units	orders of magnitude
x, y	L_h	m	10^4
z	L_v	m	10
t	T	s	10^4
u, v	U	$\mathrm{m\,s^{-1}}$	1
w	W	$\mathrm{m\,s^{-1}}$	10^{-3}
ρ	ρ_0	$\mathrm{kg\,m^{-3}}$	10^3
f, f^*	Ω	$\mathrm{s^{-1}}$	10^{-4}
	g	$\mathrm{m\,s^{-2}}$	10
	ν_t	$\mathrm{m^2\,s^{-1}}$	$10^{-5} \ldots 10^{-1}$

Table 2.1: Typical scales in the North Sea and the Scheldt.

that end, a scale is introduced for every variable. It is a constant of dimensions identical to that of the variable and that has a numerical value representative of the values of the variable. Typical values for marine applications are presented in Table 2.1[2]. The basic assumption beyond the shallow water model is that the vertical length scale L_v is much smaller than the horizontal one L_h, so that the aspect ratio $L_\mathrm{v}/L_\mathrm{h}$ is quite small, generally smaller than 0.01 (Vreugdenhil, 1994; Cushman-Roisin, 1994).

First of all, the continuity equation (2.5) may be developed as follows:

$$\underbrace{\frac{\partial u}{\partial x} + \frac{\partial v}{\partial y}}_{\frac{U}{L_\mathrm{h}}} + \underbrace{\frac{\partial w}{\partial z}}_{\frac{W}{L_\mathrm{v}}} = 0, \tag{2.24}$$

where (u, v, w) are the components of the velocity vector $\boldsymbol{v}$, and (x, y, z) are the coordinates. Three cases must be analyzed (Cushman-Roisin, 1994).

1. If $W/L_\mathrm{v} \gg U/L_\mathrm{h}$, equation (2.24) reduces to $\partial w/\partial z = 0$, which implies that w is constant in the vertical. Because of a bottom somewhere, flow must therefore be supplied by lateral convergence, and the terms $\partial u/\partial x$ and/or $\partial v/\partial y$ can not be neglected. This case must therefore be ruled out.

[2]The order of magnitude of the vertical velocity scale W is deduced from the worst case of equation (2.26).

2. If $W/L_\mathrm{v} \ll U/L_\mathrm{h}$, the leading balance is $\partial u/\partial x + \partial v/\partial y = 0$, which implies that convergence in one horizontal direction must be neutralized by a divergence in the other horizontal direction, which is very possible.

3. The case when W/L_v is on the order of U/L_h implies a three-way balance, which is also very possible.

To summarize, no term can be neglected in equation (2.24) and vertical velocity scale is constrained as follows:

$$\frac{W}{L_\mathrm{v}} \lesssim \frac{U}{L_\mathrm{h}}, \tag{2.25}$$

or,

$$\frac{W}{U} \lesssim \frac{L_\mathrm{v}}{L_\mathrm{h}}. \tag{2.26}$$

The ratio between vertical and horizontal velocity scales is therefore at most of the order of the ratio between vertical and horizontal length scales, so that $W \ll U$. That also means that the flow is almost two-dimensional.

The two horizontal components of the momentum budget equation (2.17) are developed as follows:

$$\begin{aligned}
&\underbrace{\frac{\partial u}{\partial t}}_{\frac{U}{T}} + \underbrace{u\frac{\partial u}{\partial x} + v\frac{\partial u}{\partial y}}_{\frac{U^2}{L_\mathrm{h}}} + \underbrace{w\frac{\partial u}{\partial z}}_{\frac{WU}{L_\mathrm{v}}} + \underbrace{f_* w}_{\Omega W} - \underbrace{fv}_{\Omega U} \\
&\qquad = \underbrace{-\frac{1}{\rho_0}\frac{\partial p}{\partial x}}_{\frac{\Delta p}{\rho_0 L_\mathrm{h}}} + \underbrace{\frac{\partial}{\partial x}\left(\nu_\mathrm{t}\frac{\partial u}{\partial x}\right) + \frac{\partial}{\partial y}\left(\nu_\mathrm{t}\frac{\partial u}{\partial y}\right)}_{\frac{\nu_\mathrm{t} U}{L_\mathrm{h}^2}} + \underbrace{\frac{\partial}{\partial z}\left(\nu_\mathrm{t}\frac{\partial u}{\partial z}\right)}_{\frac{\nu_\mathrm{t} U}{L_\mathrm{v}^2}},
\end{aligned} \tag{2.27}$$

$$\begin{aligned}
&\underbrace{\frac{\partial v}{\partial t}}_{\frac{U}{T}} + \underbrace{u\frac{\partial v}{\partial x} + v\frac{\partial v}{\partial y}}_{\frac{U^2}{L_\mathrm{h}}} + \underbrace{w\frac{\partial v}{\partial z}}_{\frac{WU}{L_\mathrm{v}}} + \underbrace{fu}_{\Omega U} \\
&\qquad = \underbrace{-\frac{1}{\rho_0}\frac{\partial p}{\partial y}}_{\frac{\Delta p}{\rho_0 L_\mathrm{h}}} + \underbrace{\frac{\partial}{\partial x}\left(\nu_\mathrm{t}\frac{\partial v}{\partial x}\right) + \frac{\partial}{\partial y}\left(\nu_\mathrm{t}\frac{\partial v}{\partial y}\right)}_{\frac{\nu_\mathrm{t} U}{L_\mathrm{h}^2}} + \underbrace{\frac{\partial}{\partial z}\left(\nu_\mathrm{t}\frac{\partial v}{\partial z}\right)}_{\frac{\nu_\mathrm{t} U}{L_\mathrm{v}^2}}.
\end{aligned} \tag{2.28}$$

Firstly, as $W \ll U$, the first Coriolis term in equation (2.27) is much smaller than the second one, and is therefore neglected. Secondly, according to the small aspect ration $L_\mathrm{v}/L_\mathrm{h}$, the horizontal turbulence viscosity terms in both equations are much smaller than the vertical ones, and can also be neglected. So, the horizontal components of the momentum budget equation reduce to

$$\frac{\partial u}{\partial t} + u\frac{\partial u}{\partial x} + v\frac{\partial u}{\partial y} + w\frac{\partial u}{\partial z} - fv = -\frac{1}{\rho_0}\frac{\partial p}{\partial x} + \frac{\partial}{\partial z}\left(\nu_\mathrm{t}\frac{\partial u}{\partial z}\right), \quad (2.29)$$

$$\frac{\partial v}{\partial t} + u\frac{\partial v}{\partial x} + v\frac{\partial v}{\partial y} + w\frac{\partial v}{\partial z} + fu = -\frac{1}{\rho_0}\frac{\partial p}{\partial y} + \frac{\partial}{\partial z}\left(\nu_\mathrm{t}\frac{\partial v}{\partial z}\right). \quad (2.30)$$

The vertical component of the momentum budget equation (2.17) is developed as follows:

$$\underbrace{\frac{\partial w}{\partial t}}_{\frac{W}{T}} + \underbrace{u\frac{\partial w}{\partial x} + v\frac{\partial w}{\partial y}}_{\frac{UW}{L_\mathrm{h}}} + \underbrace{w\frac{\partial w}{\partial z}}_{\frac{W^2}{L_\mathrm{v}}} - \underbrace{f_* u}_{\Omega U}$$

$$= \underbrace{-\frac{1}{\rho_0}\frac{\partial p}{\partial z}}_{\frac{\Delta p}{\rho_0 L_\mathrm{v}}} \underbrace{-\frac{\rho g}{\rho_0}}_{g} + \underbrace{\frac{\partial}{\partial x}\left(\nu_\mathrm{t}\frac{\partial w}{\partial x}\right) + \frac{\partial}{\partial y}\left(\nu_\mathrm{t}\frac{\partial w}{\partial y}\right)}_{\frac{\nu_\mathrm{t} W}{L_\mathrm{h}^2}} + \underbrace{\frac{\partial}{\partial z}\left(\nu_\mathrm{t}\frac{\partial w}{\partial z}\right)}_{\frac{\nu_\mathrm{t} W}{L_\mathrm{v}^2}}, \quad (2.31)$$

According to the values in Table 2.1, all terms are very small compared to the pressure gradient and gravity terms, so that only the hydrostatic relation remains:

$$\frac{\partial p}{\partial z} = -\rho g. \quad (2.32)$$

Keeping only the pressure gradient and gravity terms in the vertical component of the momentum budget equation is called the hydrostatic approximation. It is mainly due to the small aspect ration $L_\mathrm{v}/L_\mathrm{h}$.

The three-dimensional baroclinic shallow water equations

Equations (2.24), (2.29) and (2.30) are generally synthesized under the following form:

$$\boldsymbol{\nabla}_\mathrm{h} \cdot \boldsymbol{u} + \frac{\partial w}{\partial z} = 0, \quad (2.33)$$

$$\frac{\partial \boldsymbol{u}}{\partial t} + \boldsymbol{u} \cdot \boldsymbol{\nabla}_\mathrm{h}\boldsymbol{u} + w\frac{\partial \boldsymbol{u}}{\partial z} + f\boldsymbol{e}_z \times \boldsymbol{u} = -\frac{1}{\rho_0}\boldsymbol{\nabla}_\mathrm{h} p + \frac{\partial}{\partial z}\left(\nu_\mathrm{t}\frac{\partial \boldsymbol{u}}{\partial z}\right), \quad (2.34)$$

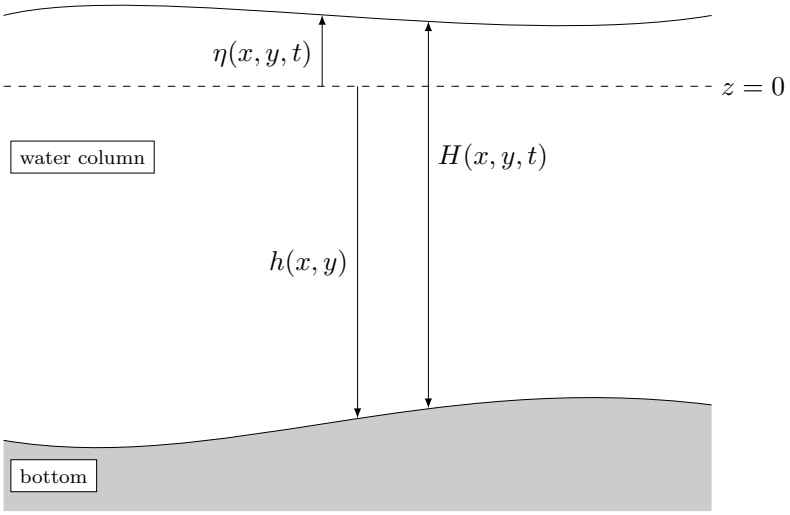

Figure 2.3: Vertical cut illustrating $\eta(x, y, t)$ the elevation above the reference level ($z = 0$), the bathymetry $h(x, y)$ and the water depth $H = \eta + h$.

where $\boldsymbol{u}$ is the horizontal projection of the velocity vector, and $\boldsymbol{\nabla}_{\mathrm{h}}$ the horizontal projection of the del operator. The pressure p is obtained by integrating the hydrostatic equation (2.32) over part of the water column:

$$p = p_{\mathrm{atm}} + \int_z^{\eta} \rho g \, dz, \tag{2.35}$$

where p_{atm} is the atmospheric pressure at the surface of the flow, and η is the elevation of the free surface above the reference level $z = 0$ (Figure 2.3).

The horizontal pressure gradient is therefore:

$$\begin{aligned}
\boldsymbol{\nabla}_{\mathrm{h}} p &= \boldsymbol{\nabla}_{\mathrm{h}} p_{\mathrm{atm}} + g\boldsymbol{\nabla}_{\mathrm{h}} \int_z^\eta \rho \, dz \\
&= \boldsymbol{\nabla}_{\mathrm{h}} p_{\mathrm{atm}} + \rho_{\mathrm{s}} g \boldsymbol{\nabla}_{\mathrm{h}} \eta + g \int_z^\eta \boldsymbol{\nabla}_{\mathrm{h}} \rho \, dz \\
&= \boldsymbol{\nabla}_{\mathrm{h}} p_{\mathrm{atm}} + (\rho_0 + \rho'_{\mathrm{s}}) g \boldsymbol{\nabla}_{\mathrm{h}} \eta + g \int_z^\eta \boldsymbol{\nabla}_{\mathrm{h}} (\rho_0 + \rho') \, dz \\
&\cong \boldsymbol{\nabla}_{\mathrm{h}} p_{\mathrm{atm}} + \rho_0 g \boldsymbol{\nabla}_{\mathrm{h}} \eta + g \int_z^\eta \boldsymbol{\nabla}_{\mathrm{h}} \rho' \, dz, \qquad (2.36)
\end{aligned}$$

where ρ_{s} is the density at the water surface, and ρ'_{s} the density variation at the water surface.

The first term is the atmospheric pressure gradient. It is needed, for example, to represent accurately the storm surges. It is generally obtained from atmospheric reanalysis datasets.

The second term is called the barotropic pressure gradient. It is due to the slope of the water surface. In this term, ρ'_{s} appears next to ρ_0, so that the density variations can be neglected. The elevation η is computed from the free surface equation, which is obtained by integrating the continuity equation (2.33) over the water column. The integration of the left-hand side of this continuity equation reads:

$$\begin{aligned}
&\int_{-h}^{\eta} \boldsymbol{\nabla}_{\mathrm{h}} \cdot \boldsymbol{u} \, dz + \Big[w \Big]_{-h}^{\eta} \\
&\qquad = \boldsymbol{\nabla}_{\mathrm{h}} \cdot \int_{-h}^{\eta} \boldsymbol{u} \, dz - \boldsymbol{u}_{\mathrm{s}} \cdot \boldsymbol{\nabla}_{\mathrm{h}} \eta + \boldsymbol{u}_{\mathrm{b}} \cdot \boldsymbol{\nabla}_{\mathrm{h}} (-h) + w_{\mathrm{s}} - w_{\mathrm{b}}, \qquad (2.37)
\end{aligned}$$

where h is the unperturbed height of the water column (Figure 2.3), and the subscripts "s" and "b" denote that the variables are evaluated at the surface and at the bottom of the water column, respectively. Taking into account the impermeability conditions at the water surface ($z = \eta$) and a the bottom ($z = -h$), i.e.

$$\begin{aligned}
w_{\mathrm{s}} &= \frac{\partial \eta}{\partial t} + \boldsymbol{u}_{\mathrm{s}} \cdot \boldsymbol{\nabla}_{\mathrm{h}} \eta, \qquad (2.38) \\
w_{\mathrm{b}} &= \boldsymbol{u}_{\mathrm{b}} \cdot \boldsymbol{\nabla}_{\mathrm{h}} (-h), \qquad (2.39)
\end{aligned}$$

the free surface equation reads:

$$\frac{\partial \eta}{\partial t} + \boldsymbol{\nabla}_{\mathrm{h}} \cdot \int_{-h}^{\eta} \boldsymbol{u} \, dz = 0. \qquad (2.40)$$

The third term is called the baroclinic pressure gradient and is due to the density variations. To obtain a closed system of equations, a state equation has to be defined to evaluate them:

$$\rho' = \rho'(T, S), \tag{2.41}$$

where T and S are the water temperature and the salinity, respectively. The salinity is governed by the classical tracer transport equation:

$$\frac{\partial S}{\partial t} + \boldsymbol{v} \cdot \boldsymbol{\nabla} S = \boldsymbol{\nabla} \cdot (\kappa \boldsymbol{\nabla} S), \tag{2.42}$$

where κ is the tracer diffusivity, while the temperature obeys the more complex heat equation. However, under the restrictions underlying the Boussinesq approximation, Kundu and Cohen (2002) show that the heat equation reduces to:

$$\frac{\partial T}{\partial t} + \boldsymbol{v} \cdot \boldsymbol{\nabla} T = \boldsymbol{\nabla} \cdot (\kappa_T \boldsymbol{\nabla} T), \tag{2.43}$$

where κ_T is the thermal diffusivity.

The two-dimensional shallow-water equations

To move from the three-dimensional baroclinic equations to the two-dimensional shallow-water equations, the baroclinic pressure gradient must be neglected. For studying coastal and marine flows, this is likely to be unacceptable. However, the Scheldt Estuary is very shallow and vertically well-mixed, so that the vertical variations of the density are rather small (Baeyens et al., 1998c). Moreover, the horizontal variations of water temperature are very small, and the horizontal salinity range from fresh to salty waters extend over a large distance. The horizontal variations of the density are therefore also rather small. For these reasons, it is not uncommon to use a barotropic model to study the Scheldt Estuary (Arndt et al., 2007; Vanderborght et al., 2007).

Neglecting the baroclinic pressure gradient, and taking advantage of the continuity equation (2.33), the horizontal momentum budget equation (2.34) rewrites:

$$\frac{\partial \boldsymbol{u}}{\partial t} + \boldsymbol{\nabla}_{\mathrm{h}} \cdot (\boldsymbol{u}\boldsymbol{u}) + \frac{\partial}{\partial z}(w\boldsymbol{u}) + f\boldsymbol{e}_z \times \boldsymbol{u} = - \frac{1}{\rho_0} \boldsymbol{\nabla}_{\mathrm{h}} p_{\mathrm{atm}} - g \boldsymbol{\nabla}_{\mathrm{h}} \eta + \frac{\partial}{\partial z}\left(\nu_{\mathrm{t}} \frac{\partial \boldsymbol{u}}{\partial z} \right). \tag{2.44}$$

The two-dimensional shallow-water equations are obtained by integrating the continuity equation (2.33) and the horizontal momentum budget equation (2.44) over the water column, using the impermeability conditions (2.38) and (2.39), and defining a horizontal depth-averaged velocity vector as

$$\overline{\boldsymbol{u}} = \frac{1}{H}\int_{-h}^{\eta} \boldsymbol{u}\, dz. \tag{2.45}$$

The integration of the continuity equation over the water column leads to the free surface equation (2.40). Taking the definition of the depth-averaged velocity into accound, it reads:

$$\frac{\partial \eta}{\partial t} + \boldsymbol{\nabla}_{\mathrm{h}} \cdot \overline{\boldsymbol{u}} = 0. \tag{2.46}$$

The integration of the horizontal momentum budget equation (2.44) needs longer developments, so that the details are shown term by term:

$$\int_{-h}^{\eta} \frac{\partial \boldsymbol{u}}{\partial t}\, dz = \frac{\partial}{\partial t}(H\overline{\boldsymbol{u}}) - \boldsymbol{u}_{\mathrm{s}}\frac{\partial \eta}{\partial t}, \tag{2.47}$$

$$\begin{aligned}\int_{-h}^{\eta} \boldsymbol{\nabla}_{\mathrm{h}} \cdot (\boldsymbol{u}\boldsymbol{u})\, dz &= \boldsymbol{\nabla}_{\mathrm{h}} \cdot \int_{-h}^{\eta} \boldsymbol{u}\boldsymbol{u}\, dz \\ &\quad -\boldsymbol{u}_{\mathrm{s}}\boldsymbol{u}_{\mathrm{s}} \cdot \boldsymbol{\nabla}_{\mathrm{h}}\eta + \boldsymbol{u}_{\mathrm{b}}\boldsymbol{u}_{\mathrm{b}} \cdot \boldsymbol{\nabla}_{\mathrm{h}}(-h) \\ &= \boldsymbol{\nabla}_{\mathrm{h}} \cdot (H\overline{\boldsymbol{u}}\overline{\boldsymbol{u}}) + \boldsymbol{\nabla}_{\mathrm{h}} \cdot \int_{-h}^{\eta} (\boldsymbol{u}-\overline{\boldsymbol{u}})(\boldsymbol{u}-\overline{\boldsymbol{u}})\, dz \\ &\quad -\boldsymbol{u}_{\mathrm{s}}\boldsymbol{u}_{\mathrm{s}} \cdot \boldsymbol{\nabla}_{\mathrm{h}}\eta + \boldsymbol{u}_{\mathrm{b}}\boldsymbol{u}_{\mathrm{b}} \cdot \boldsymbol{\nabla}_{\mathrm{h}}(-h),\end{aligned} \tag{2.48}$$

$$\begin{aligned}\int_{-h}^{\eta} \frac{\partial}{\partial z}(w\boldsymbol{u})\, dz &= \Big[w\boldsymbol{u}\Big]_{-h}^{\eta} \\ &= w_{\mathrm{s}}\boldsymbol{u}_{\mathrm{s}} - w_{\mathrm{b}}\boldsymbol{u}_{\mathrm{b}} \\ &= \boldsymbol{u}_{\mathrm{s}}\frac{\partial \eta}{\partial t} + \boldsymbol{u}_{\mathrm{s}}\boldsymbol{u}_{\mathrm{s}} \cdot \boldsymbol{\nabla}_{\mathrm{h}}\eta - \boldsymbol{u}_{\mathrm{b}}\boldsymbol{u}_{\mathrm{b}} \cdot \boldsymbol{\nabla}_{\mathrm{h}}(-h),\end{aligned} \tag{2.49}$$

$$\int_{-h}^{\eta} f\boldsymbol{e}_z \times \boldsymbol{u}\, dz = f\boldsymbol{e}_z \times (H\overline{\boldsymbol{u}}), \tag{2.50}$$

$$\int_{-h}^{\eta} -\frac{1}{\rho_0}\boldsymbol{\nabla}_{\mathrm{h}} p_{\mathrm{atm}}\, dz = -\frac{H}{\rho_0}\boldsymbol{\nabla}_{\mathrm{h}} p_{\mathrm{atm}}, \tag{2.51}$$

$$\int_{-h}^{\eta} -g\boldsymbol{\nabla}_{\mathrm{h}}\eta\, dz \;=\; -gH\boldsymbol{\nabla}_{\mathrm{h}}\eta, \tag{2.52}$$

$$\int_{-h}^{\eta} \frac{\partial}{\partial z}\left(\nu_{\mathrm{t}}\frac{\partial \boldsymbol{u}}{\partial z}\right) dz \;=\; \left[\nu_{\mathrm{t}}\frac{\partial \boldsymbol{u}}{\partial z}\right]_{-h}^{\eta}. \tag{2.53}$$

Among those expressions, some terms cannot be calculated explicitly in a horizontal two-dimensional model. They must be parameterized. Moreover, some additional processes must be taken into account.

1. Phenomena are occurring at smaller scales than what the grid size allows. They are generally thought to be of a dissipative nature. By analogy with three-dimensional turbulence, it is commonly assumed that this can be treated using an eddy viscosity formulation in terms of the depth-averaged velocity gradient (Vreugdenhil, 1994), i.e. by adding the following term in the right-hand side of the depth-averaged horizontal momentum budget equation:

   $$\boldsymbol{\nabla}_{\mathrm{h}} \cdot (H\nu_{\mathrm{h}}\boldsymbol{\nabla}_{\mathrm{h}}\overline{\boldsymbol{u}}), \tag{2.54}$$

   where ν_{h} is the horizontal subgrid viscosity. This parameterization has the advantage to have the form of the divergence of a tensor (although not a symmetrical one) in the conservative formulation, and that is dissipative (Shchepetkin and O'Brien, 1996). Moreover, the dissipation only occurs when the velocity is not constant. The horizontal subgrid viscosity ν_{h} must be parameterized in terms of the other variables and the size of the grid. Typical values for the applications of this doctoral dissertation range from 1 to 100 $\mathrm{m^2\,s^{-1}}$.

2. In equation (2.48), the differential advection term,

   $$\boldsymbol{\nabla}_{\mathrm{h}} \cdot \int_{-h}^{\eta} (\boldsymbol{u} - \overline{\boldsymbol{u}})(\boldsymbol{u} - \overline{\boldsymbol{u}})\, dz,$$

   describes a lateral momentum exchange due to differences in velocity over the depth of the flow, i.e. the shear effect. This may also be treated using an eddy viscosity formulation in terms of the depth-averaged velocity gradient, by parameterizing the differential advection term as follows (Abbot and Price, 1994):

   $$-\boldsymbol{\nabla}_{\mathrm{h}} \cdot \int_{-h}^{\eta} (\boldsymbol{u} - \overline{\boldsymbol{u}})(\boldsymbol{u} - \overline{\boldsymbol{u}})\, dz \triangleq \boldsymbol{\nabla}_{\mathrm{h}} \cdot (H\boldsymbol{\nu}_{\mathrm{s}} \cdot \boldsymbol{\nabla}_{\mathrm{h}}\overline{\boldsymbol{u}}), \tag{2.55}$$

where the shear viscosity $\boldsymbol{\nu}_\mathrm{s}$ is a tensor. However, the components of the shear viscosity being the order of 1 $\mathrm{m}^2\,\mathrm{s}^{-1}$ (Abbot and Price, 1994), this term is often much smaller than the subgrid viscosity term (2.54), and is therefore neglected.

3. The right-hand part of equation (2.53) is generally parameterized as follows:

$$\left[\nu_\mathrm{t}\frac{\partial \boldsymbol{u}}{\partial z}\right]_{-h}^{\eta} \triangleq \frac{\boldsymbol{\tau}^\mathrm{s}-\boldsymbol{\tau}^\mathrm{b}}{\rho_0}, \tag{2.56}$$

where $\boldsymbol{\tau}^\mathrm{s}$ and $\boldsymbol{\tau}^\mathrm{b}$ are called the surface and bottom stress vectors, respectively. The surface stress is an important driving force due to the wind. It needs to be parameterized in terms of external data. The bottom stress accounts for the energy dissipation due to the bottom roughness. It must be parameterized in terms of the other variables in order to close the system of equations.

The horizontal momentum budget equation becomes therefore:

$$\begin{aligned}\frac{\partial}{\partial t}(H\overline{\boldsymbol{u}}) + \boldsymbol{\nabla}_\mathrm{h}\cdot(H\overline{\boldsymbol{u}\boldsymbol{u}}) + f\boldsymbol{e}_z\times H\overline{\boldsymbol{u}} \\ = -\frac{H}{\rho_0}\boldsymbol{\nabla}_\mathrm{h}p_\mathrm{atm} - gH\boldsymbol{\nabla}_\mathrm{h}\eta + \boldsymbol{\nabla}_\mathrm{h}\cdot(H\nu_\mathrm{h}\boldsymbol{\nabla}_\mathrm{h}\overline{\boldsymbol{u}}) + \frac{\boldsymbol{\tau}^\mathrm{s}-\boldsymbol{\tau}^\mathrm{b}}{\rho_0}.\end{aligned} \tag{2.57}$$

However, it is generally written in a non-conservative form, using equation (2.46), and dividing by H:

$$\begin{aligned}\frac{\partial\overline{\boldsymbol{u}}}{\partial t} + \overline{\boldsymbol{u}}\cdot(\boldsymbol{\nabla}_\mathrm{h}\overline{\boldsymbol{u}}) + f\boldsymbol{e}_z\times\overline{\boldsymbol{u}} \\ = -\frac{1}{\rho_0}\boldsymbol{\nabla}_\mathrm{h}p_\mathrm{atm} - g\boldsymbol{\nabla}_\mathrm{h}\eta + \frac{1}{H}\boldsymbol{\nabla}_\mathrm{h}\cdot(H\nu_\mathrm{h}\boldsymbol{\nabla}_\mathrm{h}\overline{\boldsymbol{u}}) + \frac{\boldsymbol{\tau}^\mathrm{s}-\boldsymbol{\tau}^\mathrm{b}}{\rho_0 H}.\end{aligned} \tag{2.58}$$

And since only two-dimensional horizontal flows are considered in the present work, the subscript "h" and the bars overlining depth-averaged variables are omitted in all what follows in this chapter. The subscripts "0" of the mean water density is also removed. The shallow water equations are therefore written:

$$\frac{\partial \eta}{\partial t} + \boldsymbol{\nabla} \cdot (H\boldsymbol{u}) = 0, \tag{2.59}$$

$$\frac{\partial \boldsymbol{u}}{\partial t} + \boldsymbol{u} \cdot (\boldsymbol{\nabla} \boldsymbol{u}) + f\boldsymbol{e}_z \times \boldsymbol{u} = -\frac{1}{\rho}\boldsymbol{\nabla} p_{\mathrm{atm}} - g\boldsymbol{\nabla}\eta + \frac{1}{H}\boldsymbol{\nabla} \cdot (H\nu\boldsymbol{\nabla}\boldsymbol{u}) + \frac{\boldsymbol{\tau}^{\mathrm{s}} - \boldsymbol{\tau}^{\mathrm{b}}}{\rho H}. \tag{2.60}$$

Different parameterizations of ν, $\boldsymbol{\tau}^{\mathrm{s}}$ and $\boldsymbol{\tau}^{\mathrm{b}}$ are found in the literature, depending on the application. Those of use in this tesis are detailed further, when needed.

2.3 Numerical model

2.3.1 Spatial discretization

Traditionally, ocean models are built using finite difference methods on Cartesian grids (Griffies et al., 2000). However, recently finite elements methods caught ocean modeling community's attention (Piggott et al., 2008; Timmermann et al., 2009; Blaise et al., 2010a). The main advantage of finite element methods is the possibility to use unstructured meshes, which allow a better representation of the coastlines and an increase of resolution where it is needed. This is believed to compensate the higher computer cost of the finite element technique. For the simulations of this work, only triangular meshes are dealt with. They are generated using the software GMSH (Lambrechts et al., 2008a; Geuzaine and Remacle, 2009). However, the use of quadrilateral meshes should be considered in the future (Remacle et al., 2010).

The unknown fields are evaluated on nodes. To each node is associated a shape function. The number and the location of the nodes, as the nature of the definition of the functions, depend on the type of finite element used. A critical issue for applying the finite element method in oceanography is to find a suitable finite element pair for η and $\boldsymbol{u}$. This pair should represent geophysical flows correctly and not allow the existence of spurious computational modes. Several associations have been tested using SLIM (Hanert et al., 2002, 2004; Comblen et al., 2010b), but only the $P_1^{\mathrm{DG}} - P_1^{\mathrm{DG}}$ pair is considered in the present work, for its ability to represent advective processes.

Using P_1^{DG} elements, the approximations of the unknown fields are piecewise linear and the nodes are located on the vertices of the mesh. Using classical P_1 elements, the nodal value at one vertex is shared by all the neighboring triangles. It is not the case with discontinuous Galerkin (DG) elements. The approximations are therefore discontinuous at the interface of the triangles (Figure 2.4). If the two-dimensional model domain Ω is divided into a set of non overlapping elements Ω_e, the P_1^{DG} approximations of the unknown fields η and $\boldsymbol{u}$ read:

$$\eta \simeq \eta^h = \sum_{j=1}^{3N_e} \eta_j \phi_j, \tag{2.61}$$

$$\boldsymbol{u} \simeq \boldsymbol{u}^h = \sum_{j=1}^{3N_e} \boldsymbol{u}_j \phi_j, \tag{2.62}$$

where η_j and $\boldsymbol{u}_j$ are the elevation and velocity nodal values at node j, respectively, and ϕ_j is the associated shape functions. On the element related to node j, ϕ_j is a linear function of the spatial coordinates, equal to 1 on node j and to 0 on the two other nodes. It is equal to 0 everywhere else. To compute the nodal values, it is necessary to write the weak formulation of equations (2.59) and (2.60).

Weak formulation

The weak formulation of equations (2.59) and (2.60) is obtained by integrating them over the whole domain of interest, against a set of admissible test functions $\hat{\eta}$ and $\hat{\boldsymbol{u}}$, respectively, belonging to the suitable functional space (Hanert et al., 2002). In what follows, $< \cdot >_e$ denotes a surface integral over the element Ω_e and $\ll \cdot \gg_e$ a contour integral over its boundary Γ_e; $\boldsymbol{n}$ is the unit outward normal vector to the element boundary.

The weak formulation of the continuity equation (2.59) reads therefore:

$$\sum_e \left(< \frac{\partial \eta}{\partial t} \hat{\eta} >_e + < \boldsymbol{\nabla} \cdot (H\boldsymbol{u}) \hat{\eta} >_e \right) = 0. \tag{2.63}$$

Integrating by parts the second term leads to:

$$\sum_e \left(< \frac{\partial \eta}{\partial t} \hat{\eta} >_e + < \boldsymbol{\nabla} \cdot (H\boldsymbol{u}\hat{\eta}) >_e - < H\boldsymbol{u} \cdot \boldsymbol{\nabla} \hat{\eta} >_e \right) = 0. \tag{2.64}$$

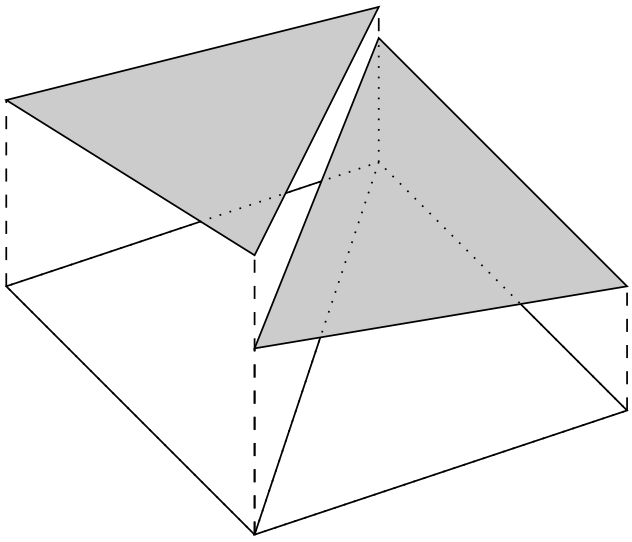

Figure 2.4: Representation of the P_1^{DG} approximation of a field, and illustration of the discontinuity at element interfaces.

Using the Gauss-Ostrogradsky theorem, and defining $u_n = \boldsymbol{u} \cdot \boldsymbol{n}$ as the component of the velocity $\boldsymbol{u}$ that is normal to the element boundary Γ_e, the weak formulation becomes:

$$\sum_e \left(< \frac{\partial \eta}{\partial t} \hat{\eta} >_e + \ll H u_n \hat{\eta} \gg_e - < H \boldsymbol{u} \cdot \boldsymbol{\nabla} \hat{\eta} >_e \right) = 0. \qquad (2.65)$$

The weak formulation of the momentum budget equation (2.60) reads:

$$\begin{aligned} &\sum_e \left(< \frac{\partial \boldsymbol{u}}{\partial t} \cdot \hat{\boldsymbol{u}} >_e + < \boldsymbol{u} \cdot (\boldsymbol{\nabla} \boldsymbol{u}) \cdot \hat{\boldsymbol{u}} >_e + < f(\boldsymbol{e}_z \times \boldsymbol{u}) \cdot \hat{\boldsymbol{u}} >_e \right) \\ &= \sum_e \left(-\frac{1}{\rho} < (\boldsymbol{\nabla} p_{\mathrm{atm}}) \cdot \hat{\boldsymbol{u}} >_e - g < (\boldsymbol{\nabla} \eta) \cdot \hat{\boldsymbol{u}} >_e \right. \\ &\qquad \left. + < \frac{1}{H} \boldsymbol{\nabla} \cdot (H \nu \boldsymbol{\nabla} \boldsymbol{u}) \cdot \hat{\boldsymbol{u}} >_e + < \frac{\boldsymbol{\tau}^{\mathrm{s}} - \boldsymbol{\tau}^{\mathrm{b}}}{\rho H} \cdot \hat{\boldsymbol{u}} >_e \right). \end{aligned} \qquad (2.66)$$

Following what has been done to obtain equation (2.65) from equation (2.63), terms with spatial derivatives may be developed further. For example, the advection term becomes:

$$\begin{aligned} < \boldsymbol{u} \cdot (\boldsymbol{\nabla u}) \cdot \hat{\boldsymbol{u}} >_e &= < \boldsymbol{\nabla} \cdot (\boldsymbol{uu} \cdot \hat{\boldsymbol{u}}) >_e - < \boldsymbol{\nabla} \cdot (\boldsymbol{u}\hat{\boldsymbol{u}}) \cdot \boldsymbol{u} >_e \\ &= \ll u_n \boldsymbol{u} \cdot \hat{\boldsymbol{u}} \gg_e - < \boldsymbol{\nabla} \cdot (\boldsymbol{u}\hat{\boldsymbol{u}}) \cdot \boldsymbol{u} >_e . \quad (2.67) \end{aligned}$$

The gravity term is developed as follows:

$$\begin{aligned} -g < (\boldsymbol{\nabla}\eta) \cdot \hat{\boldsymbol{u}} >_e &= -g < \boldsymbol{\nabla} \cdot (\hat{\boldsymbol{u}}\eta) >_e + g < \eta \boldsymbol{\nabla} \cdot \hat{\boldsymbol{u}} >_e \\ &= -g \ll \hat{u}_n \eta \gg_e + g < \eta \boldsymbol{\nabla} \cdot \hat{\boldsymbol{u}} >_e, \quad (2.68) \end{aligned}$$

where $\hat{u}_n = \hat{\boldsymbol{u}} \cdot \boldsymbol{n}$ is the component of the vectorial test function $\hat{\boldsymbol{u}}$ that is normal to the element boundary Γ_e. Finally, the dissipative term is written:

$$\begin{aligned} &< \frac{1}{H} \boldsymbol{\nabla} \cdot (H\nu \boldsymbol{\nabla u}) \cdot \hat{\boldsymbol{u}} >_e \\ &\quad = < \boldsymbol{\nabla} \cdot \big(\nu(\boldsymbol{\nabla u}) \cdot \hat{\boldsymbol{u}}\big) >_e - < H\nu(\boldsymbol{\nabla u}) : \left(\boldsymbol{\nabla} \left(\frac{\hat{\boldsymbol{u}}}{H} \right) \right)^t >_e \\ &\quad = \ll \boldsymbol{n} \cdot \big(\nu(\boldsymbol{\nabla u}) \cdot \hat{\boldsymbol{u}}\big) \gg_e \\ &\qquad - < H\nu(\boldsymbol{\nabla u}) : \left(\frac{1}{H} \boldsymbol{\nabla} \hat{\boldsymbol{u}} - (\boldsymbol{\nabla} H) \frac{\hat{\boldsymbol{u}}}{H^2} \right)^t >_e \\ &\quad = \ll \nu \frac{\partial \boldsymbol{u}}{\partial n} \cdot \hat{\boldsymbol{u}} \gg_e - < \nu(\boldsymbol{\nabla u}) : (\boldsymbol{\nabla} \hat{\boldsymbol{u}})^t >_e \\ &\qquad + < \frac{\nu}{H} (\boldsymbol{\nabla} H) \cdot (\boldsymbol{\nabla u}) \cdot \hat{\boldsymbol{u}} >_e, \quad (2.69) \end{aligned}$$

where $\partial/\partial n$ is the spatial derivative along the direction $\boldsymbol{n}$ normal to the element boundary, and the scalar product between two tensors is defined as $\boldsymbol{A} : \boldsymbol{B} = \sum_i \sum_j A_{ij} B_{ji}$.

The weak formulation of the momentum budget equation (2.66) reads therefore:

$$\begin{aligned} \sum_e \Bigg(&< \frac{\partial \boldsymbol{u}}{\partial t} \cdot \hat{\boldsymbol{u}} >_e + \ll u_n \boldsymbol{u} \cdot \hat{\boldsymbol{u}} \gg_e - < \boldsymbol{\nabla} \cdot (\boldsymbol{u}\hat{\boldsymbol{u}}) \cdot \boldsymbol{u} >_e \\ &+ < f(\boldsymbol{e}_z \times \boldsymbol{u}) \cdot \hat{\boldsymbol{u}} >_e \Bigg) \end{aligned}$$

$$= \sum_e \Bigg(-\frac{1}{\rho} < (\boldsymbol{\nabla} p_{\text{atm}}) \cdot \hat{\boldsymbol{u}} >_e - g \ll \hat{u}_n \eta \gg_e + g < \eta \boldsymbol{\nabla} \cdot \hat{\boldsymbol{u}} >_e$$
$$+ \ll \nu \frac{\partial \boldsymbol{u}}{\partial n} \cdot \hat{\boldsymbol{u}} \gg_e - < \nu (\boldsymbol{\nabla} \boldsymbol{u}) : (\boldsymbol{\nabla} \hat{\boldsymbol{u}})^t >_e$$
$$+ < \frac{\nu}{H} (\boldsymbol{\nabla} H) \cdot (\boldsymbol{\nabla} \boldsymbol{u}) \cdot \hat{\boldsymbol{u}} >_e + < \frac{\boldsymbol{\tau}^{\text{s}} - \boldsymbol{\tau}^{\text{b}}}{\rho H} \cdot \hat{\boldsymbol{u}} >_e \Bigg). \quad (2.70)$$

Finite element formulation

The finite element formulation of equations (2.59) and (2.60) is obtained by replacing η and $\boldsymbol{u}$ by their finite element approximations η^h and $\boldsymbol{u}^h$ in equations (2.65) and (2.70) (Hanert et al., 2005):

$$\sum_e \Bigg(< \frac{\partial \eta^h}{\partial t} \hat{\eta} >_e + \ll \Big(h + \big(\eta^h\big)^* \Big) \big(u_n^h\big)^* \hat{\eta} \gg_e$$
$$- < H^h \boldsymbol{u}^h \cdot \boldsymbol{\nabla} \hat{\eta} >_e \Bigg) = 0, \quad (2.71)$$

$$\sum_e \Bigg(< \frac{\partial \boldsymbol{u}^h}{\partial t} \cdot \hat{\boldsymbol{u}} >_e + \ll \big(u_n^h\big)^* \big(\boldsymbol{u}^h\big)^* \cdot \hat{\boldsymbol{u}} \gg_e$$
$$- < \boldsymbol{\nabla} \cdot (\boldsymbol{u}^h \hat{\boldsymbol{u}}) \cdot \boldsymbol{u}^h >_e + < f (\boldsymbol{e}_z \times \boldsymbol{u}^h) \cdot \hat{\boldsymbol{u}} >_e \Bigg)$$

$$= \sum_e \Bigg(-\frac{1}{\rho} < (\boldsymbol{\nabla} p_{\text{atm}}) \cdot \hat{\boldsymbol{u}} >_e - g \ll \hat{u}_n \big(\eta^h\big)^* \gg_e + g < \eta^h \boldsymbol{\nabla} \cdot \hat{\boldsymbol{u}} >_e$$
$$+ \ll \nu \left\{ \frac{\partial \boldsymbol{u}^h}{\partial n} \right\} \cdot \hat{\boldsymbol{u}} \gg_e - < \nu (\boldsymbol{\nabla} \boldsymbol{u}^h) : (\boldsymbol{\nabla} \hat{\boldsymbol{u}})^t >_e$$
$$+ < \frac{\nu}{H^h} (\boldsymbol{\nabla} H^h) \cdot (\boldsymbol{\nabla} \boldsymbol{u}^h) \cdot \hat{\boldsymbol{u}} >_e + < \frac{\boldsymbol{\tau}^{\text{s}} - \boldsymbol{\tau}^{\text{b}}}{\rho H^h} \cdot \hat{\boldsymbol{u}} >_e \Bigg), \quad (2.72)$$

where $u_n^h = \boldsymbol{u}^h \cdot \boldsymbol{n}$ and $H^h = h + \eta^h$. Since the approximations of the unknown fields are discontinuous on the element boundaries, their evaluation on the contour integrals needs to be uniquely defined for both neighboring elements of the interface.

In the contour integrals of the non viscous terms, it is usual to define a Riemann solver that relies on the characteristic structure of the equations to determine $\left(\eta^h\right)^*$ and $\left(\boldsymbol{u}^h\right)^*$. It takes into account the values of η^h and $\boldsymbol{u}^h$ from the own element (internal values) and from its neighbor (external values), adding just enough numerical dissipation to keep the scheme stable. The Riemann solver used here is detailed by Comblen et al. (2010b). When computing contour integrals on the boundary Γ of the model domain, elements have no neighbor. In the case of an open boundary, the external values are estimated using external data. In the case of a coast, the mass flux through the boundary is cancelled to insure the impermeability condition $u_n = 0$, while the external value of η^h is taken equal to the internal one.

In the contour integrals of the viscous term, it is natural to take $\{\partial \boldsymbol{u}^h / \partial n\}$ as the mean of the internal and external values, because the horizontal viscosity is an isotropic phenomenon. However, when using a discontinuous discretization method for the velocity field, a specific treatment is needed to obtain a stable and accurate representation of the viscous effects. In SLIM, the non-symmetric interior penalty (NIP) method is used. It consists in adding the following term in the right-hand side of equation (2.72):

$$-\sum_e \ll \sigma \hat{\boldsymbol{u}} \cdot \left[\boldsymbol{u}^h\right] \gg_e, \tag{2.73}$$

where σ is the penalty parameter and $\left[\boldsymbol{u}^h\right]$ is the velocity jump:

$$\left[\boldsymbol{u}^h\right] = \frac{\boldsymbol{u}^h_{\text{int}} - \boldsymbol{u}^h_{\text{ext}}}{2}, \tag{2.74}$$

where $\boldsymbol{u}^h_{\text{int}}$ and $\boldsymbol{u}^h_{\text{ext}}$ are the internal and external values of $\boldsymbol{u}^h$, respectively. A parameterization of σ is proposed by Shahbazi (2005):

$$\sigma = \frac{\nu(p+1)(p+2)}{d_e}, \tag{2.75}$$

where p is here the interpolation order of the approximation of the field considered ($p = 1$ for P_1^{DG} elements), and d_e is a typical length scale of the element Ω_e. On the boundary Γ of the model domain, the external value $\boldsymbol{u}^h_{\text{ext}}$ is determined as in the contour integrals from the non viscous terms.

To illustrate what is done when computing the viscous contour integral on the boundary Γ of the model domain, it is necessary to develop

it as follows:

$$\ll \nu \left\{ \frac{\partial \boldsymbol{u}^h}{\partial n} \right\} \cdot \hat{\boldsymbol{u}} \gg_e = \ll \nu \left\{ \frac{\partial u_n^h}{\partial n} \right\} \hat{u}_n \gg_e + \ll \nu \left\{ \frac{\partial u_t^h}{\partial n} \right\} \hat{u}_t \gg_e, \quad (2.76)$$

where u_t^h and $\hat{u}_t$ are the components of $\boldsymbol{u}^h$ and $\hat{\boldsymbol{u}}$, respectively, that are tangential to the element boundary Γ_e. On the boundary Γ of the model domain, the external value of either $\partial u_n^h/\partial n$ or $\partial u_t^h/\partial n$ is determined by the boundary condition required by the viscous term. The external value of the other normal derivative is taken equal to the internal value. Typically, in the case of a coast, the viscous boundary condition is of the form:

$$\nu \frac{\partial u_t}{\partial n} = \lambda u_t, \quad (2.77)$$

where λ is the slip coefficient. Free slip is used for open boundaries by taking $\lambda = 0$. No slip is obtained with $\lambda \to \infty$. Partial slip is used for the coasts by taking any other positive value of the slip coefficient (Haidvogel et al., 1991).

Galerkin procedure

The Galerkin procedure amounts to replace $\hat{\eta}$ by ϕ_i for $1 \leq i \leq 3N_e$ in equation (2.71) and $\hat{\boldsymbol{u}}$ by $(\phi_i, 0)$ then $(0, \phi_i)$ for $1 \leq i \leq 3N_e$ in equation (2.72) (Hanert et al., 2005). This results in a system of $9N_e$ ordinary differential equations, which are necessary to compute the $3N_e$ nodal values of η^h and the $6N_e$ nodal values of $\boldsymbol{u}^h$ introduced in relations (2.61) and (2.62). This system can be synthesized on the following matrix form:

$$\boldsymbol{A} \cdot \frac{d\boldsymbol{s}}{dt} = \boldsymbol{b}\big(t, \boldsymbol{s}(t)\big). \quad (2.78)$$

The matrix $\boldsymbol{A}$ is a $(9N_e, 9N_e)$ squared matrix and is defined as follows[3]:

$$\boldsymbol{A} = \left[A_{ij}\right] = \begin{bmatrix} \left[A_{ij}^{\eta}\right] & 0 & 0 \\ 0 & \left[A_{ij}^{u}\right] & 0 \\ 0 & 0 & \left[A_{ij}^{v}\right] \end{bmatrix}, \tag{2.79}$$

where $\left[A_{ij}^{\eta}\right]$, $\left[A_{ij}^{u}\right]$ and $\left[A_{ij}^{v}\right]$ are $(3N_e, 3N_e)$ squared matrices with

$$A_{ij}^{\eta} = A_{ij}^{u} = A_{ij}^{v} \quad = \quad < \phi_i \phi_j >_{e(i)}, \tag{2.80}$$

the subscript $e(i)$ pointing to the element for which ϕ_i is not zero everywhere. The $(9N_e, 1)$ vector $\boldsymbol{s}$ gathers all the nodal values of the problem:

$$\boldsymbol{s} = \left[s_j\right] = \begin{bmatrix} \left[\eta_j\right] \\ \left[u_j\right] \\ \left[v_j\right] \end{bmatrix}, \tag{2.81}$$

where $\left[\eta_j\right]$ is a $(3N_e, 1)$ vector that gathers the nodal values of the elevation field η, and $\left[u_j\right]$ and $\left[v_j\right]$ are $(3N_e, 1)$ vectors that gather the nodal values of the components of the velocity field, respectively u and v. The left-hand part of equation (2.78) corresponds to the terms of equations (2.71) and (2.72) that contain time derivatives. The $(9N_e, 1)$

[3] In practice, for numerical efficiency reasons, the mass matrix $\boldsymbol{A}$ is not built using blocks of equations, as it is presented here for the reader's convenience, but rather using blocks of elements; this remark also applies to the vectors $\boldsymbol{b}$ and $\boldsymbol{s}$.

vector $\boldsymbol{b}$ gathers all the other terms and is defined as follows:

$$\boldsymbol{b} = \left[b_i\right] = \begin{bmatrix} \left[b_i^{\eta \mathrm{s}}\right] + \left[b_i^{\eta \mathrm{c}}\right] \\ \left[b_i^{u \mathrm{s}}\right] + \left[b_i^{u \mathrm{c}}\right] \\ \left[b_i^{v \mathrm{s}}\right] + \left[b_i^{v \mathrm{c}}\right] \end{bmatrix}, \tag{2.82}$$

where all the sub-vectors are $(3N_e, 1)$ vectors: $b_i^{\eta \mathrm{s}}$ and $b_i^{\eta \mathrm{c}}$ gather respectively the surface and contour integrals from equation (2.71) with $\hat{\eta} = \phi_i$, $b_i^{u \mathrm{s}}$ and $b_i^{u \mathrm{c}}$ gather respectively the surface and contour integrals from equation (2.72) with $\hat{\boldsymbol{u}} = (\phi_i, 0)$, and $b_i^{v \mathrm{s}}$ and $b_i^{v \mathrm{c}}$ gather respectively the surface and contour integrals from equation (2.72) with $\hat{\boldsymbol{u}} = (0, \phi_i)$.

2.3.2 Temporal integration

To integrate equation (2.78) in time, Runge-Kutta methods are quite popular (Butcher, 1996; Ascher et al., 1997). With such methods, $\boldsymbol{s}^{n+1}$, the vector containing the nodal values at time t^{n+1}, is computed from $\boldsymbol{s}^n$, the vector containing the nodal values at time t^n, using the following equation:

$$\boldsymbol{A} \cdot \boldsymbol{s}^{n+1} = \boldsymbol{A} \cdot \boldsymbol{s}^n + \Delta t \sum_{i=1}^{s} \beta_i \boldsymbol{k}_i, \tag{2.83}$$

where

$$\boldsymbol{k}_i = \boldsymbol{b}\left(t^n + \gamma_i \Delta t, \boldsymbol{s}^n + \sum_{j=1}^{s} \alpha_{ij} \Delta t \ \boldsymbol{k}_j \right), \tag{2.84}$$

where $\Delta t = t^{n+1} - t^n$, and the functions $\boldsymbol{k}_i$ may be seen as evaluations of $\boldsymbol{b}$ at sub-time steps.

To specify a particular method, the number of stages s, and the value of the coefficients α_{ij}, β_i and γ_i need to be provided. These data are usually arranged in a mnemonic device, known as the Butcher tableau

of the method:

$$\begin{array}{c|c} \left[\gamma_i\right] & \left[\alpha_{ij}\right] \\ \hline & \left[\beta_i\right]^t \end{array}, \tag{2.85}$$

where $\left[\alpha_{ij}\right]$ is a (s, s) squared matrix, and $\left[\beta_i\right]$ and $\left[\gamma_i\right]$ are $(s, 1)$ vectors. For the method to be consistent, the following constraint must be satisfied:

$$\sum_{j=1}^{s} \alpha_{ij} = \gamma_i \qquad \text{for } 1 < i \leq s. \tag{2.86}$$

As every time integration method, Runge-Kutta methods are classified into two distinct families, i.e. explicit and implicit methods. The choice of the suitable method is not obvious and in fact depends on the flow under study. Both cases are investigated here.

Explicit methods

Using explicit methods, the only non-vanishing entries of $\left[\alpha_{ij}\right]$ are located in the left lower triangular part of the matrix with zeros on the diagonal too. This way, every function $\boldsymbol{k}_i$ only depends on the nodal values evaluated at previous sub-time steps, so that equation (2.83) leads to simple linear systems to solve. Explicit methods have therefore the advantage to be relatively easy to implement. Moreover, their efficiency is enhanced when dealing with parallel computing, in that the computing time theoretically scales with the number of computers. However, the Courant-Friedrichs-Lewy (CFL) condition must be satisfied:

$$\frac{\|\boldsymbol{u}\|\Delta t}{d_e} < C, \tag{2.87}$$

where $\|\boldsymbol{u}\|$ is the norm of the velocity $\boldsymbol{u}$, d_e is the characteristic length of the triangle Ω_e, and C is a dimensionless constant which depends on the particular equation to be solved and the time integration scheme used. The longest permissible time step is therefore restricted by the smallest triangles.

Two different explicit Runge-Kutta schemes are used in this study. The simple explicit first-order Runge-Kutta (ERK1) scheme, also know

as the Euler explicit scheme, is above all used to illustrate some theoretical aspects of the implementation of the model. It is defined by the simplest Butcher tableau:

$$\begin{array}{c|c} 0 & 0 \\ \hline & 1 \end{array}. \tag{2.88}$$

The explicit scheme mostly used in this work is the classical explicit second-order Runge-Kutta (ERK2) scheme, also known as the Heun explicit method, whose coefficients are given by the following Butcher tableau:

$$\begin{array}{c|cc} 0 & 0 & 0 \\ 1 & 1 & 0 \\ \hline & 1/2 & 1/2 \end{array}. \tag{2.89}$$

Implicit methods

Using implicit methods, there is no restriction on the values of the entries of $\left[\alpha_{ij}\right]$, so that equation (2.83) leads to very complex non-linear systems to solve. However, restricting to diagonally-implicit Runge-Kutta (DIRK) methods, the entries of the right upper triangular part of the matrix are zeros, while the diagonal entries are not. This way, the different sub-time steps can be evaluated in sequence (Butcher, 1996). But still, a non-linear iterative solver is needed at each sub-time step. Implicit methods have therefore the drawback to be more difficult to implement. Moreover, the efficiency of parallel computing is not warranted. On the other hand, they are not constrained by the CFL condition allowing the use of larger time steps. The only restriction is the need to resolve correctly the physics.

The implicit scheme mostly used in this work is the diagonally-implicit second-order Runge-Kutta method (DIRK222), whose coefficients are given by the following Butcher tableau:

$$\begin{array}{c|cc} \delta & \delta & 0 \\ 1 & 1-\delta & \delta \\ \hline & 1-\delta & \delta \end{array}, \tag{2.90}$$

with $\delta = (2 - \sqrt{2})/2$.

2.4 Modeling the tidal motion in the North Sea

At this stage, the model is not yet able to reproduce the hydrodynamics in the Scheldt Estuary. Indeed, the tidal oscillations of the free surface cause the periodical emergence of the bottom in some very shallow areas, leading to zero thicknesses that the model cannot deal with. Modeling the hydrodynamics of the Scheldt Estuary requires a specific treatment of these wetting and drying processes. But this is the subject of Chapter 3. However, modeling the hydrodynamics of the North Sea does not require such a treatment. Moreover, a shallow water model is well suited to model the tidal motion (Sinha and Pingree, 1997), which is the dominant feature in the North Sea (Otto et al., 1990). The model, as it is described at this stage, must therefore be able to reproduce satisfactorily the hydrodynamics of the North Sea.

From the mathematical point of view, the tidal signal is usually decomposed into the linear superposition of different harmonic components. In the North Sea, the semi-diurnal lunar M_2 component, whose period is 12 h 25 min, is largely predominant and is therefore a good approximation of the tidal motion (Otto et al., 1990). Tidal waves enter the North Sea from the North and through the Strait of Dover in the South. The southwards propagating wave travels as a Kelvin wave along the east coast of the United Kingdom and then turns anticlockwise along the Belgian, Dutch, German and Danish coasts, where it looses much of its energy. Only a small portion enters the Baltic Sea or leaves the region along the Norwegian coast (Maßmann et al., 2010). As an illustration, the co-tidal chart of the M_2 tide after Proudman and Doodson (1924) is given in Figure 2.5. The points from where the M_2 co-tidal lines seem to emanate are called amphidromic points. The M_2 tidal amplitude is nearly zero at these points, and the M_2 tidal waves circulate around them (Sinha and Pingree, 1997). Three M_2 amphidromic points are generally reported in the North Sea: one of the southern tip of Norway, one at 56°N, at the eastern tip of the Dogger Bank, and one near the entry of the Southern Bight. The Norwegian amphidromic point is not always reported, but then the course of the co-tidal lines form a virtual amphidromic point in the south of Norway (Otto et al., 1990).

The tidal motion of the North Sea is computed using SLIM, with the mesh presented on Figure 1.2, the implicit time-stepping scheme DIRK222 and a time step of 15 minutes. The bathymetry is based on

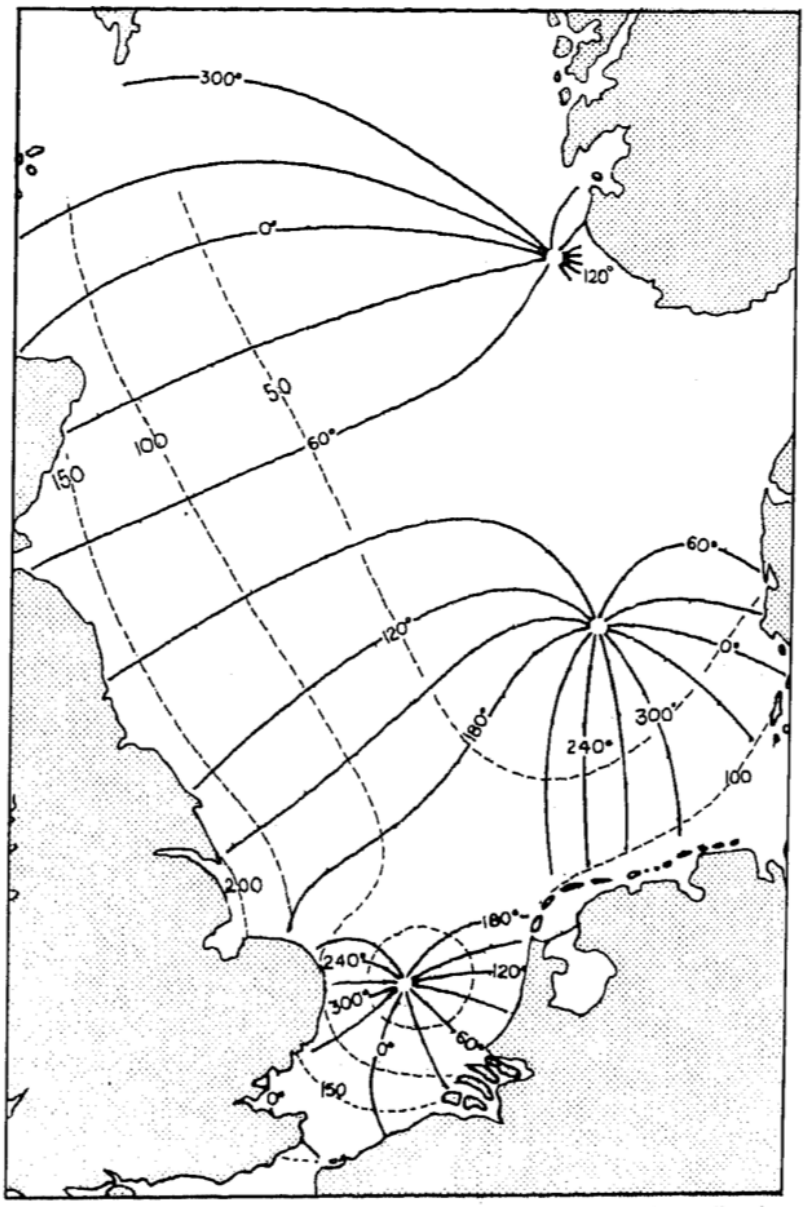

Figure 2.5: Co-tidal lines (phase in degrees) and co-range lines (amplitude in cm) of the M_2 tide in the North Sea, obtained from Otto et al. (1990) and originally published by Proudman and Doodson (1924).

ETOPO1 (Amante and Eakins, 2008). The eddy viscosity is parametrized using the Smagorinsky formulation (Smagorinsky, 1963; Majander and Siikonen, 2002):

$$\nu = c_\nu {d_e}^2 \sqrt{2\boldsymbol{d} : \boldsymbol{d}}, \tag{2.91}$$

where c_ν is a dimensionless coefficient set here to 0.01, d_e is the characteristic length of the element. The strain tensor $\boldsymbol{d}$ is here two-dimensional and defined as

$$\boldsymbol{d} = \frac{1}{2}\big((\boldsymbol{\nabla u}) + (\boldsymbol{\nabla u})^t\big). \tag{2.92}$$

As previously mentioned, the scalar product between two tensors is defined so that $\boldsymbol{A} : \boldsymbol{B} = \sum_i \sum_j A_{ij} B_{ji}$. The bottom stress is parameterized using the Chézy-Manning-Strickler formulation :

$$\boldsymbol{\tau}^{\mathrm{b}} = \rho g n^2 \frac{\|\boldsymbol{u}\|\boldsymbol{u}}{H^{1/3}}, \tag{2.93}$$

where the Manning coefficient n is set equal to $0.0235\,\mathrm{s\,m^{-1/3}}$, which is a typical value for sand (Graf and Altinakar, 1993; Heniche et al., 2000). The influence of the wind and the atmospheric pressure gradient are not taken into account in this simulation. The variations of the atmospheric conditions are operating at other frequencies, so that they do not enhance the M_2 tidal oscillations. The tide is forced at the shelf break using the elevation and velocity M_2 harmonics of the global tidal model TPXO7.1 (Egbert et al., 1994). River discharges are neglected so that all other boundaries are considered as coasts, where the slip coefficient λ is parameterized so that $\lambda/\nu = 10^{-3}\,\mathrm{m^{-1}}$. In order to avoid wetting and drying problems, the bathymetry is artificially cropped to a minimum of 10 m. The Scheldt Estuary is almost the only area affected by this constraint, but it is not the domain of interest in this chapter. The initial condition is zero for each variable. The simulation starts 5 days before the period of interest. It is the time needed to reach a regime solution.

The tidal chart presented in Figure 2.6, derived from the results of this simulation, compares rather well with the that proposed by Proudman and Doodson (1924). The three amphidromic points are present, and more or less located where expected. It is less the case for the Norwegian amphidromic point, but, once again, the latter is not reported in every study. Moreover the influence of the Baltic Sea is not taken into

account in this simulation, the south of the Kattegat being considered as a coast. This may result in a poorer behavior of the tidal motion in this area. However, the two other amphidromic points in the southern part of the North Sea are rather well represented. This is an important result. Since the M_2 component is predominant in the North Sea, it means that SLIM is well designed to model the tidal motion in the southern part of the North Sea. And since the tide is the main engine of the hydrodynamics in the Scheldt Estuary, it is of crucial importance for this work.

2.5 Conclusion

The objective of this chapter was to present the equations used in this doctoral dissertation to compute the hydrodynamics of geophysical flows and to specify the conditions under which they are valid. It has also been proved that a numerical model based on these equations is able to represent very satisfactorily the tidal motion in the North Sea.

However, as mentioned in the introduction, the model as it is presented in this chapter is not able to compute the hydrodynamics in the Scheldt Estuary. Indeed, because of its important tidal amplitude, the Scheldt Estuary experiences periodic emergence of large shallow areas at each tidal cycle. As the shallow water equations are intrinsically unable to deal with areas where the water thickness may become zero, a specific treatment of the wetting and drying processes has to be developed. This is the subject of the following chapter.

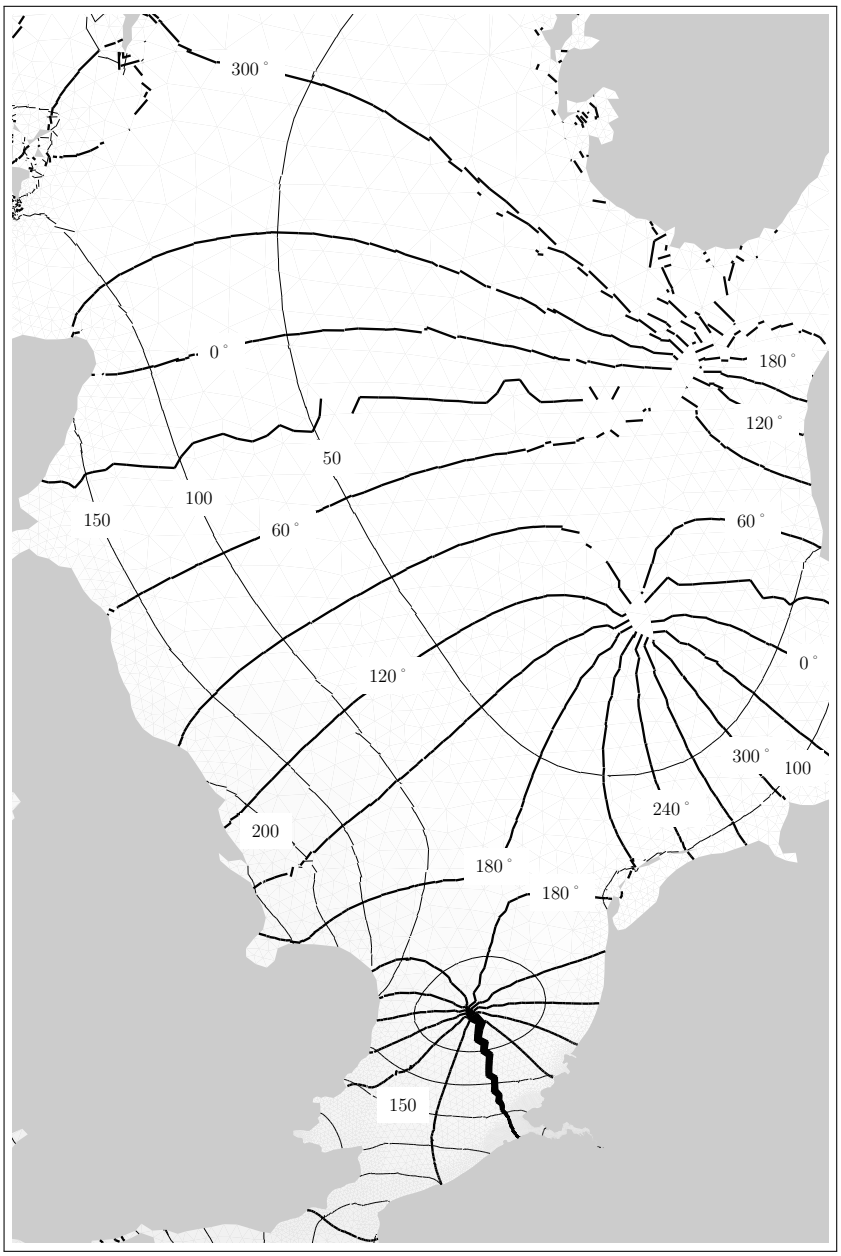

Figure 2.6: Co-tidal lines (thick lines, phase in degrees) and co-range lines (thin lines, amplitude in cm) of the M_2 tide in the North Sea, computed using SLIM.

Chapter 3

Wetting-drying

This chapter is based on the following publications:

Gourgue, O., Comblen, R., Lambrechts, J., Kärnä, T., Legat, V., and Deleersnijder, E. (2009). A flux-limiting wetting-drying method for finite-element shallow-water models, with application to the Scheldt Estuary. *Advances in Water Resources*, 32:1726-1739.

Kärnä, T., de Brye, B., **Gourgue, O.**, Lambrechts, J., Comblen, R., Legat, V., and Deleersnijder, E. (2011). A fully implicit wetting-drying method for DG-FEM shallow water models, with an application to the Scheldt Estuary. *Computer Methods in Applied Mechanics and Engineering*, 200:509–524.

3.1 Introduction

Most of the world's coastal seas are linked to embayments, estuaries and lagoons. A large number of these shallow-water bodies experience tidal oscillations of the free surface. Consequently, the extent of areas subject to alternating wetting and drying (the so-called tidal flats) can be as large as the permanently-submerged areas. The influence of the tidal flats is therefore of crucial importance, so that the wetting and drying processes need to be accurately simulated. Furthermore, tidal flats play a very important role in the dynamics of the ecosystem of these areas. The ability to represent the wetting and drying processes is therefore a key feature in coastal eco-hydrodynamic modeling. The estuarine part of the Scheldt downstream of Antwerp is characterized by

a complex morphology with deep flood and ebb channels surrounding several large tidal flats and sand banks, both of which are very shallow and are submerged during high water.

A major issue for the shallow water equations (2.59) and (2.60) in coastal modeling is the inability to model dry areas using classical eulerian numerical methods. Those methods are indeed not designed to deal with areas where the water height may become theoretically zero. The role of the wetting-drying methods is to allow the appearance and disappearance of dry areas. They are classified into two main categories: the deformed mesh (Lagrangian) methods and the fixed mesh (Eulerian) methods. Early studies show the potential of the deformed mesh strategy (Sielecki and Wurtele, 1970; Lynch and Gray, 1980), where the nodes on the boundary between wet and dry zones move following the front. But since the nodal coordinates vary at each time step, an important part of the model is devoted to the mesh adaptation, making this approach rather expensive. Consequently, at present, it is mostly restricted to idealized test cases (Christian and Palmer, 1997; Prasad and Svendsen, 2003), while the fixed mesh strategy is much widely used in realistic applications. The Eulerian methods are also divided into two main approaches: the flux-limiting methods and the so-called modified equation methods. With the flux-limiting strategy, only the discrete algebraic form of the hydrodynamic equations is modified. With the modified equation strategy, the original continuous form of the partial differential equations is modified.

The earliest flux-limiting method was suggested by Leendertse (1970) for a two-dimensional finite difference model. This type of approach turns off/on the mesh cells when the water thickness rises below/above a threshold value, limiting or canceling out the water fluxes on dry cells in order for the water depth to remain positive. However, an artificial slope of the free surface is formed in the dry areas because the water level is arbitrarily fixed at the bed elevation. This generates an extra pressure gradient term, which may lead to unstable behavior and has to be treated specifically. Nevertheless, this flux-limiting approach proves very popular in two-dimensional (Balzano, 1998) and three-dimensional (Lin and Falconer, 1997; Ji et al., 2001; Zheng et al., 2003; Oey, 2006; Abualtayef et al., 2008) finite difference models. Balzano's review is particularly extensive, gathering 10 different methods. The flux-limiting approach is also popular in finite volume modeling (Begnudelli and Sanders, 2007; Casulli, 2009; Wang et al., 2009). However, only a few examples exist with finite element models (Leclerc et al., 1990; Gourgue et al., 2009).

One of the methods among the modified equation approach is the porosity method (Heniche et al., 2000; Ertürk et al., 2002), in which the hydrodynamic equations are modified to allow water flow in a porous layer below the bed. The water depth can therefore be negative. This method avoids handling separately dry or wet cells, but allows unphysical water fluxes through dry zones. Therefore, the total mass of water within wet areas is not constant in time and conservation is then only ensured in a weak sense. Another objection to the porosity method is the lack of physical description of the so-called porous layer. It is no more the case with the capillary method that uses capillarity effect properties to describe wetting and drying processes (Tao et al., 2001; Jiang and Wai, 2005). Finally, with the damping or kinematic method, the processes like rotation and advection are neglected when the water column becomes very shallow such that a simple balance between external pressure gradient and friction prevails (Ip et al., 1998; Burchard et al., 2004; Ern et al., 2008). However, ensuring that the water depth remains positive by modifying the equations leads to spurious mass flux through dry areas. A rather different approach is developed by Kärnä et al. (2011a) in which the position of the sea bed is allowed to fluctuate in drying areas, without altering global and local mass conservation.

The selection of the suitable Eulerian method is difficult and in fact should depend on the flow under study. The problem to be tackled is highly nonlinear. Therefore, implicit time-stepping schemes are difficult to implement. The modified equation approach has a straightforward linearization that enables the use of implicit time-stepping. However it may lead to strong unphysical water fluxes, especially when using large time steps. Iterative solutions can be considered for both methods, but the convergence of such schemes requires the use of rather small time steps. If explicit methods are involved, the flux-limiting approach has the great advantage that the physics is not modified in the vicinity of dry areas. However, all flux-limiting methods are intrinsically nonlinear. As there are conditions to turn on/off a flux, these methods are discontinuous with respect to these variables. It is therefore not possible to deduce a stable linearization of the method as it is, and so implicit time stepping is not available directly.

In this chapter, two original methods are presented and verified against standard test cases. Section 3.2 describes an original method based on the flux-limiting strategy and that is designed for discontinuous finite elements and explicit time integration. Section 3.3 presents the modified bathymetry method that modifies the primitive equations

allowing the use of implicit time integration methods. The choice of the second method for long-term simulations is explained in Section 3.4, and the method is applied to compute the hydrodynamics of the Scheldt Estuary.

3.2 A flux-limiting explicit method

3.2.1 The method

This flux-limiting method is exclusively designed for finite element models using P_1^{DG} elements for the elevation field and explicit time-stepping (Gourgue et al., 2009). The first interesting property of the P_1^{DG} elements is their linear character that implies a monotonic shape of the elevation field on each element. The smallest value among the three nodes is the smallest value throughout the triangle. A triangle with three wet nodes is therefore wet everywhere. This is not the case with higher order elements. The second interesting property of the P_1^{DG} elements is their discontinuous character. They do not require any inter-element continuity, and information can only pass from an element to its neighbor through fluxes that can easily be turned on/off.

The method mainly deals with the continuity equation (2.59), which can be rewritten as follows:

$$\frac{\partial \eta}{\partial t} = \underbrace{-\boldsymbol{\nabla} \cdot \big((h+\eta)\boldsymbol{u}\big)}_{F\left(\eta, \boldsymbol{u}\right)}. \tag{3.1}$$

According to the nature of the equation, the operator F is conservative: its integral is zero over the whole domain Ω, if the latter is closed. For the sake of simplicity, the method is presented using the simple ERK1 time integration scheme (Section 2.3.2). However, it can be easily transposed to any other explicit scheme, by applying the method to each sub-time step. With such an time integration scheme, if there were no wetting and drying, equation (3.1) could be rewritten as follows:

$$\frac{\eta^{n+1} - \eta^n}{\Delta t} = F\big(\eta^n, \boldsymbol{u}^n\big). \tag{3.2}$$

This flux-limiting method is divided into three intermediate steps that are illustrated on Figure 3.1. To summarize, the elevation at time step n (η^n) is known before starting the wetting-drying method, and

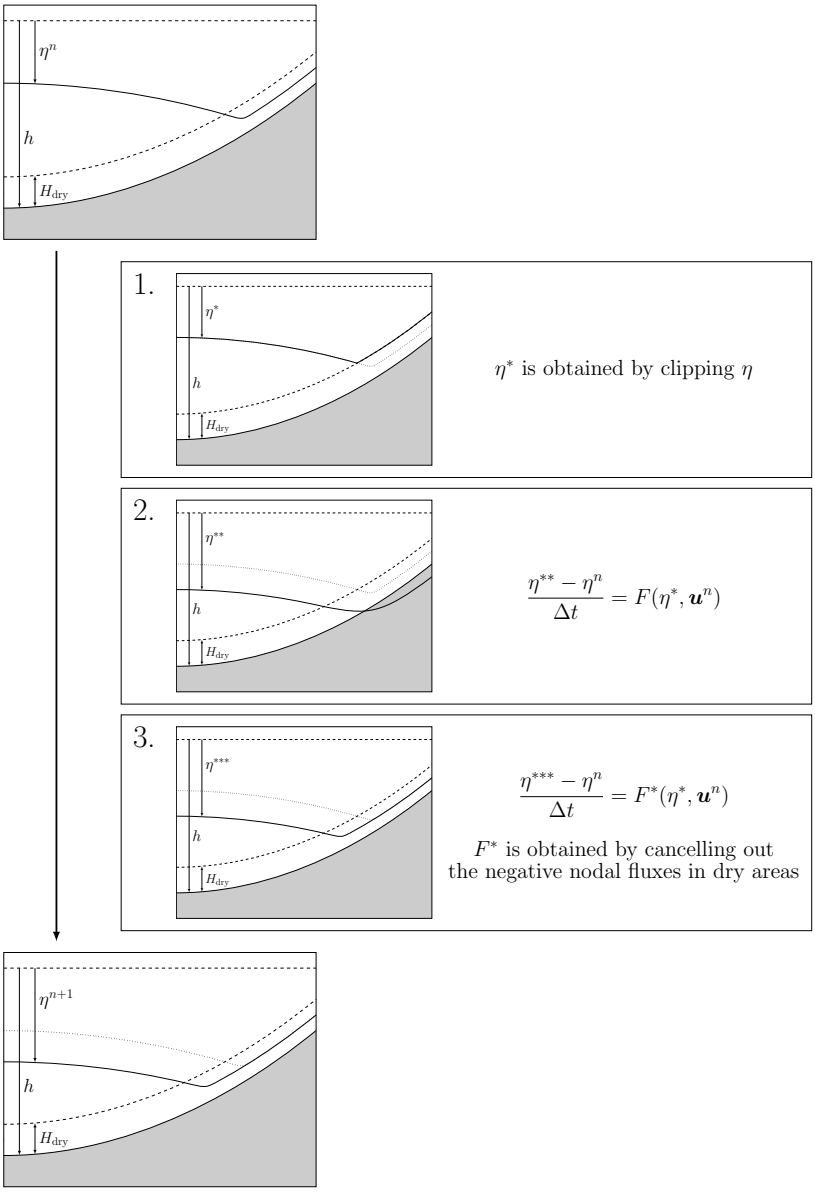

Figure 3.1: Illustration of the three steps of the flux-limiting method and the corresponding intermediate states of the elevation field η.

each step corresponds to an intermediate elevation (η^*, η^{**} and η^{***}), the last one being the elevation at time step $n+1$ (η^{n+1}).

1. The elevation is clipped to ensure that the water depth $h+\eta^*$ is not smaller than the threshold value H_{dry} at each position:

$$\eta^* = \max\big(\eta^n, H_{\text{dry}} - h\big). \tag{3.3}$$

2. The equation (3.2) is used with $\eta = \eta^*$ to ensure that only positive water depths are involved:

$$\frac{\eta^{**} - \eta^n}{\Delta t} = F\big(\eta^*, \boldsymbol{u}^n\big). \tag{3.4}$$

   Since the operator F is conservative, the mass is conserved between the second intermediate state ($**$) and the initial state (n). However, the free surface may have moved down in already dry areas.

3. The operator F is modified to ensure that the free surface does not move down in dry areas while remaining conservative:

$$\frac{\eta^{***} - \eta^n}{\Delta t} = F^*\big(\eta^*, \boldsymbol{u}^n\big). \tag{3.5}$$

   The third intermediate state represents accurately the water level around dry areas.

In practice, η^{**} and η^{***} are not computed. The second intermediate step only consists in building F, and the third one in modifying it into F^*. The elevation at time step $n+1$ is then computed as follows:

$$\frac{\eta^{n+1} - \eta^n}{\Delta t} = F^*\big(\eta^*, \boldsymbol{u}^n\big), \tag{3.6}$$

which is nothing but equation (3.2) with η and F modified in dry areas.

The way to obtain η^* from η^n in the first intermediate step is obvious. However, to describe how F is modified to obtain the operator F^* in the third intermediate step, the finite element Galerkin formulation of equation (3.4) is needed. Following the definitions accompanying equation (2.78), it can be written:

$$\Big[A_{ij}^{\eta}\Big] \cdot \frac{\Big[\eta_j^{**}\Big] - \Big[\eta_j^{n}\Big]}{\Delta t} = \Big[b_i^{\eta\text{s}}\Big] + \Big[b_i^{\eta\text{c}}\Big], \tag{3.7}$$

where the vectors $\left[\eta_j^{**}\right]$ and $\left[\eta_j^{n}\right]$ gather the $3N_e$ nodal values of η^{**} and η^n, respectively. Multiplying the latter equation by $\left[A_{ij}^{\eta}\right]^{-1}$, the inverse matrix of $\left[A_{ij}^{\eta}\right]$, it becomes:

$$\frac{\left[\eta_j^{**}\right] - \left[\eta_j^{n}\right]}{\Delta t} = \underbrace{\left[A_{ij}^{\eta}\right]^{-1} \cdot \left[b_i^{\eta \mathrm{s}}\right]}_{\left[F_j^{\eta \mathrm{s}}\right]} + \underbrace{\left[A_{ij}^{\eta}\right]^{-1} \cdot \left[b_i^{\eta \mathrm{c}}\right]}_{\left[F_j^{\eta \mathrm{c}}\right]}, \tag{3.8}$$

where $\left[F_j^{\eta \mathrm{c}}\right]$ and $\left[F_j^{\eta \mathrm{c}}\right]$ are called the generalized nodal fluxes due to surface and contour integrals, respectively.

Negative nodal fluxes tend to lower the water surface, which must be avoided on dry nodes. On the other hand, positive nodal fluxes tend to elevate the water surface, which allows to flood dry areas. Therefore, in the third step, the generalized nodal fluxes are modified by canceling out those that are negative in dry areas:

$$\frac{\left[\eta_j^{**}\right] - \left[\eta_j^{n}\right]}{\Delta t} = \left[F_j^{\eta \mathrm{s}*}\right] + \left[F_j^{\eta \mathrm{c}*}\right], \tag{3.9}$$

where

$$F_j^{\eta \mathrm{s}*} = \begin{cases} 0 & \text{if there is a node } i \in \Omega_{e(j)} \\ & \quad \text{with} \quad F_i^{\eta \mathrm{s}} < 0 \quad \& \quad \eta_i^n + h_i < H_{\mathrm{dry}} \\ F_j^{\eta \mathrm{s}} & \text{otherwise,} \end{cases} \tag{3.10}$$

$$F_j^{\eta \mathrm{c}*} = \begin{cases} 0 & \text{if} \quad F_j^{\eta \mathrm{c}} < 0 \quad \& \quad \eta_j^n + h_j < H_{\mathrm{dry}} \\ F_j^{\eta \mathrm{c}} & \text{otherwise,} \end{cases} \tag{3.11}$$

where $\Omega_{e(j)}$ is the element where the shape function ϕ_j is not zero everywhere, and h_i is the value of the bathymetry h at node i. It is for mass conservation reasons that all nodal fluxes due to surface integrals are cancelled out if at least one is negative on a dry node. The modification of the nodal fluxes in the third intermediate step are illustrated by Figure 3.2.

The mass conserving property of the second step is not altered in the third step since only fluxes are cancelled out. Clearly, the algorithm as a whole preserves mass. Moreover, all discontinuous Galerkin methods are intrinsically locally mass conservative, as a flux balance can be made for each element. Since the only effect of the present wetting-drying is to cancel out some fluxes in dry areas, the method is also locally mass conservative.

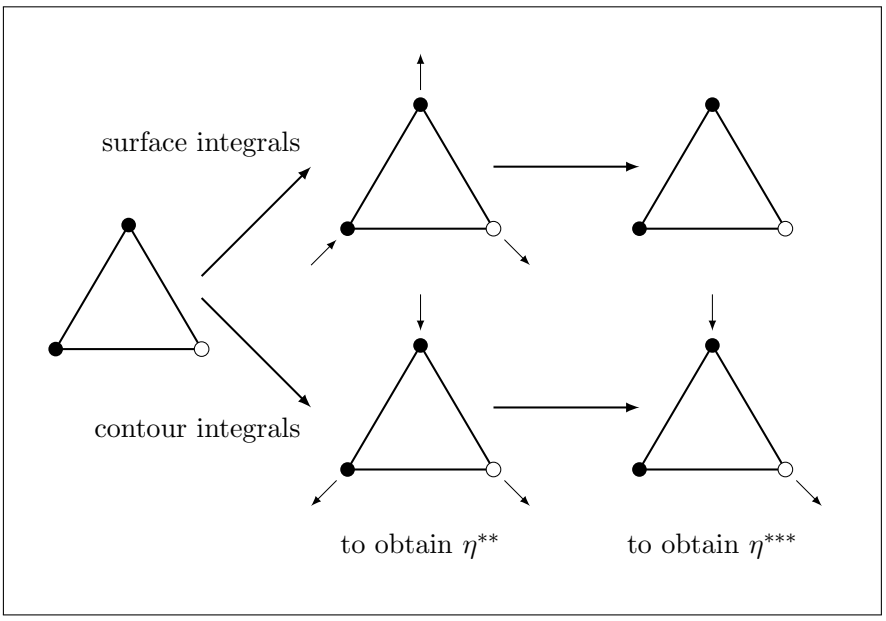

Figure 3.2: Illustration of the third intermediate step of the flux-limiting wetting-drying method; black and white nodes are dry and wet nodes, respectively, at time step n; inward and outward small arrows represent postive and negative nodal fluxes, respectively.

There are also a few modifications in the momentum conservation equation (2.60). First of all, the clipped elevation η^* is used to ensure that only positive water depths are dealt with, thus avoiding dividing by zero in some terms. Moreover, for stability reasons, the gravity effect cancelled out within the dry elements to allow the free surface to remain parallel to the bottom (Leclerc et al., 1990). Finally, in shallow areas, the bottom stress and the eddy viscosity are increased, and the surface stress is decreased. This is done using the concept of a "buffer" layer (Ip et al., 1998; Heniche et al., 2000; Zheng et al., 2003; Wang et al., 2009), the thickness of which is H_{buf}. The terms to increase or decrease are multiplied by a factor linearly varying from 1 when $H \geq H_{\text{buf}}$ to f_{buf} when $H \leq H_{\text{dry}}$. Different values of the factor f_{buf} are chosen for each term. Inside an element with at least one dry node, the above-mentioned terms are multiplied by f_{buf}, whatever the value of H.

If there were no wetting-drying to deal with, η^{n+1} would simply be computed using the equation (3.2), which is just the equation (3.5) with $\eta^* = \eta^n$ and $F^* = F$, i.e. with no modification of η^n and F during the first and third intermediate steps, respectively. The extra computing cost of this flux-limiting method is therefore due to these two intermediate steps, which only consist in modifying some nodal values and some nodal fluxes in dry areas, which is rather cheap. Moreover, it does not require additional stability constraint, except the conventional CFL stability condition (2.87) of explicit time integration methods.

3.2.2 Verification of the method

Balzano (1998) presented three simple one-dimensional test cases to compare different flux-limiting wetting-drying methods for finite difference models. They were also used to evaluate the accuracy of other wetting-drying methods (Yuan et al., 2008). The computational domain of the three test cases is a one-dimensional basin 13,800 m in length. However, as the goal is to verify a wetting-drying method for two-dimensional models, this one-dimensional domain is replaced by a two-dimensional one. This new domain has a relatively large width of 7,200 m and frictionless coastlines. The two-dimensional problems and their corresponding one-dimensional Balzano test cases must have the same solutions.

The reference water level is 5 m at the open boundary and zero at the other end, where the basin is closed. The Coriolis force, the surface stress and the horizontal viscosity are neglected. The bottom stress is parameterized with the Chézy-Manning-Strickler formulation (2.93) with the Manning coefficient n equal to $0.02\,\mathrm{s\,m^{-1/3}}$, which is a typical value for sand (Graf and Altinakar, 1993; Heniche et al., 2000). A specific mesh is designed for each test case. They are displayed beside the corresponding results. The ERK2 time integration scheme (Section 2.3.2) is used to integrate in time and the time step is dynamically adapted to satisfy the CFL condition (2.87) everywhere. Finally, concerning the wetting-drying method itself, the threshold thickness H_{dry} is fixed to 0.01 m, and because of the relatively low basin slopes for each test case, no modification of terms has to be done in the buffer layer ($f_{\mathrm{buf}} = 1$). The only differences between the three test cases are their bathymetry and external forcing.

In the first Balzano test case (Figure 3.3), a basin with a uniform bottom slope is considered. The analytical expression of the bathymetry

may be found in Appendix A. At the open boundary, a sinusoidal water level variation is imposed, with a period of 12 h and an amplitude of 2 m, the water depth at the open boundary oscillating between 3 and 7 m. Following the observations of Balzano (1998), some methods cause undesired wiggles in the free surface profile during the wetting phase. It is clearly not the case here. In dry areas (where the water thickness is theoretically zero), some methods also suffer from pronounced underestimation (strictly negative water thickness) or overestimation (strictly positive water thickness) of the retention volume. With the present method, the water thickness is always positive. So the retention volume is never underestimated. Moreover, the water thickness in dry areas is controlled by the threshold value H_{dry}, which limits the overestimation to very small values.

In the second Balzano test case (Figure 3.4), the external forcing is the same, but the bathymetry is different. While the first basin has a uniform slope, the second one contains a small shelf. The analytical expression of the bathymetry may be found in Appendix A. The mesh is designed to represent it exactly. In addition to the wiggling and retention problems mentioned before, Balzano (1998) notices a runoff problem with some methods in this test case. With these methods, the runoff becomes negligible along the shelf at the end of the drying phase, with an important overestimation of the retention volume. And during the wetting phase, a period of newly increasing runoff is observed. This two phase runoff behavior is clearly not plausible. With the present method, the slowing down of the runoff seems quite linear, which is the correct physical behavior.

In the third Balzano test case (Figure 3.5), the basin contains a small reservoir. The analytical expression of the bathymetry may be found in Appendix A. The external forcing is also different. The elevation of the water is initially set to 2 m, i.e. the water depth is 7 m at the open boundary and 2 m at the other end. A sinusoidal decay is then applied during 6 h (half the sinusoidal period) at the open boundary to decrease the water depth from 7 to 3 m. Afterwards, the water level at the open boundary is kept to 3 m, and the simulation ends after 100 h. Clearly, the surface in the reservoir should asymptotically reach an horizontal plane at the level of the local peak of the bathymetry. The mesh is designed to represent exactly both the analytical bathymetry and the expected elevation in the reservoir. Among the three Balzano test cases, the third one is probably the most difficult to tackle. For example, with most of the modified equation methods, the water surface behavior is

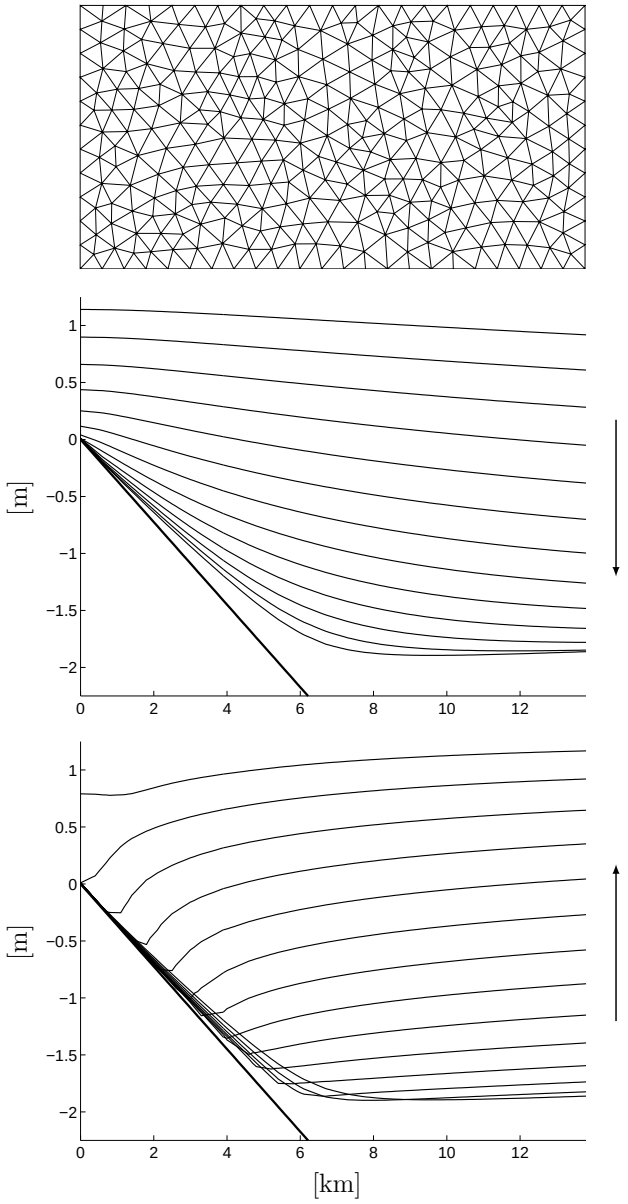

Figure 3.3: [First Balzano test case] Mesh used (561 triangles with a characteristic length of 600 m), and vertical section, along the main direction of the domain, showing the sea bed (thick line) and the elevation of the water surface η every 20 minutes (thin lines), during the drying and wetting phases.

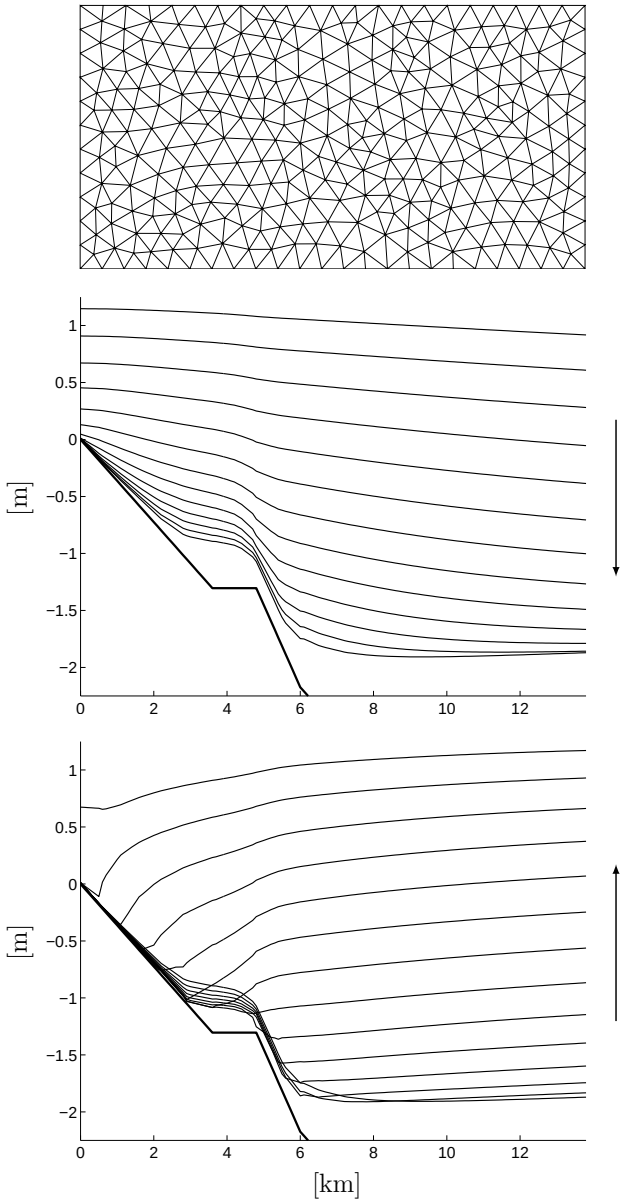

Figure 3.4: [Second Balzano test case] Mesh used (557 triangles with a characteristic length of 600 m), and vertical section, along the main direction of the domain, showing the sea bed (thick line) and the elevation of the water surface η every 20 minutes (thin lines), during the drying and wetting phases.

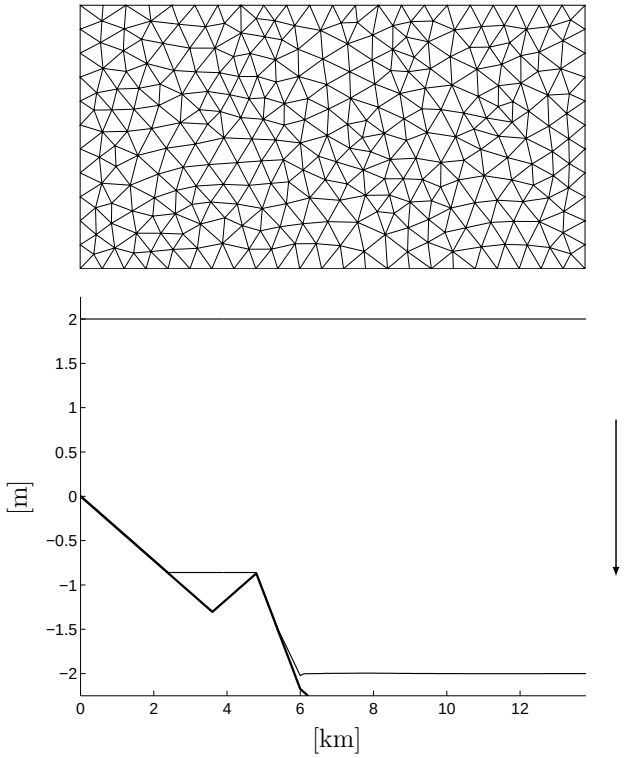

Figure 3.5: [Third Balzano test case] Mesh used (543 triangles with a characteristic length of 600 m), and vertical section, along the main direction of the domain, showing the sea bed (thick line) and the elevation of the water surface η at initial time and at equilibrium (thin lines).

badly represented: some water can flow from the reservoir to the rest of the basin, even when the mean surface level inside the reservoir is below the local peak of the bathymetry. With this flux-limiting method, after 100 h of simulation, the expected water level is perfectly simulated in the reservoir. Therefore, the physics does not seem to be altered close to dry areas.

The bottom slopes of these academical test cases are very low compared with those along the main channels of the Scheldt Estuary. Nev-

ertheless, simulations in similar basins but with steeper slopes have also been performed with the present flux-limiting method, and the quality of the results have not been altered. However, because the configuration defined by Balzano is considered as a reference, the results are presented in the same framework.

The first Balzano test case is also used to verify the convergence of the method, by evaluating the L^2 error on the elevation after one tidal cycle (Figure 3.6). The meshes used for this convergence analysis are similar to that of Figure 3.3, with various triangle characteristic lengths, the reference solution being computed on a mesh whose triangle characteristic length is 150 m. A time step of 1 s is used for all runs. The convergence rate is estimated to 1.7, while it should be theoretically 2 with the $P_1^{\mathrm{DG}} - P_1^{\mathrm{DG}}$ pair and without wetting and drying (Comblen et al., 2010b). Actually, the same analysis has been performed for all the test cases: convergence is always observed, and each time at a rate comprised between 1 and 2, the extent of the dry areas decreasing the convergence rate towards 1, suggesting that the present wetting-drying method is first order.

Finally, the Thacker test case (Thacker, 1981) is used to illustrate that the method is strictly mass conserving. For this test case, the domain is a circular closed basin, so that no water can enter or leave the domain; the sea bed is a paraboloid of revolution. At the initial time, the free surface is also a paraboloid of revolution. Then, the free surface moves with free oscillations and wetting and drying occurs on the boundary of the domain (Figure 3.7). If there is no Coriolis force, no surface stress and no dissipation (neither viscosity nor bottom stress), the analytical solution of the problem is known (Thacker, 1981). The analytical expressions of the bathymetry and the solution of the non dissipative problem may be found in Appendix A.

However, this flux-limiting method requires some dissipation to be stable, and the bottom stress is taken into account using the Chézy-Manning-Strickler formulation (2.93). The values of the wetting-drying parameters are the same as in the Balzano test cases ($H_{\mathrm{dry}} = 0.01\,\mathrm{m}$ and $f_{\mathrm{buf}} = 1$). Several simulations are conducted on the mesh presented in Figure 3.7, using various values of the Manning coefficient n. The time integration scheme used is the same as in the Balzano test cases. The evolution of the free surface in the center of the domain is shown in Figure 3.8. It is clearly seen that, as expected, the model results tend to the Thacker solution when decreasing the Manning coefficient.

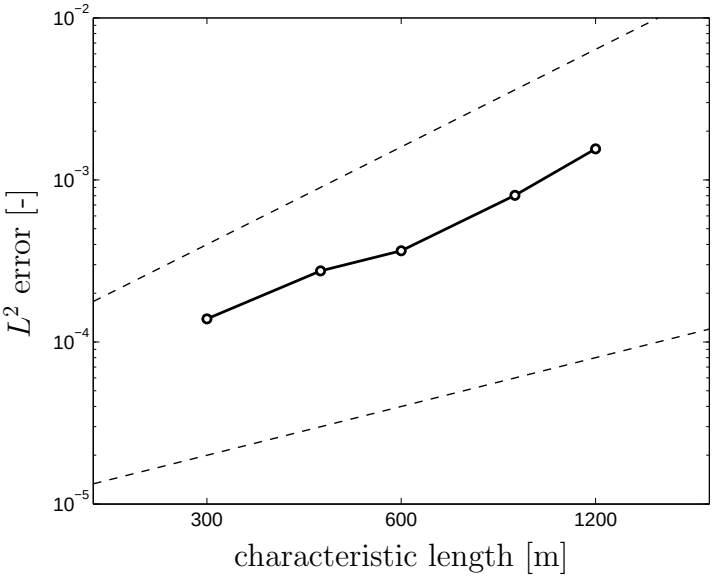

Figure 3.6: [First Balzano test case] Evolution of the L^2 error on the elevation of the water surface η after 12 h, versus the characteristic length of the triangle meshes; the reference solution is computed on a mesh whose triangle characteristic length is 150 m; the rate of the dashed lines are 1 (below) and 2 (above), while the convergence rate is here estimated to 1.7.

Since the method is mass conserving and the domain is closed (and since the flow is incompressible), the total water volume must always remain constant. After four free oscillation cycles, the maximum relative difference between the water volume and its initial value is of the order of 10^{-15}, for each simulation. The volume is therefore strictly conserved, up to round-off errors.

3.3 The modified bathymetry implicit method

3.3.1 The method

This second wetting-drying method is more versatile, as the wetting and drying phenomena are taken into account in the primitive equations

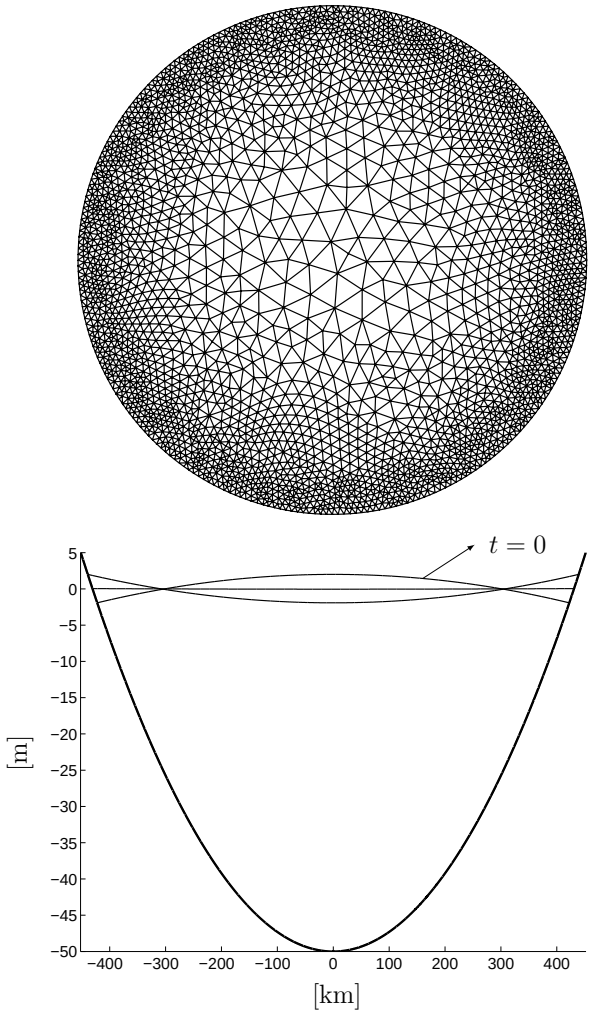

Figure 3.7: [Thacker test case] Mesh used (6012 triangles with a characteristic ranging from 10 km near the border to 50 km near the center), and vertical section, along the diameter of the circular domain, showing the sea bed (thick line) and the theoretical elevation of the water surface η when there is no dissipation, at initial time, after 3 hours and after 6 hours (thin lines).

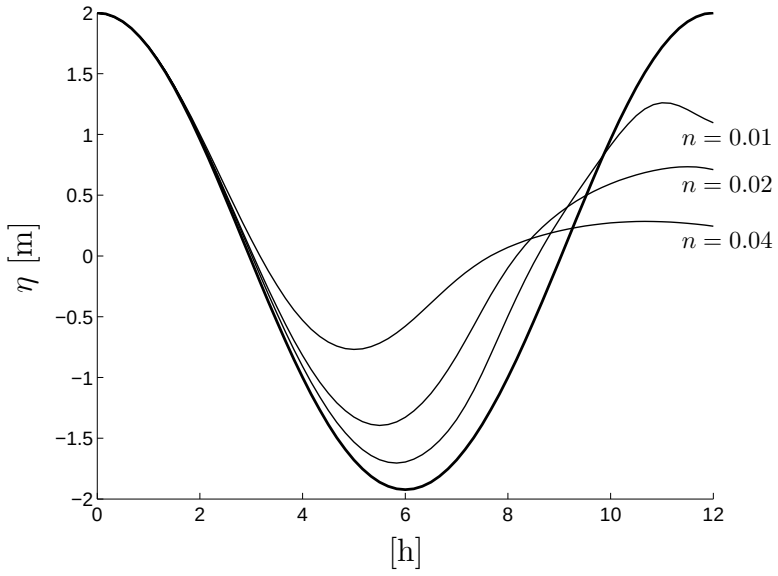

Figure 3.8: [Thacker test case] Evolution of the free surface in the center of the domain for different values of the Manning coefficient; the thin lines ($n > 0$) are model results, and the thick line ($n = 0$) is the exact Thacker solution, assuming zero dissipation.

themselves, by modifying equations (2.59) and (2.60). It is therefore independent of the choice of discretization, and is especially valid for implicit time integration (Kärnä et al., 2011a).

To ensure positive water depths, a smooth function $s(H)$ is introduced to redefine the bathymetry as

$$\tilde{h} = h + s(H), \tag{3.12}$$

so that the redefined water depth $\tilde{H} = \eta + \tilde{h}$ remains positive (Figure 3.9). Then, the primitive continuity equation (2.59) is modified in such a way that the bed fluctuation is properly taken into account:

$$\frac{\partial \eta}{\partial t} + \frac{\partial \tilde{h}}{\partial t} + \boldsymbol{\nabla} \cdot \left(\tilde{H} \boldsymbol{u} \right) = 0, \tag{3.13}$$

where the second term is due to the fact that $\tilde{h}$ is not static. The variable that is conserved is therefore now the redefined water depth $\tilde{H}$. It is

important to remark that, if the first two terms are developed further:

$$\begin{aligned}\frac{\partial \eta}{\partial t}+\frac{\partial \tilde{h}}{\partial t} &= \frac{\partial \eta}{\partial t}+\frac{\partial \tilde{h}}{\partial H}\frac{\partial H}{\partial t}\\ &= \left(1+\frac{\partial \tilde{h}}{\partial H}\right)\frac{\partial \eta}{\partial t}\\ &= \left(1+\frac{\partial s}{\partial H}\right)\frac{\partial \eta}{\partial t}\\ &= \big(1+s'(H)\big)\frac{\partial \eta}{\partial t}\\ &\triangleq A(H)\,\frac{\partial \eta}{\partial t}. \end{aligned} \tag{3.14}$$

Introducing equation (3.14) into the continuity equation (3.13) leads to a formulation closely related to the scaling of the continuity equation that is presented in some porosity methods (Ip et al., 1998; Heniche et al., 2000; Jiang and Wai, 2005). Indeed, it is easy to see that $0 < A < 1$ so that A is a smooth indicator that ranges from dry ($A \approx 0$) to wet ($A \approx 1$) conditions. In the context of the porosity method, A is interpreted as the wet fraction of an element that is penetrable by water. In contrast with flux-limiting methods where elements are either wet or dry, it is exactly the smoothness of A that prevents spurious oscillations and allows implicit time stepping.

The primitive momentum conservation equation (2.60) is only modified by replacing H by $\tilde{H}$, which only appears in the forcing and dissipative terms:

$$\begin{aligned}&\frac{\partial \boldsymbol{u}}{\partial t}+\boldsymbol{u}\cdot(\boldsymbol{\nabla}\boldsymbol{u})+f\boldsymbol{e}_z\times\boldsymbol{u}\\ &\qquad = -g\boldsymbol{\nabla}\eta+\frac{1}{\tilde{H}}\boldsymbol{\nabla}\cdot\big(\tilde{H}\nu\boldsymbol{\nabla}\boldsymbol{u}\big)+\frac{\boldsymbol{\tau}^{\mathrm{s}}-\boldsymbol{\tau}^{\mathrm{b}}}{\rho\tilde{H}}. \end{aligned} \tag{3.15}$$

The discrete form of equations (3.13) and (3.15) is very similar to that of the original equations. The system of equations to solve can also be synthesized by the matrix equation (2.78). Comparing with the system from the original equations, the only differences are found in the integrals contained in the vector $\boldsymbol{b}$. First of all, the integrals from the additional term of equation (3.13) are added and the integrals from the diffusive term and the surface and bottom stress terms of equation (3.15) are modified according to the redefined water depth $\tilde{H}$. Secondly,

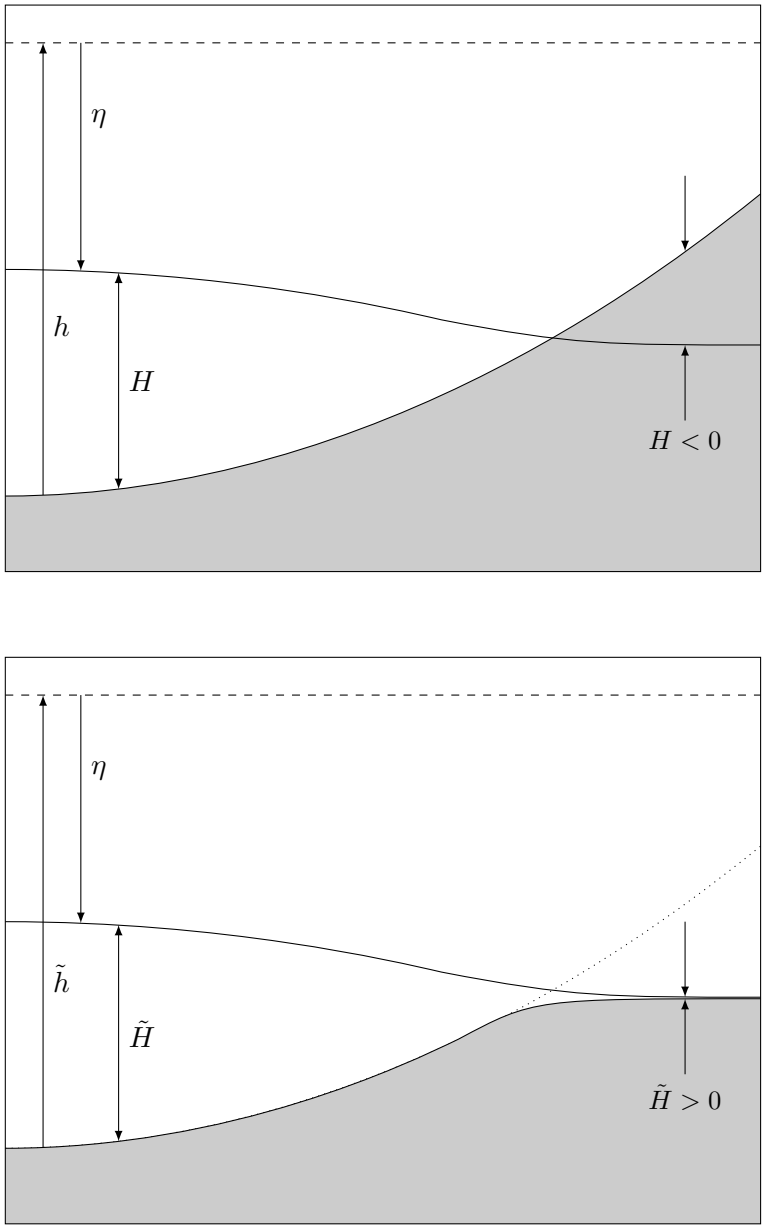

Figure 3.9: Vertical cut illustrating the classical variables for a fixed bathymetry (above) and the redefined variables of the modified bathymetry method (below).

the Riemann solver used to determine the value of η^h and $\boldsymbol{u}^h$ on the contour integrals must be adapted to take into account the redefinition of the bathymetry $\tilde{h}$ and the water depth $\tilde{H}$.

The choice of the function $s(H)$ must be done taking care to meet the following properties:

1. $\tilde{H} = H + s(H) > 0$ for all H,
2. $s(H) \approx 0$ for $H \gg 1$,
3. $s(H)$ must be continuously differentiable.

The first property is obvious since the purpose of the method is to ensure positive water depths. The second property states that the modification is restricted to shallow areas only. And the third property is needed for ensuring convergence of Newton iterations when using implicit time stepping (Kärnä et al., 2011a). The following function fulfills the desired properties:

$$s(H) = \frac{1}{2}\Big(\sqrt{H^2 - \alpha^2} - H\Big), \tag{3.16}$$

where α is a free parameter controlling the smoothness of the transition. It is important to note that the choice of such a non-polynomial function $s(H)$ requires a linear spatial discretization for η to ensure mass conservation (Kärnä et al., 2011a). It is the case here as this study is restricted to P_1^{DG} elements for both the elevation and the velocity fields.

In practice, the parameter α affects the width of the transition zone between wet ($A(H) \approx 1$) and dry ($A(H) \approx 0$) areas (the smaller α, the smaller the transition zone). Moreover, since $\tilde{H} = \alpha/2$ when $H = 0$, it directly controls the remaining water depth in dry areas, and may be compared to the threshold depth parameter H_{dry} of the flux-limiting method. For robust operation, the wetting-drying interface should be smooth so that the transition zone should encompass more than one element. Estimating the variation in bathymetry within one element by

$$\epsilon = d_e \|\boldsymbol{\nabla} h\|, \tag{3.17}$$

where d_e is a typical length scale of the triangle Ω_e, a rule of thumb for gradually sloping domains could be $\alpha \approx \epsilon$. Other more restrictive constraints may also exist for numerical stability reasons. For example, it is plausible that rapidly varying flows and shock waves require larger values for α. These restrictions are, however, more difficult to estimate a priori.

3.3.2 Verification of the method

The Balzano (Balzano, 1998) et Thacker (Thacker, 1981) test cases are also of use to verify the accuracy of the modified bathymetry method. The physical setups and the meshes are the same as in Section 3.2.2. As one of the major assets of the modified bathymetry method is its ability to operate with implicit time stepping, the test cases are here simulated using the DIRK222 time integration scheme (Section 2.3.2), with a time step of 10 minutes. Concerning the wetting-drying method itself, according to equation (3.17) and the rule of thumb of the former section ($\alpha \approx \epsilon$), a value of 0.3 m is assigned to the parameter α for the Balzano test cases and a value of 2 m for the Thacker test case.

To facilitate the comparison with the results obtained with the flux-limiting method, it is useful to plot the total water column depth on the original static bathymetry. In this case, the elevation is given by

$$\tilde{\eta} = \tilde{H} - h = \eta + s, \tag{3.18}$$

and is called the redefined elevation.

In the first two Balzano test cases (Figure 3.10 and 3.11), the results are in good agreement with those obtained using the flux-limiting method: no wiggle during the wetting phase, a small retention volume and a correct behavior of the runoff. The only noticeable difference is that the shocks at the flooding front appear to be milder than with the flux-limiting method, which is due to the smooth wetting-drying transition.

In the third Balzano test case (Figure 3.12), where the basin contains a small reservoir, the results are not so good. Because the water fluxes do not vanish as long as the pressure gradient term operates, the reservoir eventually dries up. The flux depends on the parameter α (the smaller α, the smaller the flux) and the bottom friction parameterization (the bigger the bottom friction, the smaller the flux), but neither can prevent the reservoir from drying as time goes to infinity. The third Balzano test case reveals therefore that water is leaking through dry areas, which can be seen as a major drawback of the present method. However, it must be stressed that such a drawback is common to all porous media methods (Nielsen and Apelt, 2003; Kärnä et al., 2011a). This is also probably the price to pay to be able to use implicit time integration methods.

As in Section 3.2.2, the first Balzano test case is also used to verify the convergence of the method, by evaluating the L^2 error on the elevation after one tidal cycle (Figure 3.13). The meshes used for this

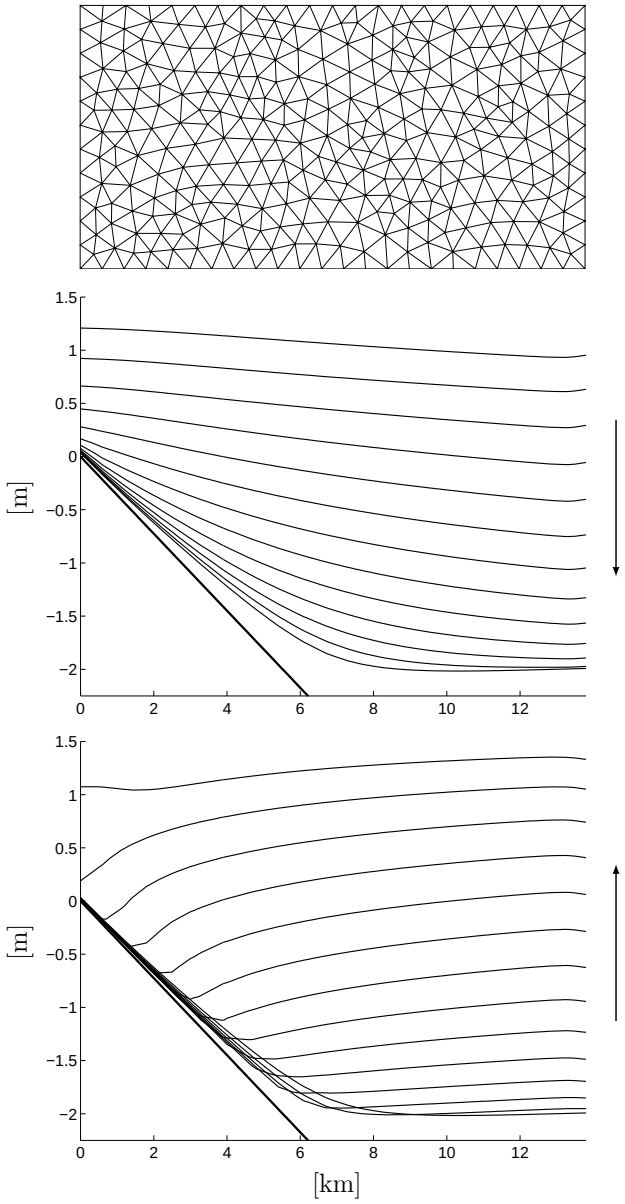

Figure 3.10: [First Balzano test case] Mesh used (561 triangles with a characteristic length of 600 m), and vertical section, along the main direction of the domain, showing the sea bed (thick line) and the redefined elevation of the water surface $\tilde{\eta}$ every 20 minutes (thin lines), during the drying and wetting phases.

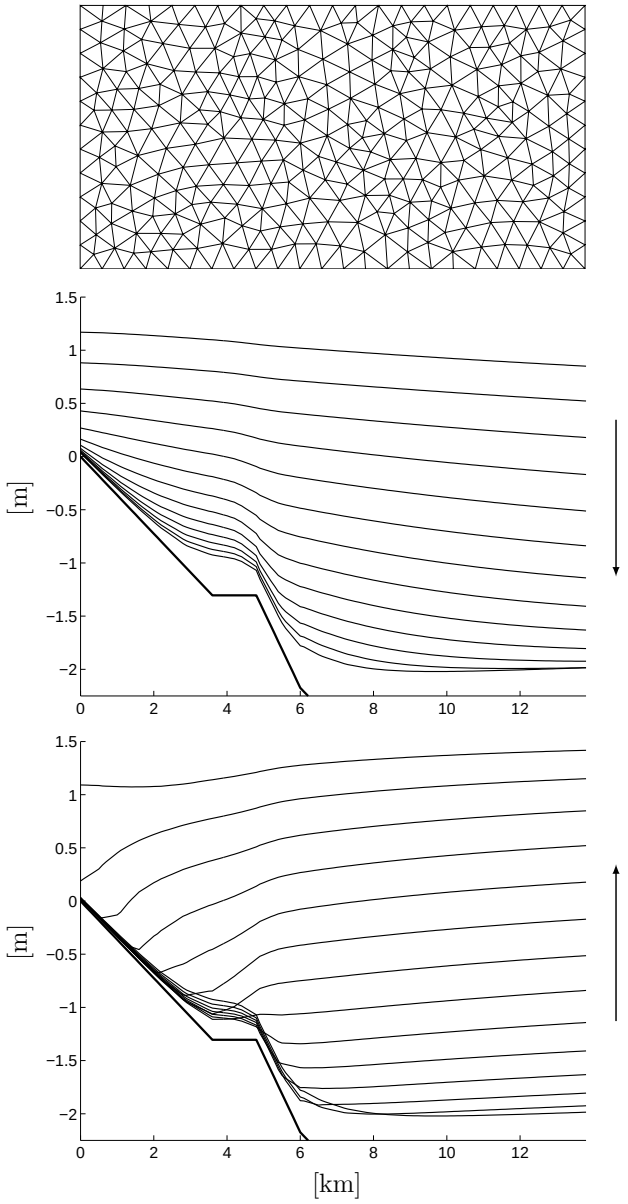

Figure 3.11: [Second Balzano test case] Mesh used (557 triangles with a characteristic length of 600 m), and vertical section, along the main direction of the domain, showing the sea bed (thick line) and the redefined elevation of the water surface $\tilde{\eta}$ every 20 minutes (thin lines), during the drying and wetting phases.

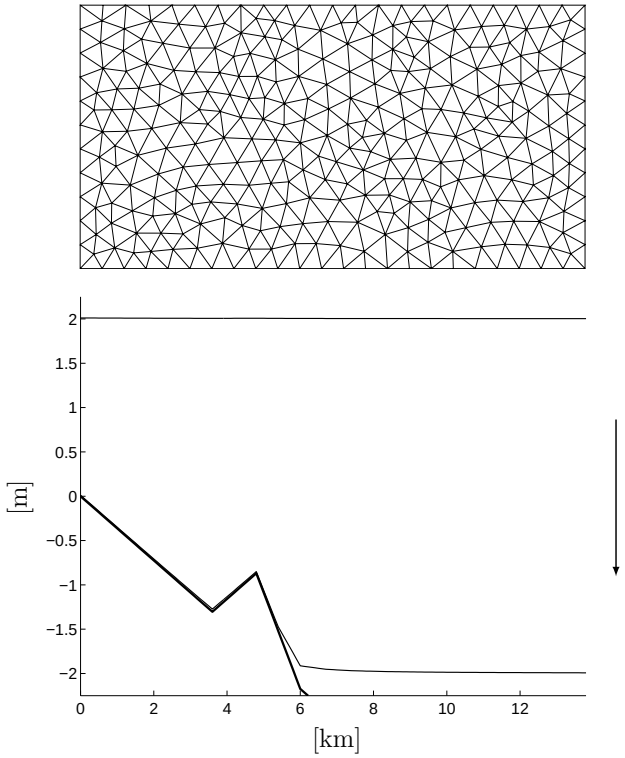

Figure 3.12: [Third Balzano test case] Mesh used (543 triangles with a characteristic length of 600 m), and vertical section, along the main direction of the domain, showing the sea bed (thick line) and the redefined elevation of the water surface $\tilde{\eta}$ at initial time and at equilibrium (thin lines).

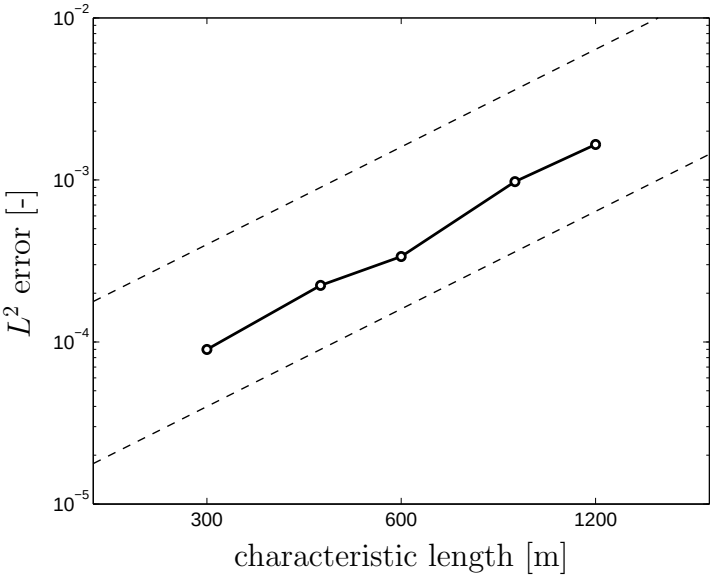

Figure 3.13: [First Balzano test case] Evolution of the L^2 error on the elevation of the water surface η after 12 h, versus the characteristic length of the triangle meshes; the reference solution is computed on a mesh whose triangle characteristic length is 150 m; the rate of the dashed lines are 1 (below) and 2 (above), while the convergence rate is here estimated to 2.1.

convergence analysis are similar to that of Figure 3.10, with various triangle characteristic lengths, the reference solution being computed on a mesh whose triangle characteristic length is 150 m. A time step of 30 s is used for all runs. The convergence rate is here estimated to 2.1, while it should be theoretically 2 with the $P_1^{\mathrm{DG}} - P_1^{\mathrm{DG}}$ pair, and without wetting and drying (Comblen et al., 2010b), suggesting that the convergence rate of the discretization method is not affected by the wetting-drying strategy. This is not surprising since the present modified bathymetry method takes the wetting and drying phenomena into account from the primitive equations, and therefore before their discretization.

The results of the Thacker test case are very similar to those obtained with the flux-limiting methods. Firstly, the evolution of the free surface in the center of the domain (Figure 3.14) tends towards the Thacker

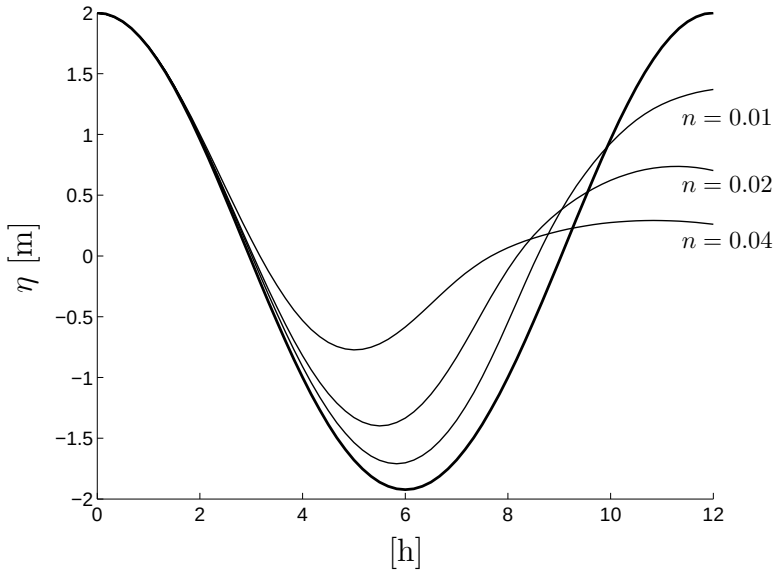

Figure 3.14: [Thacker test case] Evolution of the free surface in the center of the domain for different values of the Manning coefficient; the thin lines ($n > 0$) are model results, and the thick line ($n = 0$) is the exact Thacker solution, assuming zero dissipation.

analytical solution when decreasing the Manning coefficient n, which is the expected behavior. Secondly, after four oscillation cycles, the maximum relative difference between the water volume and its initial value is of the order of 10^{-15}. The total water volume is therefore also strictly conserved with the modified bathymetry method, up to round-off errors.

3.4 Modeling the hydrodynamics of the Scheldt Estuary

At this stage, the model is finally equipped to reproduce the tidal motion inside the Scheldt Estuary. To deal with the wetting and drying phenomena, it is now necessary to make a choice between both methods presented above. Comparing the results for the different test cases, especially those for the third Balzano test case, and regardless of the time integration method, the choice should naturally stand on the flux-limiting method. However, it requires an explicit time integration method and therefore to satisfy the CFL constraint (2.87) on the time step. Small elements of meshes similar to that presented on Figure 1.2 lead to very small time steps (less than 1 s), making the computing time rather long. Nevertheless, Gourgue et al. (2009) performed a 2 week simulation on a coarser mesh to prove that the flux-limiting method is also working on real applications.

But the goal is to build a model able to perform environmental studies, with simulations over several months or years. Therefore, using an explicit time integration method would lead to an unacceptably long computing time, at least with the current version of SLIM. Therefore, at the time of writing this doctoral dissertation, the only admissible solution was the modified bathymetry method, enabling the use of implicit time integration methods, and therefore without any numerical restriction on the time step. However, the recent developments to optimize the computing cost of the next version of SLIM, as the interest for explicit time integration methods when considering large parallel computing, allow to think about the flux-limiting method as a future admissible solution too.

The setup to simulate the hydrodynamics of the Scheldt Estuary is therefore similar to that for the tidal motion in the North Sea (Section 2.4). The mesh is that shown in Figure 1.2. The DIRK222 implicit time integration scheme (Section 2.3.2) is used with a time step of 15 minutes. The bathymetry is based on ETOPO1 (Amante and Eakins, 2008) in the European shelf and on data from the KustZuid model[1] in the Scheldt Estuary. The wetting and drying processes are dealt with the modified bathymetry method, with the smoothing parameter $\alpha = 0.5\,\mathrm{m}$. Upstream of Antwerp, a one-dimensional section-averaged model is used.

[1]Courtesy of M. Zijlema from the National Institute for Coastal and Marine Management (RIKZ), The Hague, The Netherlands.

The primitive equations of the one-dimensional model are briefly discussed in Appendix B. More details their implementation into SLIM can be found in (de Brye et al., 2010).

The eddy viscosity ν is parameterized using the Smagorinsky formulation (2.91) with $c_\nu = 0.01$. The Chézy-Manning-Strickler formulation (2.93) is used to parameterize the bottom stress $\boldsymbol{\tau}^{\mathrm{b}}$, but here the Manning coefficient n is not constant, reflecting the varying properties of the seabed. Following the calibration by de Brye et al. (2010), it is equal to $0.0235\,\mathrm{s\,m^{-1/3}}$ in the European shelf and increases linearly along the estuary up to $0.028\,\mathrm{s\,m^{-1/3}}$ at the connexion with the one-dimensional model. The same value is kept upstream. The wind is considered as the only source of surface stress and its impact is parameterized using the formulation of Smith and Banke (1975):

$$\boldsymbol{\tau}^{\mathrm{s}} = 10^{-3}\big(0.630\|\boldsymbol{w}\| + 0.066\|\boldsymbol{w}\|^2\big)\boldsymbol{w}, \tag{3.19}$$

where $\boldsymbol{w}$ is the horizontal wind velocity vector, evaluated from NCEP reanalysis data of the wind at 10 m above the mean sea level (Kalnay et al., 1996).

The tide is forced at the shelf break using the elevation and velocity harmonics of the global tidal model TPXO7.1 (Egbert et al., 1994). Daily average data from different public data sources are used to take into account the influence of the Seine[2], the Thames[3], the Rhine and the Meuse[4], and the Scheldt and its main tributaries[5] at the upstream limits of the domain. On the coasts, the slip coefficient λ is parameterized so that $\lambda/\nu = 10^{-3}\,\mathrm{m^{-1}}$. The initial condition is zero for each variable. Even if a regime solution is reached after a few days, the simulation starts 20 days before the period of interest.

Around new and full moon, the influence of the Sun reinforces the influence of the Moon on the tidal motion. Those tides are called spring tides and they are characterized by higher amplitudes and a larger extent of the dry areas. The opposite phenomenon, when the axis Earth-Sun is orthogonal with the axis Earth-Moon, leads to the so-called neap tides, characterized by smaller amplitudes. Figure 3.15 displays the elevation of the water surface computed by the model at low tide during

[2]Data provided by the Groupement d'Intérêt Public (GIP) Seine-Aval.

[3]Data provided by the National River Flow Archive (NRFA).

[4]Data provided by the National Institute for Coastal and Marine Management (RIKZ) and Institute for Inland Water Management and Waste Water Treatment (RIZA).

[5]Data provided by the Hydrologic Information Centre (HIC).

a spring tide in the Scheldt Estuary. The extent of the dry areas is quite important and compares rather well with the satellite view presented in Figure 3.16.

In Figures 3.17 and 3.18, model outputs are confronted to measurement data from stations close to the Overloop van Hansweert (S1, Figure 1.2) and Baalhoek (S2, Figure 1.2) during year 2000[6]. Model outputs and measurement data are not easy to distinguish on Figure 3.17, partly because they are very similar, but also because the tidal variation period is quite small compared with the seasonal timescale. However, this figure illustrates very well the variation in amplitude from spring to neap tides. In Figure 3.18, thanks to the shorter timescale, the good model behavior regarding the measurement data can be observed.

More details about the calibration of the hydrodynamics module of SLIM may be found in de Brye et al. (2010).

3.5 Conclusion

The numerical discretization of the shallow water model presented in Chapter 2 is not designed to deal with the wetting and drying processes occurring in very shallow areas. The objective of this chapter was to present a solution to that problem for two different modeling strategies experimented during this thesis.

The flux-limiting method is exclusively designed for finite element models using a P_1^{DG} discretization for the elevation of the water surface and explicit time integration method. It is rather robust and passes all the test cases considered. However, explicit time integration methods require the use of rather small time steps, so that the computer cost becomes too high with the current version of SLIM, which is not optimized to be computationally efficient. Although the next version of SLIM is developed in that direction, another wetting-drying has been proposed in the meanwhile.

The modified bathymetry method has the drawback to be less successful in one of the test cases considered. However, it has no restriction on the time integration method. Using an implicit one, there is no more restriction on the time step. This becomes a crucial advantage when undertaking long-term environmental studies.

[6]Data provided by the Hydro Meteo Centrum Zeeland (HMCZ).

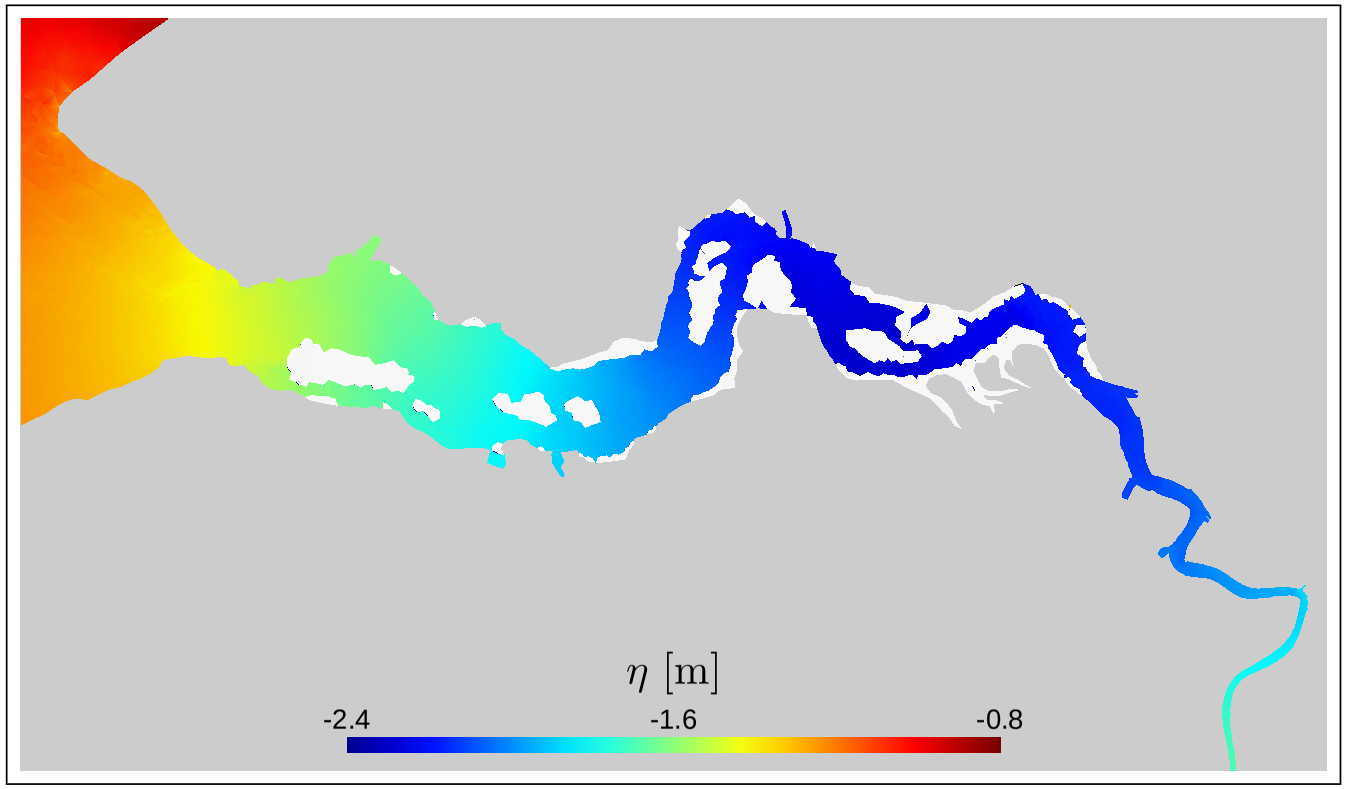

Figure 3.15: Elevation of the water surface above its reference level at low tide during a spring tide (March 8, 2000); white areas indicate that the water surface is below the original bathymetry.

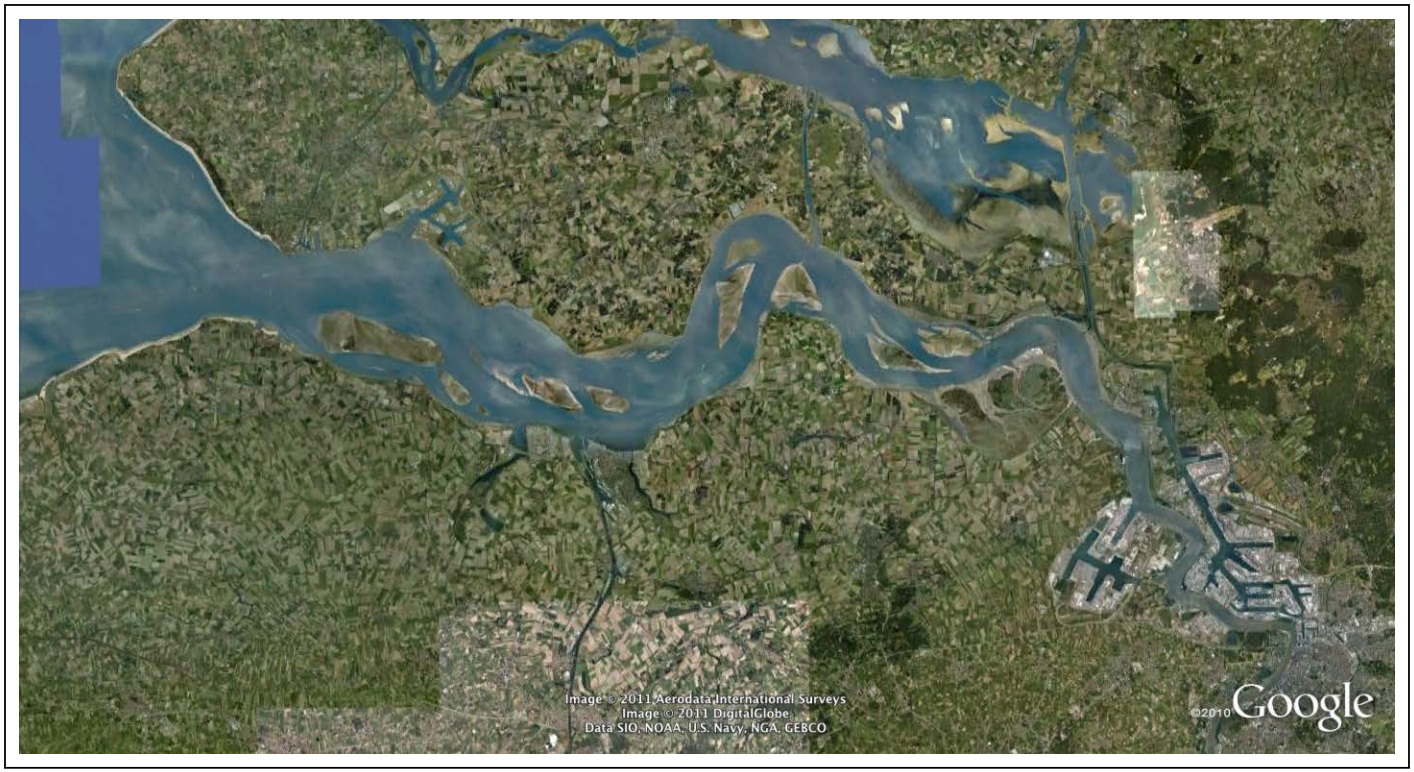

Figure 3.16: Satellite view of the tidal flats of the Scheldt Estuary (from Google Earth^{TM} mapping service).

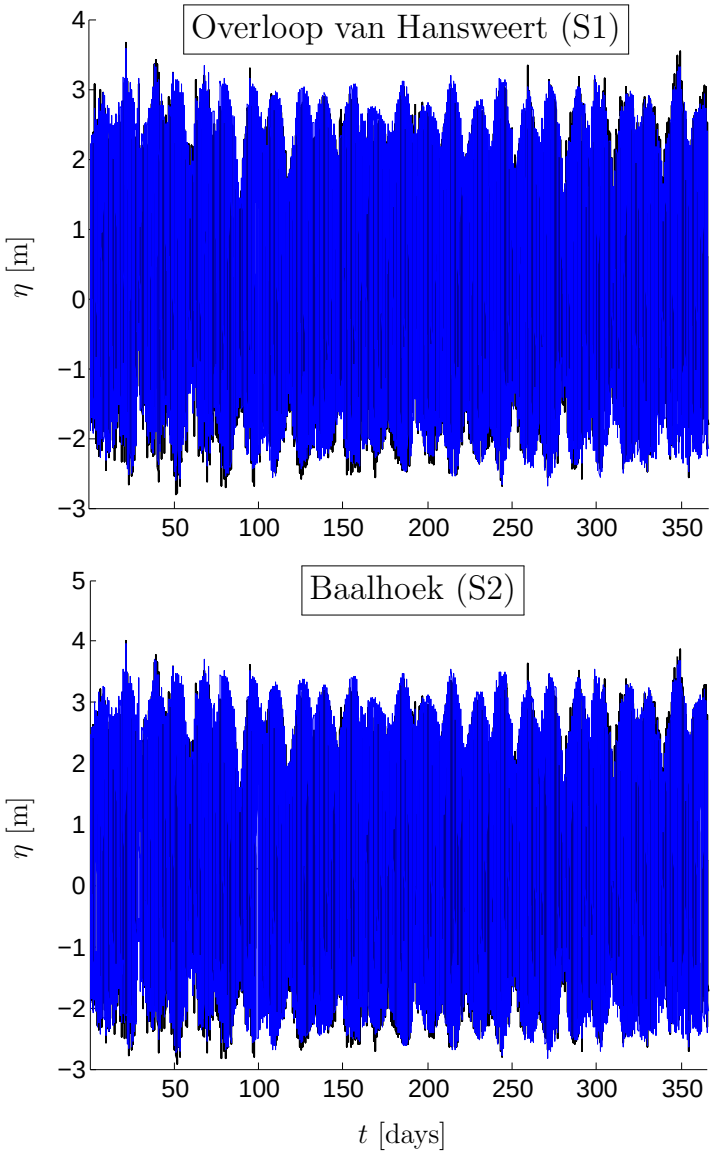

Figure 3.17: Elevation of the water surface above its reference level during year 2000; in black, data from station S1 (Overloop van Hansweert) and S2 (Baalhoek), provided by the Hydro Meteo Centrum Zeeland; in blue, model results at the same locations.

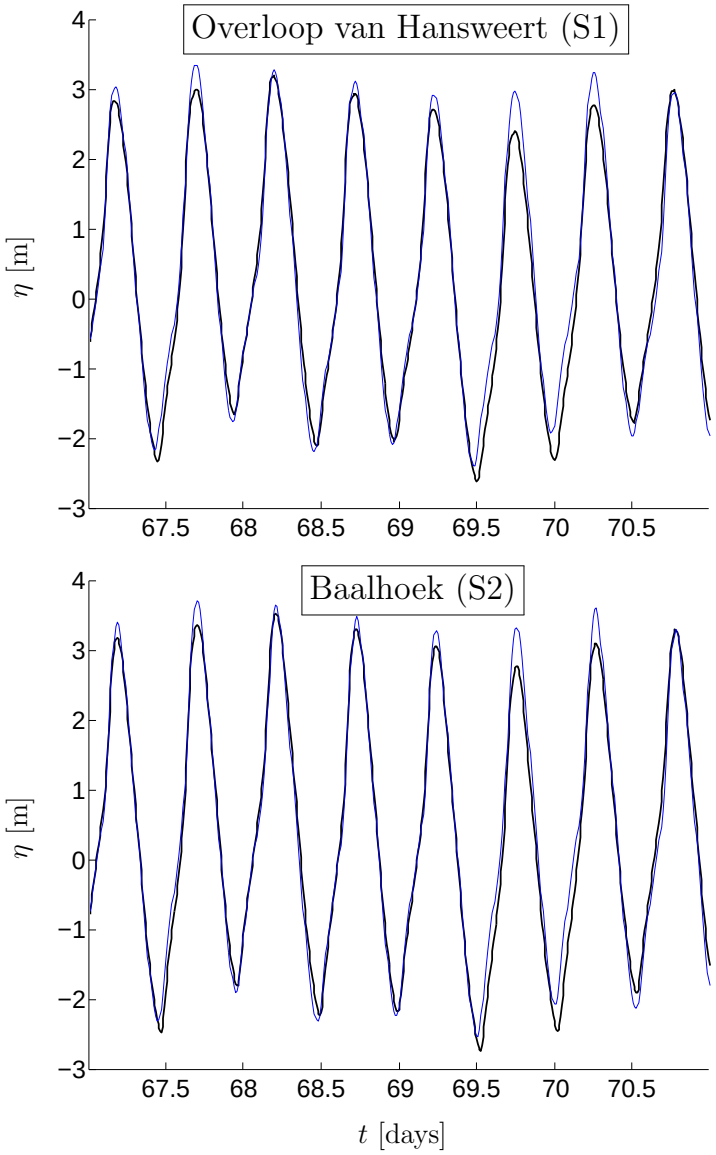

Figure 3.18: Elevation of the water surface above its reference level, from March 8, 2000 until March 12, 2000 (spring tide); in black, data from stations S1 (Overloop van Hansweert) and S2 (Baalhoek), provided by the Hydro Meteo Centrum Zeeland; in blue, model results at the same locations.

Chapter 4

Salinity transport

4.1 Introduction

Since 1978, oceanographers define salinity as the conductivity ratio of a sea water sample to a standard KCl solution. Being defined as a ratio, salinity has therefore no unit.

Salinity is considered as a passive tracer, because it is just transported through advection and diffusion. It is neither influenced by the presence of another tracer, nor it is produced or destroyed by any process. Modeling the salinity is therefore mainly important for the calibration of the transport processes. And this calibration is useful for the transport of other tracers such as the concentration of suspended sediments in Chapter 5. Moreover, modeling salinity is also important by itself since the salinity influences important properties such as the settling velocity of suspended sediments (by enhancing flocculation processes) or the partition between trace metal particles that are adsorbed or not on suspended sediments. Though this chapter is not an original contribution, it still illustrates how the transport of tracers is modeled using SLIM.

In Section 4.2, the general transport equation of a passive tracer is integrated over the water column to obtain its two-dimensional depth-averaged counterpart. Except for the possible additional reactive terms, the transport of any other tracer is governed by the same equation.

Section 4.3 describes how this equation is discretized in a finite element framework. Finally, in Section 4.4, the model is applied to compute the salinity dynamics in the Scheldt Estuary.

4.2 Governing equation

The three-dimensional tracer transport equation for the salinity S is:

$$\frac{\partial S}{\partial t} + \boldsymbol{v} \cdot \boldsymbol{\nabla} S = \boldsymbol{\nabla} \cdot (\kappa \boldsymbol{\nabla} S), \tag{4.1}$$

where κ is the molecular diffusivity. Attention must be paid that $\boldsymbol{\nabla}$ is here the three-dimensional del operator again, while, as a reminder, $\boldsymbol{v}$ is the three-dimensional velocity vector.

Reynolds equations for turbulent flows

As essentially all marine flows are turbulent, the quantities of equation (4.1) may be split into a slowly varying mean value and a random variation about it, similarly to what is done in Section 2.2 for the equations governing the hydrodynamics. For example:

$$S = \overline{S} + S'. \tag{4.2}$$

Introducing the splitting for each quantity of the equation, and taking the ensemble average, lead to an equation very similar to equation (4.1). The only difference is the presence of an additional term $\boldsymbol{\nabla} \cdot (\overline{\boldsymbol{v}' S'})$, accounting for the mixing of salinity due to turbulent processes. It is generally parameterized using an approach quite similar to that of the eddy viscosity, i.e.

$$\boldsymbol{\nabla} \cdot (\overline{\boldsymbol{v}' S'}) \triangleq \boldsymbol{\nabla} \cdot \left(\kappa_\mathrm{t} \boldsymbol{\nabla} \overline{S}\right), \tag{4.3}$$

where κ_t is called the turbulence eddy diffusivity, whose typical values are similar to those of the turbulence eddy viscosity, i.e. from 10^{-5} to $10^{-1}\,\mathrm{m^2\,s^{-1}}$, and therefore much larger than the molecular diffusivity κ. In what follows, the bars are omitted, and equation (4.1) is still used, remembering that it deals with Reynolds-averaged quantities and that the diffusivity is now the turbulence eddy diffusivity, which is not constant.

Typical scales and simplification of the equation

Using the non-inertial local basis, the diffusion term may developed as follows:

$$\boldsymbol{\nabla}\cdot(\kappa_\mathrm{t}\boldsymbol{\nabla}S) = \underbrace{\frac{\partial}{\partial x}\left(\kappa_\mathrm{t}\frac{\partial S}{\partial x}\right)+\frac{\partial}{\partial y}\left(\kappa_\mathrm{t}\frac{\partial S}{\partial y}\right)}_{\frac{\kappa_\mathrm{t}S}{L_\mathrm{h}}} + \underbrace{\frac{\partial}{\partial z}\left(\kappa_\mathrm{t}\frac{\partial S}{\partial z}\right)}_{\frac{\kappa_\mathrm{t}S}{L_\mathrm{v}}}. \tag{4.4}$$

According to the small aspect ratio $L_\mathrm{v}/L_\mathrm{h}$ of the flows under study in this doctoral dissertation (Table 2.2), the horizontal diffusion terms are much smaller than the vertical one, and are therefore neglected.

Taking advantage of the three-dimensional continuity equation (2.33), the tracer transport equation for the salinity becomes therefore:

$$\frac{\partial S}{\partial t}+\boldsymbol{\nabla}_\mathrm{h}\cdot(\boldsymbol{u}S)+\frac{\partial}{\partial z}(wS)=\frac{\partial}{\partial z}\left(\kappa_\mathrm{t}\frac{\partial S}{\partial z}\right), \tag{4.5}$$

where $\boldsymbol{u}$ is here the horizontal projection of the velocity vector again, and, as a reminder, $\boldsymbol{\nabla}_\mathrm{h}$ is the horizontal projection of the del operator and w is the vertical component of the velocity.

Depth-averaged equation

The integration of equation (4.5) is developed term by term:

$$\int_{-h}^{\eta}\frac{\partial S}{\partial t}\,dz = \frac{\partial}{\partial t}\big(H\overline{S}\big)-S_\mathrm{s}\frac{\partial \eta}{\partial t}, \tag{4.6}$$

$$\begin{aligned}\int_{-h}^{\eta}\boldsymbol{\nabla}_\mathrm{h}\cdot(\boldsymbol{u}S)\,dz &= \frac{\partial}{\partial x}\big(H\overline{\boldsymbol{u}}\overline{S}\big)+\boldsymbol{\nabla}_\mathrm{h}\cdot\int_{-h}^{\eta}(\boldsymbol{u}-\overline{\boldsymbol{u}})\big(S-\overline{S}\big)\,dz\\ &\quad -S_\mathrm{s}\boldsymbol{u}_\mathrm{s}\cdot\boldsymbol{\nabla}_\mathrm{h}\eta+S_\mathrm{b}\boldsymbol{u}_\mathrm{b}\cdot\boldsymbol{\nabla}_\mathrm{h}(-h),\end{aligned} \tag{4.7}$$

$$\begin{aligned}\int_{-h}^{\eta}\frac{\partial}{\partial z}(wS)\,dz &= [wS]_{-h}^{\eta}\\ &= w_\mathrm{s}S_\mathrm{s}-w_\mathrm{b}S_\mathrm{b}\\ &= S_\mathrm{s}\frac{\partial\eta}{\partial t}+S_\mathrm{s}\boldsymbol{u}_\mathrm{s}\cdot\boldsymbol{\nabla}_\mathrm{h}\eta-S_\mathrm{b}\boldsymbol{u}_\mathrm{b}\cdot\boldsymbol{\nabla}_\mathrm{h}(-h),\end{aligned} \tag{4.8}$$

$$\int_{-h}^{\eta}\frac{\partial}{\partial z}\left(\kappa_\mathrm{t}\frac{\partial S}{\partial z}\right)dz = \left[\kappa_\mathrm{t}\frac{\partial S}{\partial z}\right]_{-h}^{\eta}, \tag{4.9}$$

where S_s and S_b are the salinity evaluated at the surface and the bottom, respectively, and $\overline{S}$ is now the depth-averaged salinity defined as

$$\overline{S} = \frac{1}{H} \int_{-h}^{\eta} S \, dz. \tag{4.10}$$

As a reminder, $\overline{\boldsymbol{u}}$ is the depth-averaged horizontal velocity vector.

Among those expressions, some terms cannot be calculated explicitly in a horizontal two-dimensional model. They must be parameterized (or neglected). Moreover, some additional processes must be taken into account.

1. Phenomena are occurring at smaller scales than what the grid size allows. They are generally thought to be of a dissipative nature. By analogy with three-dimensional turbulence, it is commonly assumed that this can be treated using an eddy diffusivity formulation in terms of the depth-averaged salinity (Abbot and Price, 1994), i.e. by adding the following term in the right-hand side of the depth-averaged equation:

   $$\boldsymbol{\nabla}_\mathrm{h} \cdot (H \kappa_\mathrm{h} \boldsymbol{\nabla}_\mathrm{h} \overline{S}), \tag{4.11}$$

   where κ_h is the horizontal subgrid diffusivity. This parameterization has the advantage to conserve the tracer mass and to decrease monotonically the variance of the tracer concentration. Moreover, the dissipation only occurs when the salinity is not constant. The horizontal subgrid viscosity κ_h is generally parameterized in terms of the size of the grid. Typical values for the applications of this doctoral dissertation range from 1 to 100 $\mathrm{m^2\,s^{-1}}$.

2. In equation (4.7), the differential advection term,

   $$\boldsymbol{\nabla}_\mathrm{h} \cdot \int_{-h}^{\eta} (\boldsymbol{u} - \overline{\boldsymbol{u}})(S - \overline{S}) \, dz,$$

   describes a lateral salinity exchange due to differences in velocity over the depth of the flow, i.e. the shear effect. This may also be treated using an eddy diffusivity formulation in terms of the depth-averaged salinity gradient, by parameterizing the differential advection term as follows (Abbot and Price, 1994):

   $$-\boldsymbol{\nabla}_\mathrm{h} \cdot \int_{-h}^{\eta} (\boldsymbol{u} - \overline{\boldsymbol{u}})(S - \overline{S}) \, dz \triangleq \boldsymbol{\nabla}_\mathrm{h} \cdot (H \boldsymbol{\kappa}_\mathrm{s} \cdot \boldsymbol{\nabla}_\mathrm{h} \overline{S}), \tag{4.12}$$

where the shear diffusivity $\boldsymbol{\kappa}_\mathrm{s}$ (also usually called the shear dispersion) is a tensor. Unlike the shear viscosity, it is not always much smaller than the subgrid diffusivity and is therefore not likely to be neglected. The combined effects of the subgrid and shear diffusivities can be gathered in a horizontal diffusivity tensor:

$$\boldsymbol{\kappa} = \kappa_\mathrm{h}\boldsymbol{\delta} + \boldsymbol{\kappa}_\mathrm{s}. \tag{4.13}$$

3. The right-hand part of equation (4.9) can be neglected. Indeed, considering that there is no salinity flux through the water surface and the bottom, the following conditions are applicable:

$$(\boldsymbol{\nabla} S)\cdot\boldsymbol{n} = 0 \qquad \text{if } z=\eta \text{ or } z=-h, \tag{4.14}$$

where $\boldsymbol{n}$ is the local vector normal to the boundary. Since the water surface and bottom slopes are generally much smaller than unity, the vector $\boldsymbol{n}$ is almost aligned with the vertical direction $\boldsymbol{e}_z$ at the water surface and at the bottom, so that

$$(\boldsymbol{\nabla} S)\cdot\boldsymbol{n} \approx \frac{\partial S}{\partial z} \approx 0 \qquad \text{if } z=\eta \text{ or } z=-h. \tag{4.15}$$

The depth-averaged tracer transport equation for salinity becomes therefore:

$$\frac{\partial}{\partial t}\big(H\overline{S}\big) + \boldsymbol{\nabla}_\mathrm{h}\cdot\big(H\overline{\boldsymbol{u}}\overline{S}\big) = \boldsymbol{\nabla}_\mathrm{h}\cdot\big(H\boldsymbol{\kappa}\cdot\boldsymbol{\nabla}_\mathrm{h}\overline{S}\big), \tag{4.16}$$

Finally, since only two-dimensional horizontal flows are considered, the subscript "h" and the bar overlining the depth-averaged quantities are omitted thereafter. Moreover, the anisotropic effect of the shear dispersion has not been taken into account in this work. The horizontal diffusivity is therefore considered as a scalar. It is a drawback in the present version of the model that must be corrected in the near future. Anyway, the depth-averaged equation governing the transport of salinity reads therefore:

$$\frac{\partial}{\partial t}(HS) + \boldsymbol{\nabla}\cdot(H\boldsymbol{u}S) = \boldsymbol{\nabla}\cdot(H\kappa\boldsymbol{\nabla} S). \tag{4.17}$$

4.3 Numerical model

4.3.1 Spatial discretization

A necessary condition for a tracer to be consistently conservative is the use of the same discretization as for the elevation η (White et al., 2008b). The salinity is therefore also represented by a P_1^{DG} approximation:

$$S \simeq S^h = \sum_{j=1}^{3N_e} S_j \phi_j, \tag{4.18}$$

where S_j is the salinity nodal value at node j and ϕ_j is the associated shape function.

Weak formulation

The weak formulation of equation (4.17) is obtained by integrating it over the whole domain of interest, against an admissible test function $\hat{S}$ belonging to the suitable functional space. Since the model domain is divided into a set of non overlapping elements Ω_e, it reads:

$$\sum_e \left(< \frac{\partial}{\partial t}(HS)\hat{S} >_e + < \boldsymbol{\nabla} \cdot (H\boldsymbol{u}S)\hat{S} >_e \right) = \sum_e < \boldsymbol{\nabla} \cdot (H\kappa \boldsymbol{\nabla} S)\hat{S} >_e . \tag{4.19}$$

Integrating by parts the advection and diffusion terms leads to:

$$\sum_e \left(< \frac{\partial}{\partial t}(HS)\hat{S} >_e + < \boldsymbol{\nabla} \cdot (H\boldsymbol{u}S\hat{S}) >_e - < H\boldsymbol{u}S \cdot \boldsymbol{\nabla}\hat{S} >_e \right) = \sum_e \left(< \boldsymbol{\nabla} \cdot \left(H\kappa(\boldsymbol{\nabla} S)\hat{S} \right) >_e - < H\kappa(\boldsymbol{\nabla} S) \cdot (\boldsymbol{\nabla}\hat{S}) >_e \right). \tag{4.20}$$

Using Stoke's divergence theorem:

$$\sum_e \left(< \frac{\partial}{\partial t}(HS)\hat{S} >_e + \ll Hu_n S\hat{S} \gg_e - < H\boldsymbol{u}S \cdot \boldsymbol{\nabla}\hat{S} >_e \right) = \sum_e \left(\ll H\kappa \frac{\partial S}{\partial n}\hat{S} \gg_e - < H\kappa(\boldsymbol{\nabla} S) \cdot (\boldsymbol{\nabla}\hat{S}) >_e \right). \tag{4.21}$$

Finite element formulation

The finite element formulation of equation (4.17) is obtained by replacing all the variables by their finite element approximations in equation (4.21):

$$\sum_e \left(< \frac{\partial}{\partial t}\left(HS^h\right)\hat{S} >_e + \ll \left(h + \left(\eta^h\right)^*\right)\left(u_n^h\right)^*\left(S^h\right)^*\hat{S} \gg_e \right.$$
$$\left. - < H\boldsymbol{u}S^h \cdot \boldsymbol{\nabla}\hat{S} >_e \right)$$
$$= \sum_e \left(\ll H\kappa\left\{\frac{\partial S^h}{\partial n}\right\}\hat{S} \gg_e - < H\kappa(\boldsymbol{\nabla}\hat{S}) \cdot (\boldsymbol{\nabla}S^h) >_e \right). \quad (4.22)$$

As the hydrodynamic variables, the salinity needs to be uniquely defined for both neighboring elements at their interface when using discontinuous discretization methods.

In the contour integrals from the advection term, the value of the salinity is therefore also denoted with a star superscript. It is determined with a classical upwind scheme: $\left(S^h\right)^*$ is equal to the external value of S^h where the flow enters the element, it is equal to the internal value otherwise. When computing contour integrals on the boundary Γ of the model domain, elements have no neighbors. In the case of an open boundary, the external values are estimated using external data. In the case of a coast, since u_n^h is supposed to be zero, the entire integral is cancelled. The values of the hydrodynamic variables on the contour integrals are determined with the Riemann solver described in Section 2.3.1, exactly the same way as in equations (2.65) and (2.70).

In the contour integrals from the diffusion term, $\{\partial S^h/\partial n\}$ is taken as the mean of the internal and the external values. As for the dissipative terms in the momentum conservation equation, using a discontinuous discretization method requires a specific treatment to obtain a stable and accurate representation of the dispersion effects. The IP method is also used here. It consists in adding the following term in the right-hand side of equation (4.22):

$$-\sum_e \ll \sigma\left(h + \left(\eta^h\right)^*\right)\hat{S}\left[S^h\right] \gg_e, \quad (4.23)$$

where σ is the penalty parameter and $\left[S^h\right]$ is the salinity jump:

$$\left[S^h\right] = \frac{S^h_{\text{int}} - S^h_{\text{ext}}}{2}, \quad (4.24)$$

where S^h_{int} and S^h_{ext} are the internal and external values of S^h, respectively. The parameterization used for σ is similar to that proposed by Shahbazi (2005):

$$\sigma = \frac{\kappa(p+1)(p+2)}{d_e}, \tag{4.25}$$

where p is here the interpolation order of the approximation of the field considered ($p = 1$ for P_1^{DG} elements), and d_e is a typical length scale of the element Ω_e. On the boundary Γ of the model domain, the external value S^h_{ext} is determined as in the contour integrals from the advection term. In the case of a coast, the external value is taken equal to the internal one.

Galerkin procedure

The Galerkin procedure amounts to replace $\hat{S}$ by ϕ_i for $1 \leq i \leq 3N_e$ in equation (4.22) (Hanert et al., 2004). This results in a system of $3N_e$ ordinary differential equations, which are necessary to compute the $3N_e$ nodal values of S^h introduced in relation (4.18). This system can be synthesized on the following matrix form:

$$\frac{d}{dt}\big(\boldsymbol{A}_S \cdot \boldsymbol{S}\big) = \boldsymbol{b}_S\big(t, \boldsymbol{S}(t)\big). \tag{4.26}$$

The matrix $\boldsymbol{A}_S$ is a $(3N_e, 3N_e)$ squared matrix whose entries are

$$(A_S)_{ij} = < H\phi_i\phi_j >_{e(i)}, \tag{4.27}$$

the subscript $e(i)$ pointing to the element for which ϕ_i is not zero everywhere. The $(3N_e, 1)$ vector $\boldsymbol{S}$ gathers all the nodal values S_j of the salinity field. The left-hand part of equation (4.26) corresponds to terms of equation (4.22) that contain time derivatives. The $(3N_e, 1)$ vector $\boldsymbol{b}_S$ gathers all the other terms.

4.3.2 Temporal integration

Runge-Kutta methods are also used to integrate equation (4.26) in time. However, in this case, the mass matrix $\boldsymbol{A}_S$ is a function of the water depth H and is therefore time-dependent:

$$\boldsymbol{A}_S^{n+1} \cdot \boldsymbol{S}^{n+1} = \boldsymbol{A}_S^{n} \cdot \boldsymbol{S}^{n} + \Delta t \sum_{i=1}^{s} \beta_i (\boldsymbol{k}_S)_i, \tag{4.28}$$

where $\boldsymbol{S}^n$ and $\boldsymbol{S}^{n+1}$ are the vector $\boldsymbol{S}$ at time t^n and t^{n+1}, respectively, $\boldsymbol{A}^n$ and $\boldsymbol{A}^{n+1}$ are the matrix $\boldsymbol{A}$ at time t^n and t^{n+1}, respectively, and

$$(\boldsymbol{k}_S)_i = \boldsymbol{b}_S\left(t^n + \gamma_i \Delta t, \boldsymbol{S}^n + \sum_{j=1}^{s} \alpha_{ij} \Delta t \ (\boldsymbol{k}_S)_j\right). \tag{4.29}$$

Also here, the functions $(\boldsymbol{k}_S)_i$ may be seen as evaluations of $\boldsymbol{b}_S$ at sub-time steps. Here, because it is time-dependent, the mass matrix must be updated at each sub-time step. In what follows, only the implicit DIRK222 scheme (Section 2.3.2) is used.

4.3.3 Consistency

For a tracer to be consistently conservative, the discretization of its governing equation must be consistent with the discretization of the mass conservation equation, i.e. if the tracer is 1 everywhere, the discretization of its governing equation must be equivalent to the discretization of the mass conservation equation (White et al., 2008b).

To that end, a P_1^{DG} approximation is used for both the elevation η and the salinity S. Indeed, if $S^h = 1$ everywhere, the finite element formulation (4.22) of the salinity transport equation is equivalent to the finite element formulation (2.71) of the mass conservation equation, considering that both $\hat{S}$ and $\hat{\eta}$ are replaced by the same shape functions ϕ_i during the Galerkin procedure. Therefore, if the same time integration scheme is used for each equation, the tracer will be consistently conservative.

The treatment of the wetting and drying processes also affects the equation governing the salinity transport. The flux-limiting method is not discussed here. Indeed, as already mentioned, this wetting-drying method requires explicit time integration schemes that would lead to unacceptably long simulations with the current version of the model. On the other hand, when using the modified bathymetry method, the wetting-drying treatment of the salinity transport equation is quite obvious. If the water thickness H is replaced by the redefined water thickness $\tilde{H}$ in the primitive equation (4.17), the discrete formulation is similar to that of the mass conservation equation if $S^h = 1$ everywhere. Then, Kärnä et al. (2011a) show that the salinity remains consistently conservative if the appropriate Riemann solver is used to evaluate the contour integrals.

4.4 Modeling the salinity of the Scheldt Estuary

In order to be consistent with the setup to compute the hydrodynamics of the Scheldt Estuary (Section 3.4), the setup to compute the salinity is very similar. The mesh is that shown on Figure 1.2. The DIRK222 implicit time integration scheme (Section 2.3.2) is used with a time step of 15 minutes. The bathymetry is based on ETOPO1 (Amante and Eakins, 2008) in the European shelf and on data from the KustZuid model[1] in the Scheldt Estuary. The wetting and drying processes are dealt with the modified bathymetry method, with the smoothing parameter $\alpha = 0.5\,\mathrm{m}$. Upstream of Antwerp, a one-dimensional section-averaged model is used. The primitive equations of the one-dimensional model are briefly discussed in Appendix B. More details their implementation into SLIM can be found in (de Brye et al., 2010).

The diffusivity of the salinity is parameterized using the formulation from Okubo (1971):

$$\kappa = c_\kappa {d_e}^{1.15}, \tag{4.30}$$

where c_κ is a constant that is calibrated to a value of $0.03\,\mathrm{m}^{0.85}\,\mathrm{s}^{-1}$ by de Brye et al. (2010) in order to obtain optimal results in the Scheldt Estuary with SLIM, and d_e is the characteristic length of the element. This value of c_κ will be of use for any other tracer.

Concerning the boundary conditions, freshwater ($S = 0$) enters the domain from the upstream limits of the one-dimensional tidal river network model, from the Ghent-Terneuzen and Bath canals, from the Antwerp harbor locks, and from the Seine, Thames, Meuse and Rhine Rivers. Precipitation and evaporation are of negligible importance compared to the freshwater flows entering the domain through the upstream boundaries. They are therefore not taken into account. The salinity outside of the Southern Bight is relaxed towards monthly climatological data (Berx and Hughes, 2009). The initial condition is based on a long time averaged profile (Soetaert et al., 2006), so that a regime solution is quickly reached. The simulation still starts 20 days before the period of interest.

More details about the calibration of the salinity module may be found in de Brye et al. (2010). However, to illustrate the rather good

[1]Courtesy of M. Zijlema from the National Institute for Coastal and Marine Management (RIKZ), The Hague, The Netherlands.

behavior of the model, outputs are here compared with measurement data from stations close to the Overloop van Hansweert (S1, Figure 1.2) and Baalhoek (S2, Figure 1.2) during year 2000[2] in Figures 4.1 and 4.2. The differences between model outputs and measurements data are here slightly apparent on the seasonal timescale. Compared to the variations in the water surface elevation, the evolution of the salinity is more difficult to represent because other processes than the tides are involved. For example, the seasonal variation in the salinity dynamics, mainly due to the seasonal variation of the river discharge, is more important than the variation at the tidal scale (Baeyens et al., 1998c). Nevertheless, observing the results at a smaller timescale (Figure 4.2) allows to notice a rather good behavior of the model.

In Figure 4.3, the model outputs of the same simulation are compared with an analytical salinity profile proposed by Soetaert et al. (2006) from measurements gathered between 1965 and 2002.

4.5 Conclusion

The objective of this chapter was to present the two-dimensional depth-averaged equation governing the dynamics of a passive tracer, and its discretization in a finite element framework. Its application to compute the salinity dynamics in the Scheldt Estuary allowed to validate the modeling of the horizontal transport processes of any tracer and to calibrate the diffusivity parameterization.

[2]Data provided by the Hydro Meteo Centrum Zeeland (HMCZ).

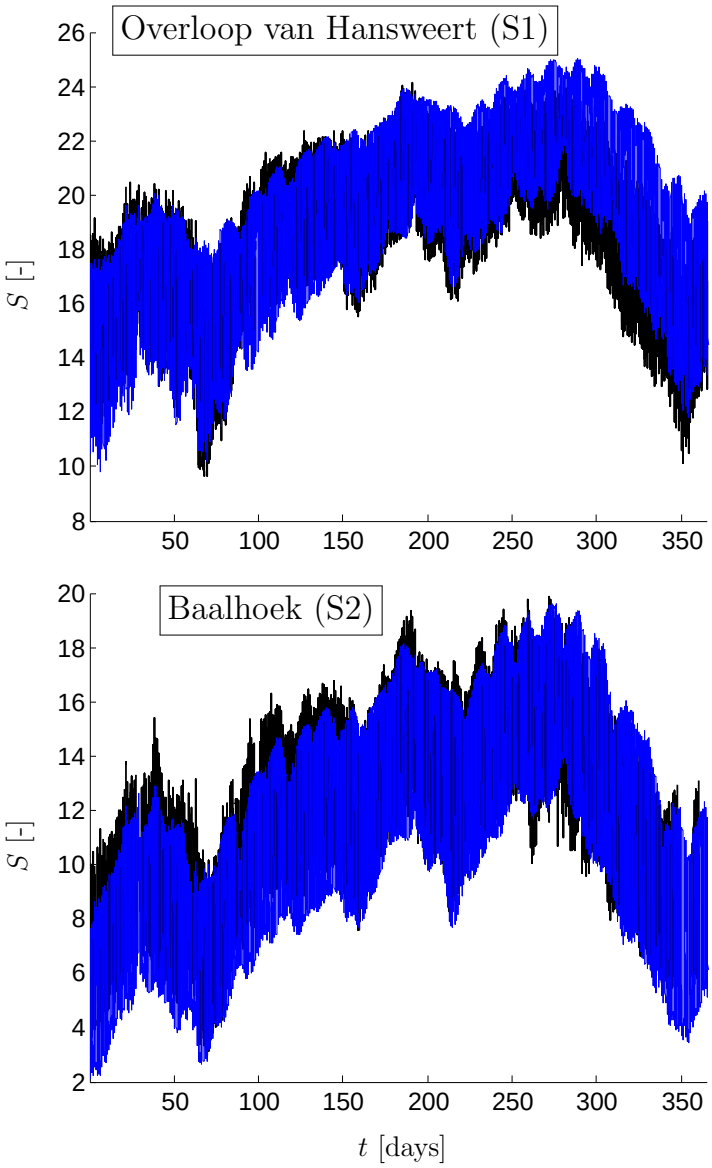

Figure 4.1: Depth-averaged salinity during year 2000; in black, data averaged from measurements at two different levels of stations S1 (Overloop van Hansweert) and S2 (Baalhoek), provided by the Hydro Meteo Centrum Zeeland; in blue, model results at the same locations.

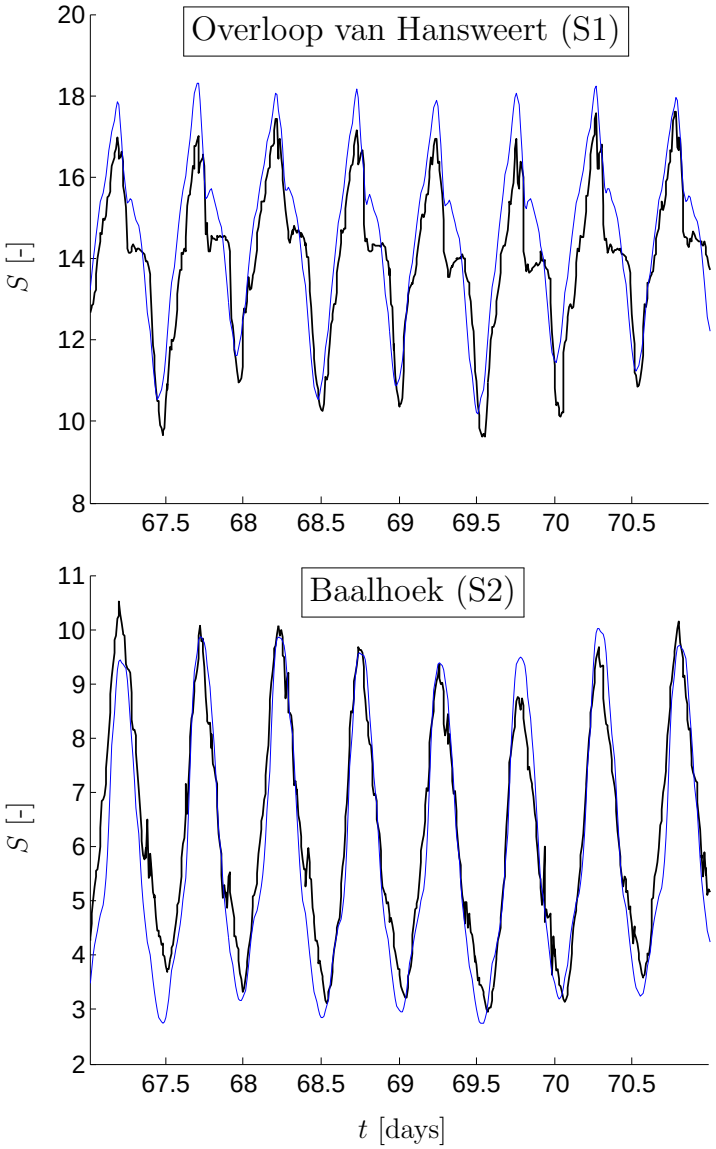

Figure 4.2: Depth-averaged salinity, from March 8, 2000 until March 12, 2000; in black, data averaged from measurements at two different levels of stations S1 (Overloop van Hansweert) and S2 (Baalhoek), provided by the Hydro Meteo Centrum Zeeland; in blue, model results at the same locations.

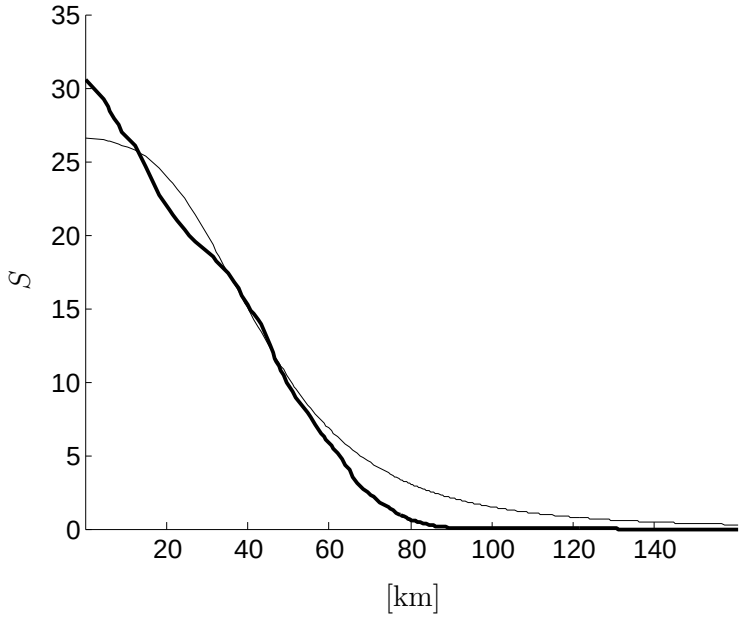

Figure 4.3: Longitudinal profile of the mean salinity, from the mouth (km 0) to Ghent (km 160); the thick line is obtained from model results averaged over year 2000, and the thin line is an analytical profile proposed by Soetaert et al. (2006) from measurements gathered between 1965 and 2002.

Chapter 5

Sediment dynamics

This chapter is based on the following publication:
Gourgue, O., Baeyens, W., Chen, M., de Brauwere, A., de Brye, B., Deleersnijder, E., Elskens, M., and Legat, V. A depth-averaged two-dimensional sediment transport model for environmental studies in the Scheldt Estuary and tidal river network, *Journal of Marine Systems* (submitted).

5.1 Introduction

The subject of this chapter is the development of a suitable set of equations and parameter values to accurately represent the sediment dynamics in the tidal part of the Scheldt Basin. The aim is not to build yet another sophisticated sediment transport model such as those of van der Wal et al. (2010) and van Kessel et al. (2011). Instead, the goal is to build a simplified sediment transport model, for the purpose of conducting long-term environmental simulations to analyze the behavior of biogeochemical pollutants in association with sediments.

The Scheldt is a relatively turbid estuary with three ETMs. The most important one is located in the area of Antwerp (Figure 1.2). Another one is reported upstream in the tidal river and a third one is located downstream of the mouth (Chen et al., 2005b; Chen and Wartel, 2009), and therefore outside of the domain of interest of this study. The suspended sediment concentration (SSC) exhibits variability at different

timescales. The variations at the tidal and spring/neap cycle scales are closely linked to the hydrodynamic regime (Chen et al., 2005b; Arndt et al., 2007). However, the estuary undergoes seasonal variations too (the turbidity is higher in winter than in summer) that cannot be explained by the hydrodynamics alone, and often are associated with water discharge and sediment supply (Chen and Wartel, 2009; van der Wal et al., 2010). Therefore, even if the goal is to design a sediment module that is as simple as possible, additional processes must be taken into account. The features that have to be accurately represented are

- the order of magnitude of the SSC throughout the estuary and the tidal river network;
- the variations of the SSC at the tidal, spring/neap cycle and seasonal timescales;
- the location of the main ETMs.

If these conditions are met, this simplified sediment transport model will be considered to be satisfactory to undertake long-term biogeochemical environmental studies.

The governing equations are presented in Section 5.2. Since they are rather similar to that governing the salinity dynamics, their numerical implementation is only briefly discussed in Section 5.3. The parameterizations of the sediment processes to represent satisfactorily the sediment dynamics of the Scheldt Estuary and tidal river network are then discussed in Section 5.4.

5.2 Governing equations

Three layers are taken into account in the sediment module: the water column where the sediments are in suspension, a layer made up of sediments freshly deposited on the bottom, and a parent layer underneath the latter (Figure 5.1). Although three layers are considered, the module is only made up of two interacting variables, i.e. C_{ss}, the depth-averaged concentration of sediments in suspension [$\mathrm{kg\,m^{-3}}$], and C_{sb}, the concentration of bottom sediments in the fresh layer [$\mathrm{kg\,m^{-2}}$]. The parent layer is an infinite source of sediments that is only eroded when C_{sb} is locally zero.

The concentration of suspended sediments may be seen as an active tracer, i.e. it is transported exactly as salinity is in equation (4.17), with

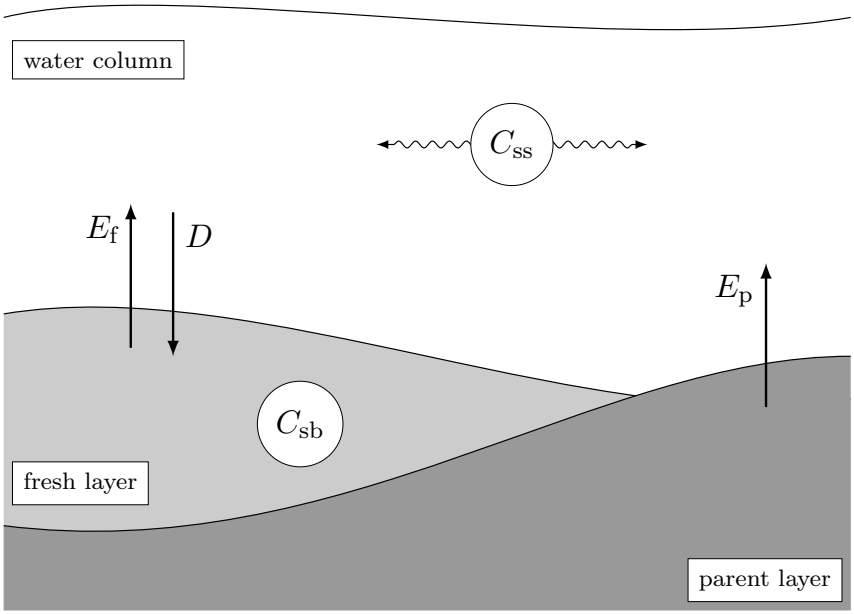

Figure 5.1: Schematic representation of the sediment module; C_{ss} is the depth-averaged concentration of sediments in suspension and C_{sb} is the concentration of bottom sediments in the fresh layer; E_f is the erosion rate of sediments from the fresh layer, E_p is the erosion rate of sediments from the parent layer, and D is the deposition rate of sediments on the fresh layer.

additional source/sink terms to take into account the vertical exchange of sediments with the bottom layers:

$$\frac{\partial}{\partial t}(HC_{ss}) + \boldsymbol{\nabla} \cdot (H\boldsymbol{u}C_{ss}) = \boldsymbol{\nabla} \cdot (H\kappa\boldsymbol{\nabla}C_{ss}) + E_f + E_p - D, \qquad (5.1)$$

where E_f is the erosion rate of sediments from the fresh layer, E_p is the erosion rate of sediments from the parent layer, and D is the deposition rate of sediments on the fresh layer. These three erosion/deposition rates are a priori unknown and have to be parameterized. The sediments of the bottom fresh layer are not transported horizontally and only exchange of sediments with the water column allows to change their concentration:

$$\frac{\partial C_{sb}}{\partial t} = D - E_f. \qquad (5.2)$$

In the present version of the sediment module, it is assumed that the parent layer is never supplied and that there is no exchange between the two bottom layers. Moreover, bed-load transport is not taken into account[1]. These assumptions are consistent with the aim of designing a sediment module that is as simple as possible.

To summarize, the equations governing the fine sediment dynamics for a depth-averaged model are:

$$\frac{\partial}{\partial t}(HC_{\rm ss}) + \boldsymbol{\nabla}\cdot(H\boldsymbol{u}C_{\rm ss}) = \boldsymbol{\nabla}\cdot(H\kappa\boldsymbol{\nabla}C_{\rm ss}) + E_{\rm f} + E_{\rm p} - D, \quad (5.1)$$

$$\frac{\partial C_{\rm sb}}{\partial t} = D - E_{\rm f}. \quad (5.2)$$

With this formulation, the sum $(HC_{\rm ss}+C_{\rm sb})$ must be globally conserved in an enclosed domain with no supply from the parent layer, whatever the parameterizations of the different erosion and deposition rates.

5.3 Numerical model

The discretization of the sediment equations is very similar to the discretization of the salinity equation. The whole procedure is therefore not transcribed here. As salinity or any other tracer transported in the water column, for consistency reasons, the suspended sediment concentration $C_{\rm ss}$ needs the same spatial discretization as the elevation η. It is therefore also represented by a $P_1^{\rm DG}$ approximation. The weak and finite element formulations of equation (5.1) and the Galerkin procedure lead to a system of ordinary differential equations that can be synthesized in a matrix form very similar to equation (4.26) for the salinity. The only major difference is the addition of the following extra source/sink term in each entry of the right-hand side vector:

$$< (E_{\rm f} + E_{\rm p} - D)\phi_i >_{e(i)} . \quad (5.3)$$

[1]Nevertheless, to allow for a rough redistribution of sediments on the bottom, a simple Laplacian operator is added to equation (5.2), with a diffusion coefficient of $30\,{\rm m}^2\,{\rm s}^{-1}$. Because both bottom layers have the same properties in this preliminary study, this diffusion has no influence on the suspended sediment concentration, which is the only subject of interest in this chapter.

The equation (5.2) governing the bottom sediment concentration C_{sb} can be seen as a simplified version of the transport equation, with a source/sink term, but with $H = 1$, $\boldsymbol{u} = 0$ and $\kappa = 0$. As a consequence, and regardless of the type of finite element approximation, the weak and finite element formulations of equation (5.2) and the Galerkin procedure also lead to a system of ordinary differential equations that can be synthesized in a matrix form very similar to equation (4.26) for the salinity. In this case, the extra source/sink term added in each entry of the right-hand side vector reads

$$< (D - E_{\mathrm{f}})\psi_i >_{e(i)}, \tag{5.4}$$

where ψ_i is the shape function corresponding to the finite element type chosen for C_{sb}. In order to globally conserve the sum $(HC_{\mathrm{ss}} + C_{\mathrm{sb}})$ in an enclosed domain with no supply from the parent layer, it is clear that ψ_i must be equal to ϕ_i. The P_1^{DG} approximation is therefore also used for the bottom sediment concentration C_{sb}. Finally, the temporal integration is performed exactly the same way as salinity for both equations (Section 4.3.2).

5.4 Modeling the sediments dynamics in the Scheldt Estuary

In most of the Scheldt Estuary, the SSC is about a few tens of $\mathrm{g\,m^{-3}}$. Values may attain $0.5\,\mathrm{kg\,m^{-3}}$ in the area of the most significant ETM around Antwerp. It corresponds more or less to the area between the Belgian-Dutch border and the confluence with the Rupel (Figure 1.2). The large tidal energy is responsible for the formation of this main ETM (Chen et al., 2005b; Arndt et al., 2007). A second ETM occurs in the tidal river where the SSC may reach $0.3\,\mathrm{kg\,m^{-3}}$ (Chen et al., 2005b). Finally, a third one is located downstream of the mouth. It is marine-dominated and characterized by high wave energy with SSC attaining $0.2\,\mathrm{kg\,m^{-3}}$ (Fettweis and Van den Eynde, 2003).

The SSC also undergoes variations at different timescales. The hydrodynamics seems to be directly responsible for the SSC variations observed at the tidal scale (period of a few hours) and at the spring/neap cycle scale (period of a few weeks) because they follow the tidal regime (Chen et al., 2005b; Arndt et al., 2007). In addition, the SSC is two or three times higher in winter than in summer, which cannot be explained by the water discharge variations alone. In order to represent

this variability, other forcings or processes must be taken into account (Chen and Wartel, 2009; van der Wal et al., 2010).

The parameterizations of the erosion rates are based on a formula introduced by Partheniades (1965), and that is now widely used (e.g. Burchard et al., 2004; Arndt et al., 2007; Mercier and Delhez, 2007):

$$E_{\mathrm{f}} = \begin{cases} M\left(\dfrac{\tau_{\mathrm{b}}}{\tau_{\mathrm{e}}} - 1\right) & \text{if } \tau_{\mathrm{b}} > \tau_{\mathrm{e}} \text{ and } C_{\mathrm{sb}} > 0, \\ 0 & \text{otherwise,} \end{cases} \tag{5.5}$$

$$E_{\mathrm{p}} = \begin{cases} M\left(\dfrac{\tau_{\mathrm{b}}}{\tau_{\mathrm{e,p}}} - 1\right) & \text{if } \tau_{\mathrm{b}} > \tau_{\mathrm{e,p}} \text{ and } C_{\mathrm{sb}} = 0, \\ 0 & \text{otherwise.} \end{cases} \tag{5.6}$$

Sediments are eroded from the fresh layer when τ_{b} (the norm of the bottom stress vector $\boldsymbol{\tau}^{\mathrm{b}}$) is higher than a threshold value τ_{e}, or, if the fresh layer is locally empty, from the parent layer when τ_{b} is higher than another threshold value $\tau_{\mathrm{e,p}}$; M is called, in a slightly improper way, the erosion velocity. As in many other studies (e.g. Burchard et al., 2004; Arndt et al., 2007; Mercier and Delhez, 2007), the parameterization of the deposition rate is based on a formula introduced by Einstein and Krone (1962):

$$D = w_{\mathrm{s}} C_{\mathrm{ss,b}}, \tag{5.7}$$

where w_{s} is the settling velocity and $C_{\mathrm{ss,b}}$ is the SSC just above the bottom. In depth-averaged models, $C_{\mathrm{ss,b}}$ is usually taken to be three times the depth-averaged SSC:

$$C_{\mathrm{ss,b}} = 3C_{\mathrm{ss}}, \tag{5.8}$$

which is confirmed by the field data collected in the Scheldt by Chen et al. (2005a).

As a first attempt, the erosion parameters M, τ_{e} and $\tau_{\mathrm{e,p}}$ are considered as constants, with $\tau_{\mathrm{e,p}} = \tau_{\mathrm{e}}$. Considering the dynamics of fine sediments, the same hypothesis cannot be made for the settling velocity w_{s}, which is greatly influenced by flocculation. Flocculation refers to the processes by which suspended sediments attach to each other to form bigger structures called flocs, modifying the sediment properties, in particular the settling velocity (Wolanski, 1995; Winterwerp, 2002). One of the main factors influencing the flocculation of suspended sediments is the SSC itself: the higher is the SSC, the higher is the number of collisions of suspended particles per unit of time, increasing their probability

to aggregate (van Leussen, 1999; Chen et al., 2005a; Chen, 2009; Pejrup and Mikkelsen, 2010). The weight and, as a consequence, the settling velocity of the flocs are also affected accordingly. In this article, this is taken into account by using the following parameterization:

$$w_{\mathrm{s}} = w_{\mathrm{s},0}\left(\frac{C_{\mathrm{ss}}}{C_{\mathrm{ss},0}}\right)^{m}, \tag{5.9}$$

where $C_{\mathrm{ss},0} = 0.1\,\mathrm{kg\,m^{-3}}$ is the reference value of the SSC, $w_{\mathrm{s},0}$ is the associated reference settling velocity whose value is determined empirically, and m is a coefficient between 0.5 and 3.5 (van Leussen, 1999). For want of any empirical estimates of parameter m in the Scheldt, the value of the latter is arbitrarily taken to be equal to unity. Other values were tested in the framework of this study, but none appeared to lead to a significant improvement of the results.

When dealing with only one type of sediments, only three parameters must therefore be calibrated: M, τ_{e} and $w_{\mathrm{s},0}$. If several types of sediments are dealt with, the number of parameters to calibrate is obviously multiplied by the number of sediment types. For the sake of simplicity, only one type is considered in this first study, where the values assigned to the three parameters determine the type of sediments under study. Fine sediments (silt and clay) are considered here because of their importance in the crucial zones like the main ETM and their interaction with contaminants (Baeyens et al., 1998c).

The setup to compute the sediment dynamics in the Scheldt Estuary is the same as that used to compute the hydrodynamics and the salinity dynamics (Sections 3.4 and 4.4). Upstream of Antwerp, a one-dimensional section-averaged model is used. The primitive equations of the one-dimensional model are briefly discussed in Appendix B. Upstream boundary conditions of SSC are provided by outputs of the Seneque/Riverstrahler model (Thieu et al., 2009). The initial condition is zero for the variables of the sediment module and the simulations start 20 days before the period of interest. A regime solution is reached after 10 days for the SSC. This takes longer for the bottom variable. However, as long as equations (5.5) and (5.6) are used with $\tau_{\mathrm{e}} = \tau_{\mathrm{e,p}}$, both bottom layers have the same properties and the fresh layer is only useful to keep track of the sediments entered in the domain through the parent layer or the open boundaries. Therefore, under these conditions, and as long as the study does not focus specifically on the bottom concentration, a longer initialization period is not needed. A specific study of the bottom concentrations or a more complex version of the module

considering different behaviors for the bottom layers would require the simulations to start earlier.

Time series of turbidity measurements (Villars and Vos, 1999) from stations S0 (Terneuzen) and S2 (Baalhoek) are used to calibrate the model in the area downstream of the main ETM. The model is then calibrated against SSC measurements from stations S3 (Buoy 87) to S17 (Wetteren) along the Belgian part of the Scheldt, to represent accurately the range of variation in this area, and to reproduce the location and the intensity of the ETMs. Finally, the model results are compared with those from the LTVmud model, a three-dimensional model described in van Kessel et al. (2011).

5.4.1 Variations at the tidal and spring/neap cycle scales

In order to isolate the variations of the SSC at the tidal and spring/neap cycle scales, the model is first calibrated for a spring/summer situation against turbidity measurements at stations S0 (Terneuzen) and S2 (Baalhoek). Because these fluctuations are following the tidal regime, they should be reproduced rather well only taking into account the hydrodynamics. A set of constant values for the three parameters M, τ_e and $w_{s,0}$ should therefore be found. However, it proved impossible to identify a single set of parameters to fit the time series of both stations at the same time. The optimal values are

$$\begin{aligned} M &= 2 \cdot 10^{-5}\,\mathrm{kg\,m^{-2}\,s^{-1}}, \\ \tau_e &= 0.2\,\mathrm{N\,m^{-2}}, \\ w_{s,0} &= 3 \cdot 10^{-3}\,\mathrm{m\,s^{-1}}, \end{aligned} \tag{5.10}$$

to fit the data from Terneuzen (not shown), and

$$\begin{aligned} M &= 2 \cdot 10^{-5}\,\mathrm{kg\,m^{-2}\,s^{-1}}, \\ \tau_e &= 0.2\,\mathrm{N\,m^{-2}}, \\ w_{s,0} &= 1.5 \cdot 10^{-3}\,\mathrm{m\,s^{-1}}, \end{aligned} \tag{5.11}$$

to fit those from Baalhoek (not shown). Even if only the optimal value of $w_{s,0}$ is different for both stations, using the optimal value of one station leads to rather poor results at the other station. In this form, the model is therefore too simple and at least one additional process or forcing should be taken into account, which would spatially modulate the value of $w_{s,0}$.

Fluctuations in flocculation influence the value of $w_{s,0}$. Besides SSC, salinity is another factor that influences the flocculation processes (Xia et al., 2004; Chen, 2009). While an increase of the SSC implies an increase of the number of collisions of suspended sediment particles per unit of time, the salinity increases their ability to aggregate (van Leussen, 1999; Mietta et al., 2009). Since salinity is higher around Terneuzen than around Baalhoek, this may suggest different values of the reference settling velocity for these two stations, or that $w_{s,0}$ is a function of the salinity S. As the goal is only to determine if the influence of salinity on the flocculation processes could improve the results, a simple linear parameterization is proposed:

$$w_{s,0} = w_{s,0}^{f}\left(\left(P_S - 1\right)\frac{S}{34} + 1\right). \tag{5.12}$$

The reference settling velocity $w_{s,0}$ is equal to its freshwater value $w_{s,0}^{f}$, multiplied by a factor increasing linearly from 1 in freshwater ($S = 0$) to $P_S > 1$ into the sea ($S = 34$). Comparing with the measurements of spring and summer 2000, the best results, both for Terneuzen and Baalhoek, are obtained with

$$\begin{aligned} M &= 2 \cdot 10^{-5}\,\mathrm{kg\,m^{-2}\,s^{-1}}, \\ \tau_e &= 0.2\,\mathrm{N\,m^{-2}}, \\ w_{s,0}^{f} &= 7 \cdot 10^{-4}\,\mathrm{m\,s^{-1}}, \\ P_S &= 5. \end{aligned} \tag{5.13}$$

It is important to mention here that this formulation leads to settling velocity values that are in rather good agreement with observations (Mietta et al., 2009; Manning et al., 2011). These results are displayed in Figures 5.2 and 5.3.

Figure 5.2 shows the variations at the tidal scale. The mean value and the range of variation are correct, but the fine scale variability present in the observations is not reproduced. However, these results obtained with a two-dimensional depth-averaged model are qualitatively comparable to those obtained with more complex three-dimensional models (e.g. van Kessel et al., 2011). Figure 5.3 displays the variations at the spring/neap cycle scale. The mean value and the range of variation are quite satisfactorily reproduced at this timescale.

Another possibility to account for the spatially varying reference settling velocity would be to take into account several types of sediments

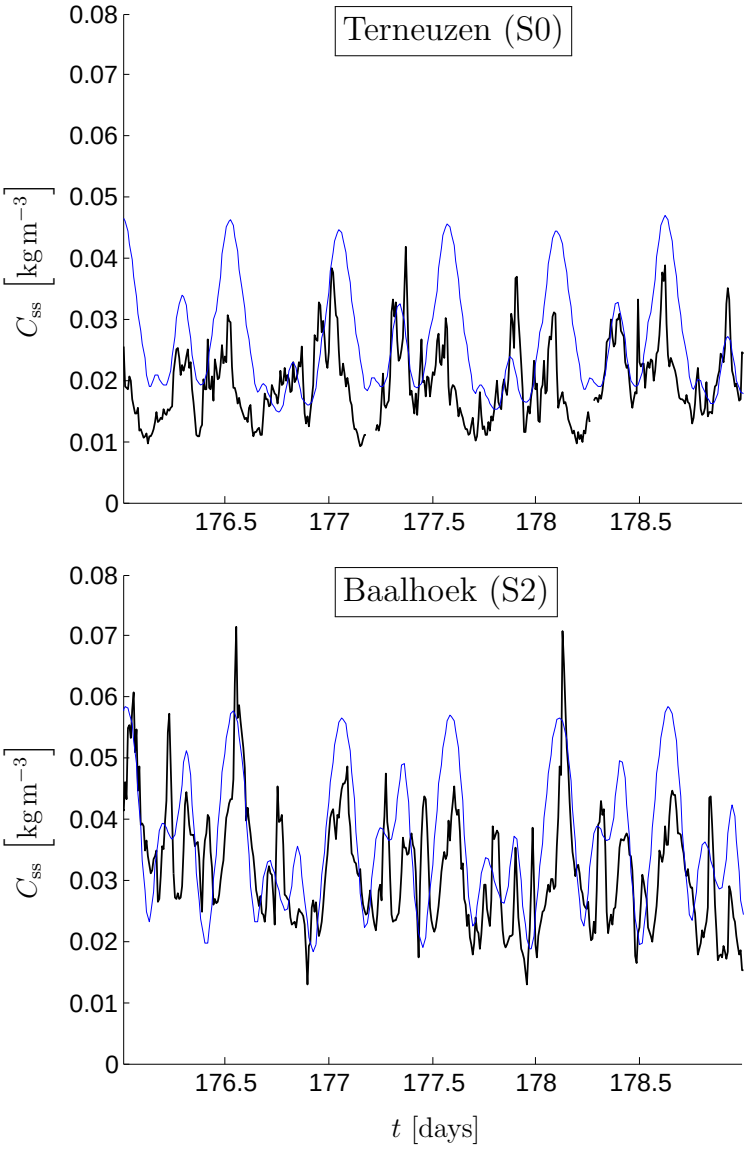

Figure 5.2: Depth-averaged SSC from 24 June 2000 until 27 June 2000; in black, data deduced from turbidity measurements at different depth levels of stations S0 (Terneuzen) and S2 (Baalhoek); in blue, model results at the same locations, using equations (5.9) and (5.12) for w_s and parameter set (5.13).

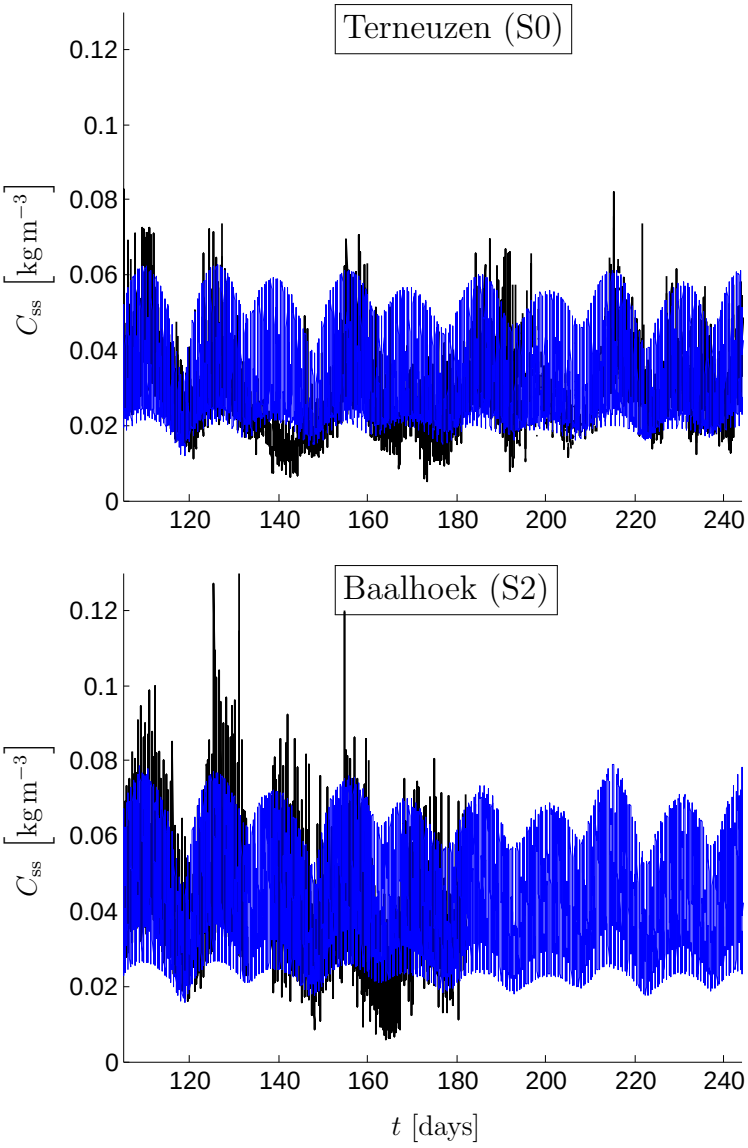

Figure 5.3: Depth-averaged SSC from 15 April 2000 until 1 September 2000; in black, data deduced from turbidity measurements at different depth levels of stations S0 (Terneuzen) and S2 (Baalhoek); in blue, model results at the same locations, using equations (5.9) and (5.12) for w_s and parameter set (5.13).

with different properties. The marine sediments (sand) are heavier than the riverine sediments (silt and clay) and their proportion is larger downstream (van der Wal et al., 2010). This could also explain why the settling velocity seems higher in Terneuzen than in Baalhoek. However, to limit the number of parameters and the computational cost, the approach chosen for the present article is restricted to one only type of sediments. Nevertheless, it would be interesting to compare the present results with those obtained with a future version of the module that would deal with several types of sediments.

5.4.2 Variations at the seasonal scale

The observed SSC is significantly higher in winter than in summer. This is not only observed around Terneuzen and Baalhoek (Figure 5.4), but also along the whole estuary (Fettweis et al., 1998; Chen et al., 2005b; van der Wal et al., 2010). The hydrodynamics exhibits no such variations, at least not in the areas of Terneuzen and Baalhoek: the tidal discharge in these regions is several hundreds of times higher than the river discharge. However, salinity does feature seasonal variations, depending on the river discharge, and, in the present module, salinity has an influence on the settling velocity. It is nevertheless not sufficient to represent the seasonal variations of the SSC (not shown). Therefore, once again, there is at least one more process or forcing to take into account.

A good candidate to explain this decrease of turbidity in summer is the increase of the biological activity. Indeed, organism activity generates a fluffy, interfacial layer on suspended particles that causes them to stick together when colliding (Wolanski, 1995). Therefore, an increase of organic content in summer implies an increase of floc size that is observed in situ (Mietta et al., 2009). This process is called bioflocculation (Manning et al., 2010) and it suggests that the settling velocity is higher in summer. Moreover, similar processes increase the cohesiveness of muddy bottom sediments in summer which become more difficult to erode (Stolzenbach et al., 1992). This process, called biostabilization (Manning et al., 2010), suggests that the bottom stress threshold value for erosion is also higher in summer (van der Wal et al., 2010).

Although the biological activity is not a variable of the present model and is moreover difficult to quantify, there is a strong correlation between

biological activity and water temperature, for which data are available[2]. In the new parameterizations proposed here, the reference settling velocity and the threshold value of the bottom stress for erosion are functions of the water temperature T. The reference settling velocity is equal to its summer value given by equation (5.12), multiplied by a factor decreasing linearly from 1 in summer ($T = T_\mathrm{s}$) to $P_T < 1$ in winter ($T = T_\mathrm{w}$):

$$w_{\mathrm{s},0} = w_{\mathrm{s},0}^{\mathrm{fs}}\left(\left(P_S - 1\right)\frac{S}{34} + 1\right)\left(\left(P_T - 1\right)\frac{T - T_\mathrm{s}}{T_\mathrm{w} - T_\mathrm{s}} + 1\right), \quad (5.14)$$

where $w_{\mathrm{s},0}^{\mathrm{fs}}$ is the summer freshwater value of the reference settling velocity $w_{\mathrm{s},0}$, and $T_\mathrm{s} = 20\,^\circ\mathrm{C}$ and $T_\mathrm{w} = 5\,^\circ\mathrm{C}$ are typical values of the Scheldt water temperature in summer and winter, respectively. The threshold value of the bottom stress for erosion is equal to its summer value $\tau_\mathrm{e}^\mathrm{s}$, multiplied by a factor decreasing linearly from 1 in summer ($T = T_\mathrm{s}$) to $Q_T < 1$ in winter ($T = T_\mathrm{w}$):

$$\tau_\mathrm{e} = \tau_\mathrm{e}^\mathrm{s}\left(\left(Q_T - 1\right)\frac{T - T_\mathrm{s}}{T_\mathrm{w} - T_\mathrm{s}} + 1\right), \quad (5.15)$$

After comparison with the measurements of the whole year 2000, the best results are obtained with

$$\begin{aligned} M &= 2 \cdot 10^{-5}\,\mathrm{kg\,m^{-2}\,s^{-1}}, \\ w_{\mathrm{s},0}^{\mathrm{fs}} &= 1 \cdot 10^{-3}\,\mathrm{m\,s^{-1}}, \\ P_S &= 5, \\ P_T &= 2/3, \\ \tau_\mathrm{e}^\mathrm{s} &= 0.2\,\mathrm{N\,m^{-2}}, \\ Q_T &= 1/3. \end{aligned} \quad (5.16)$$

These results are displayed in Figure 5.4.

First of all, it has to be mentioned that the new parameterizations (5.14) and (5.15) do not alter the quality of the results in summer, at the tidal and spring/neap cycle scales. Then, the range of variation is quite satisfactorily represented for the first half of 2000. It is less so for the end of the year, at least for Terneuzen since there are no data available for that period for Baalhoek. However, some external processes, such as dredging or shipping for example, are known to locally have a significant impact on the SSC (Chen et al., 2005b). For example,

[2]Hydro Meteo Centrum Zeeland, Middelburg, The Netherlands (`www.hmcz.nl`)

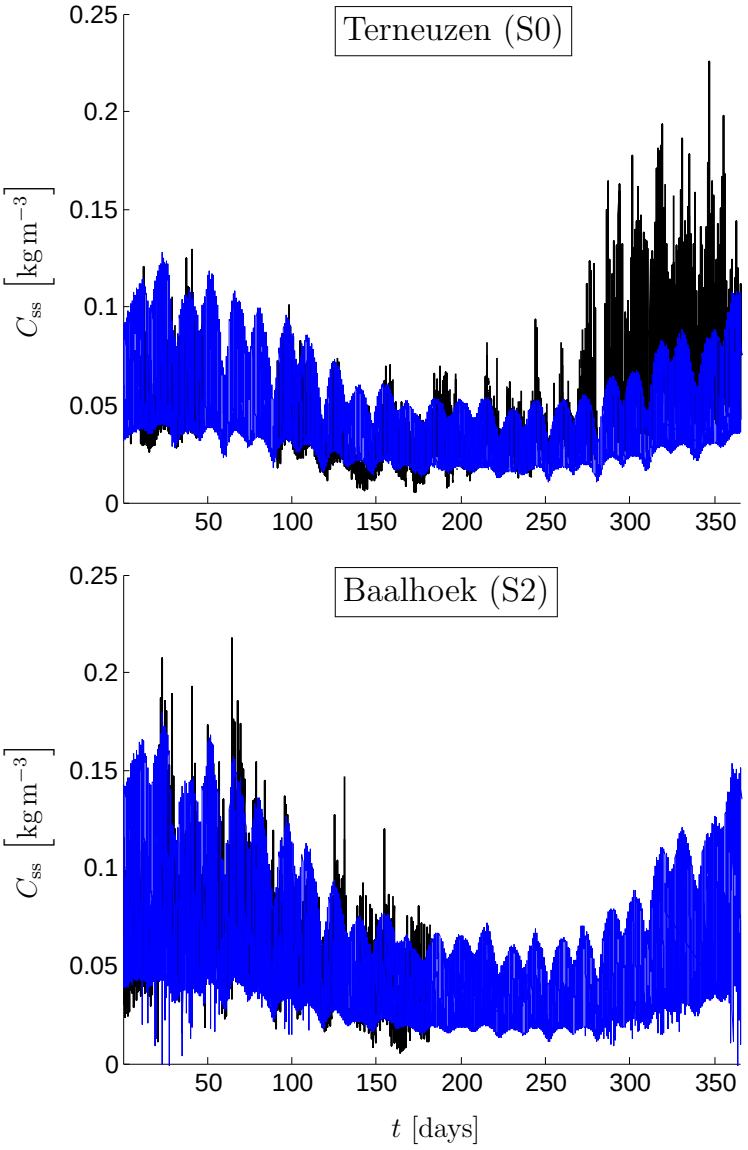

Figure 5.4: Depth-averaged SSC in 2000; in black, data deduced from turbidity measurements at different depth levels of stations S0 (Terneuzen) and S2 (Baalhoek); in blue, model results at the same locations, using equations (5.9) and (5.14) for w_s, equation (5.15) for τ_e and parameter set (5.16).

locally enhanced turbulence may influence the SSC by breaking the flocs and therefore affect the settling velocity (Chen, 2009). The cohesiveness of bottom sediments is probably also affected, which may change the erodibility. Finally, the dredging activities are probably contributing to resuspension events. However, due to a marked lack of available data, these important processes are very difficult, even impossible, to quantify and to incorporate into the model. On top of those dredging and shipping activities, the area of Terneuzen is moreover influenced by the inputs from the connexion with the Ghent-Terneuzen canal.

5.4.3 Variations at the seasonal scale for another period

Sections 5.4.1 and 5.4.2 described different calibration steps leading to a definition of the module that produces rather satisfactory results around Terneuzen and Baalhoek for the year 2000. The present section displays the results obtained with the same parameterizations and the same parameter values, but for the year 1999 (Figure 5.5). Those results may be claimed to be as satisfactory as those of 2000, even if the SSC variability is underestimated in the late spring in Baalhoek and strongly underestimated the whole summer in Terneuzen. These differences between the model outputs and the data must be explained by processes and forcings that are not taken into account in this model. Among them, the influence of important wind events, which may soften the bottom layer in shallow areas and therefore increase its erodibility, must probably be excluded. Indeed, no significant wind event is reported for this period (not shown). On the other hand, dredging events or shipping activities are still plausible explanations.

5.4.4 Longitudinal profile and ETMs

So far, the model is calibrated using data from two measurement stations located downstream of the main ETM. In this section, the aim is to assess the behavior of the model around and upstream of the main ETM. To this end, the results are first compared with monthly SSC measurements performed during the whole year 2002 along the Belgian part of the Scheldt Estuary and River. Unlike those used in the previous sections, which were deduced from turbidity measurements, the data presented here are direct measurements of SSC. The model results are then compared against depth-averaged outputs from the more complex three-dimensional LTVmud model (van Kessel et al., 2011) during

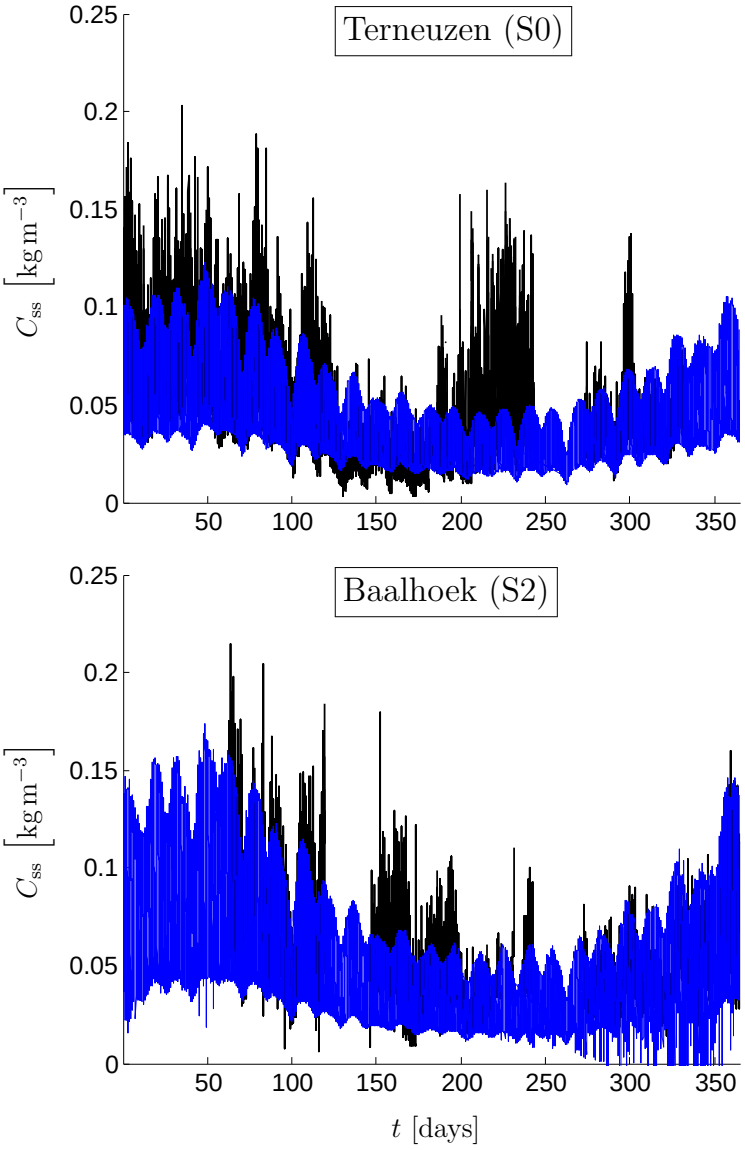

Figure 5.5: Depth-averaged SSC in 1999; in black, data deduced from turbidity measurements at different depth levels of stations S0 (Terneuzen) and S2 (Baalhoek); in blue, model results at the same locations, using equations (5.9) and (5.14) for w_s, equation (5.15) for τ_e and parameter set (5.16).

autumn 2006. In this section, the results are presented as a longitudinal profile, i.e. along a virtual line that follows the main channel of the estuary, from the mouth (km 0) to Ghent (km 160).

As it is defined so far, the model is more or less able to represent the location of the main ETM in the correct area. However, comparing with observations (Chen et al., 2005b; Arndt et al., 2007), the measurements of 2002 or the outputs from the LTVmud model, the SSC is largely underestimated around and upstream of the main ETM (not shown). A decrease of the settling velocity or the bottom stress threshold value for erosion is difficult to justify in these areas. On the other hand, an increase of the erosion velocity is more plausible. Indeed, the nature of bottom sediments is quite constant between the mouth and the Belgian/Dutch border, mainly made up of sand, but the proportion of finer sediments increases drastically upstream of it (van der Wal et al., 2010). This radical change in the bottom sediment type distribution is initiated around the downstream limit of the main ETM.

Since the present module only deals with fine sediments, it is normal that the erosion velocity M is higher in areas where the proportion of such sediments is higher. In the parameterization proposed here, M is equal to its downstream value M^{d} downstream km 50 (from the mouth), it is multiplied by a factor increasing linearly from 1 to $R_s > 1$ between km 50 and km 90, and it is equal to R_s further upstream:

$$M = \begin{cases} M^{\mathrm{d}} & \text{if } \; s \leq 50\,\mathrm{km}, \\ M^{\mathrm{d}}\left((R_s - 1)\dfrac{s - 50}{90 - 50} + 1 \right) & \text{if } \; 50\,\mathrm{km} \leq s \leq 90\,\mathrm{km}, \\ R_s M^{\mathrm{d}} & \text{if } s \geq 90\,\mathrm{km}, \end{cases} \tag{5.17}$$

where s is the upstream distance to the mouth (it is equal to 0 downstream). The best results are obtained with

$$\begin{aligned} M^{\mathrm{d}} &= 2 \cdot 10^{-5}\,\mathrm{kg\,m^{-2}\,s^{-1}}, \\ R_s &= 2, \\ w_{\mathrm{s},0}^{\mathrm{fs}} &= 1 \cdot 10^{-3}\,\mathrm{m\,s^{-1}}, \\ P_S &= 5, \\ P_T &= 2/3, \\ \tau_{\mathrm{e}}^{\mathrm{s}} &= 0.2\,\mathrm{N\,m^{-2}}, \\ Q_T &= 1/3. \end{aligned} \tag{5.18}$$

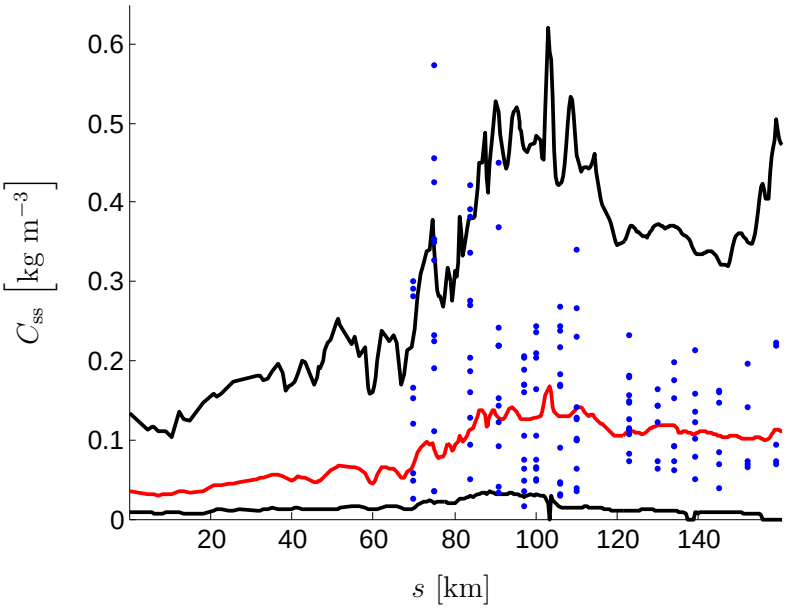

Figure 5.6: Longitudinal profile of mean (red), maximum and minimum (black) SSC during year 2002, from the mouth (km 0) to Ghent (km 160); model results obtained using equations (5.9) and (5.14) for w_s, equation (5.15) for τ_e, equation (5.17) for M and parameter set (5.18); in blue, monthly SSC measurements.

It must be underscored that this new parameterization does not influence much the dynamics downstream of the Belgian/Dutch border, so that the quality of the previous results is not altered (not shown).

In Figure 5.6, the new model results are presented for year 2002, against the measurement data sampled at that period. Looking at the mean and maximum values of the SSC, the main ETM is now clearly apparent (approximately from km 70 to km 120) and its intensity is in accordance with most observations (Chen et al., 2005b; Arndt et al., 2007). Moreover, the range is well reproduced almost all along the estuary, as only a few data are found outside the range of the model values. This attests to the good performance of the model to represent the sediment dynamics in the Scheldt Estuary and River.

In Figure 5.7 the model results are compared with the outputs of the LTVmud model during autumn 2006. The main ETM is also clearly

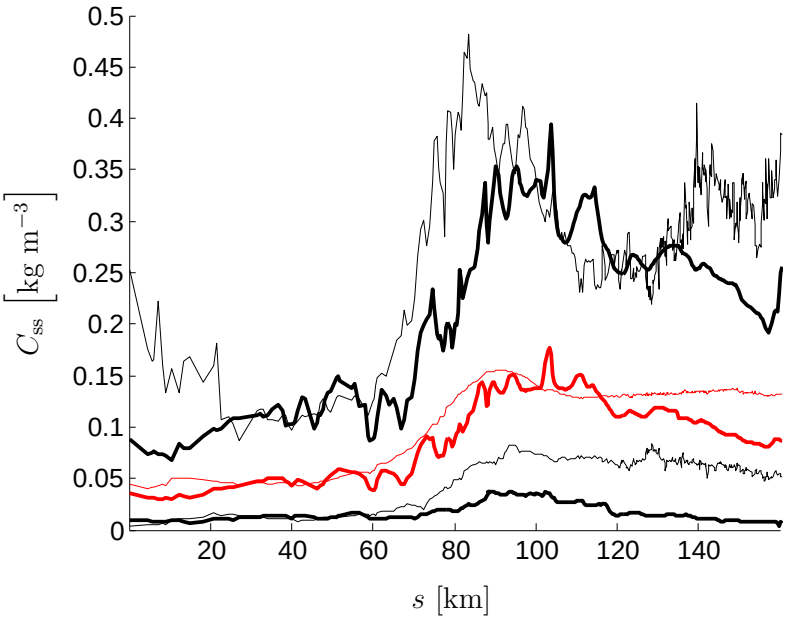

Figure 5.7: Longitudinal profile of mean (red), maximum and minimum (black) SSC between October 1, 2006 and December 31, 2006, from the mouth (km 0) to Ghent (km 160); thick lines are model results obtained using equations (5.9) and (5.14) for w_s, equation (5.15) for τ_e, equation (5.17) for M and parameter set (5.18); thin lines are results from the three-dimensional LTVmud model.

apparent in the mean and maximum SSC values from both models, although the LTVmud model locates it a little more downstream. In the river part, the models have more different behaviors. The LTVmud model maximum values are almost as high in the river ETM as in the main ETM. But still, even if the model of this article does not feature a clear local maximum, either the maximum or the mean values of the SSC are higher in the river part than downstream of the main ETM. This can be identified as the river ETM. Finally, using a depth-averaged model, suspended sediments instantaneously settle to the bottom. This could explain the lower minimum values of the SSC. Anyway, the consistency of the results from both models is remarkable.

As it is located downstream of the mouth, the third ETM is not visible on Figure 5.7. The snapshot of SSC presented on Figure 5.8

shows the existence of a small ETM in front of the mouth, but SSC is clearly underestimated there. This may be due to the fact that the bottom of this region is mainly made up of sand, while the only type of sediments considered here are fine sediments. In addition, the waves play an important role in the formation of this third ETM (Chen and Wartel, 2009) and this marine process is not taken into account in the present module. Indeed, the domain of interest is the estuary, and the wave influence is limited to only a few kilometers upstream of the mouth (Chen and Wartel, 2009).

Figure 5.9 presents the snapshot of the simulated bottom sediment concentration at the same moment. An accumulation of bottom sediments is observed in the area of the marine ETM. Therefore, it could be expected that a more sophisticated parameterization of the erosion velocity M, which would take into account the influence of the waves (e.g. Lambrechts et al., 2010), would lead to better results in this area. However, as the goal is to keep the module as simple as possible, and because this marine ETM is not inside the domain of main interest, M is not further modified.

5.5 Conclusion

The objective of this study was to design a sediment module for the two-dimensional depth-averaged and one-dimensional section-averaged components of SLIM, in order to represent satisfactorily the main features of the SSC dynamics in the Scheldt Estuary and tidal river network. The initial idea was to develop a module as simple as possible, with only three parameters: M the erosion velocity, τ_e the bottom stress threshold value for erosion, and w_s the settling velocity. However, to be able to represent accurately the variations of the SSC at timescales ranging from hours to a year at two locations in the estuary, improved parameterizations proved to be necessary.

The settling velocity is influenced by flocculation processes. The SSC, the salinity and the biological activity are important factors governing the flocculation processes and they are used in the parameterization of w_s. The biological activity also has an impact on the erodibility of the bottom sediments and is of use in the parameterization of τ_e.

With these improvements, the model produces an ETM in the area of Antwerp, but its intensity is too small and the river ETM is not present. To improve the model to represent more accurately those two ETMs,

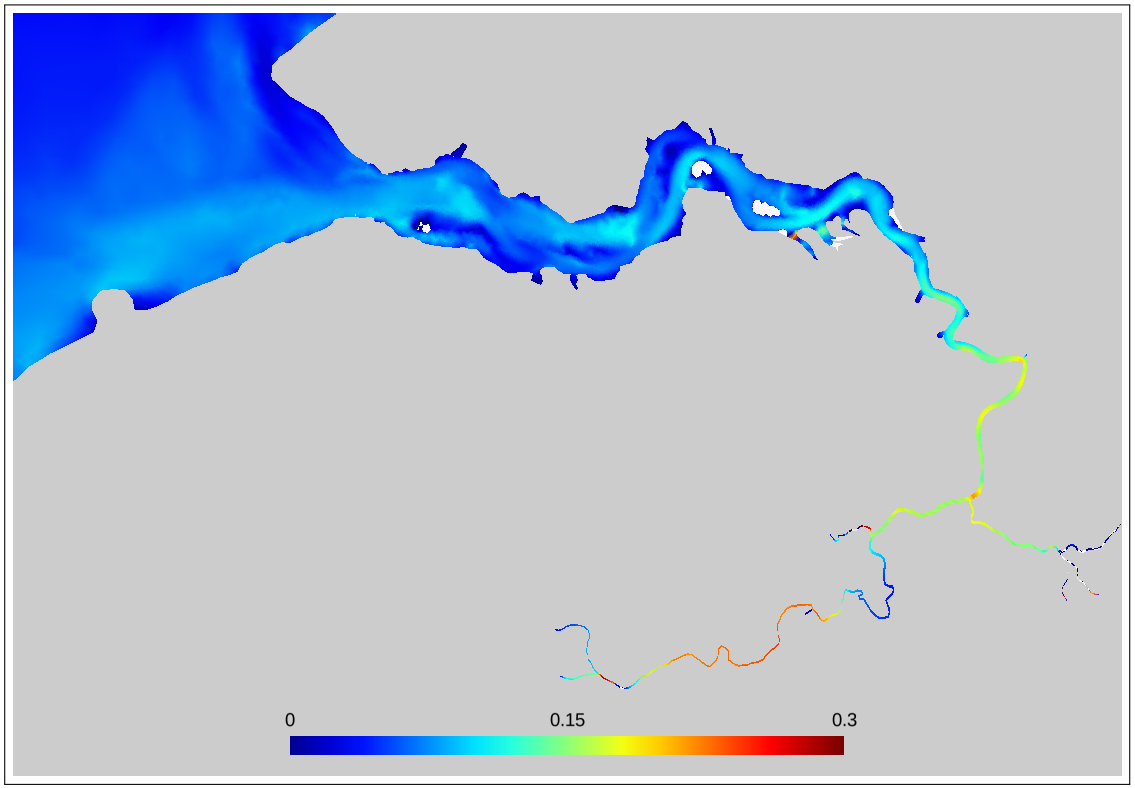

Figure 5.8: SSC snapshot at rising tide (January 15, 2000); dry areas are represented in white; results obtained using equations (5.9) and (5.14) for w_s, equation (5.15) for τ_e, equation (5.17) for M and parameter set (5.18).

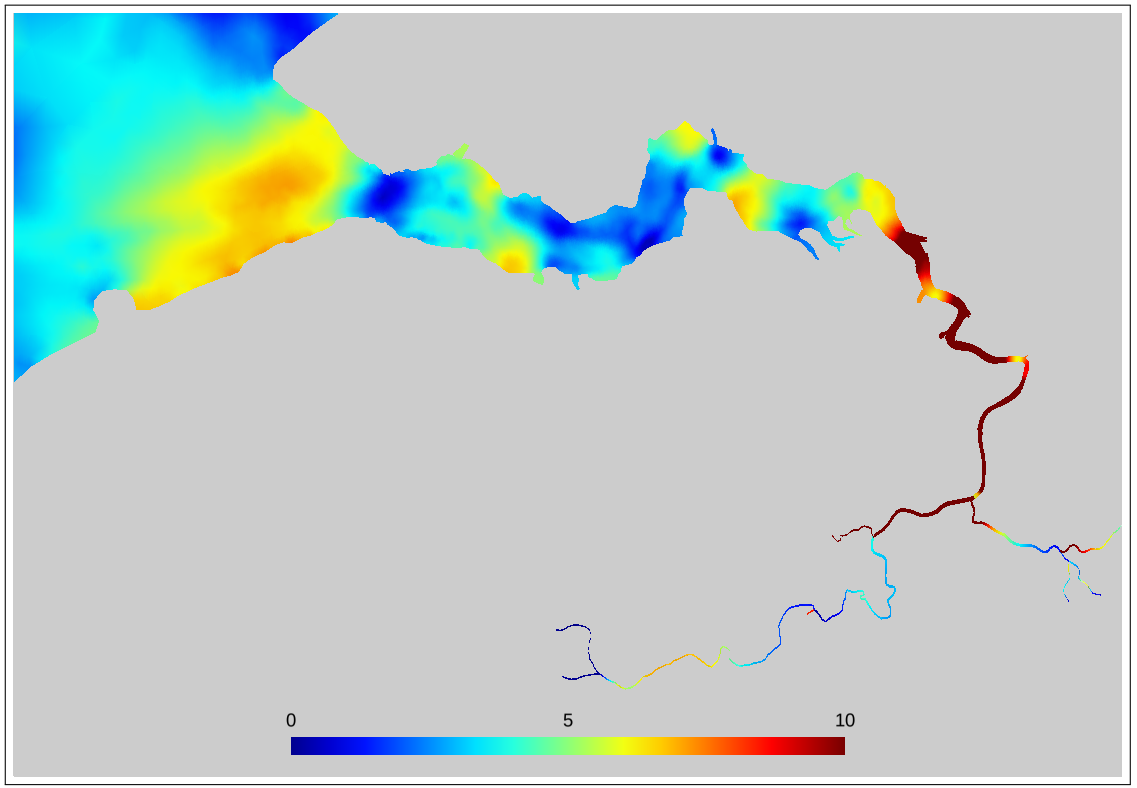

Figure 5.9: Bottom sediment concentration snapshot at rising tide (January 15, 2000); results obtained using equations (5.9) and (5.14) for w_{s}, equation (5.15) for τ_{e}, equation (5.17) for M and parameter set (5.18).

the parameterization of M is enriched in order to take into account the bottom composition changes.

This strategy allowed to identify what seems to be some of the key processes governing the sediment dynamics in the Scheldt Estuary. Moreover, this depth-averaged two-dimensional sediment model, with only one type of sediments, proved to be able to represent rather satisfactorily the main features of the SSC dynamics in the Scheldt Estuary and tidal river, which is an important result by itself.

Chapter 6

Conclusions and perspectives

This research work was conducted under the auspices of two important projects. As a member of the SLIM project, I contributed to the development of a new finite element marine model, especially its two-dimensional depth-averaged component. Some members of the team, including me, are also involved in the TIMOTHY network, where our role is to develop environmental applications of this finite element model for the Scheldt Estuary. The general thread of the present work is formed by the different stages to obtain a finite element sediment model of the Scheldt Estuary, in order to make possible such environmental studies.

The main reason for the choice of a two-dimensional depth-averaged model (combined with a one-dimensional section-averaged model upstream of Antwerp) is that the three-dimensional component is not yet available for such realistic applications. As a result, the effects of the baroclinic pressure gradient, and therefore the water density variations, are removed from the system (Section 2.2). In the Scheldt Estuary, the consequences are not overly important. Indeed, the flow is vertically well-mixed and the horizontal variations are rather small. This is illustrated with the good agreement between our results and those from the three-dimensional LTVmud model in modeling the sediment dynamics of the Scheldt (Section 5.4.4). However, stratification may be

important in the vicinity of the main maximum of turbidity (around Antwerp) and in the coastal zone, downstream of the mouth. If we want to study more specifically the dynamics of those regions, a three-dimensional model is probably mandatory. Nevertheless, the smaller computational cost of two-dimensional models will always remain a crucial advantage when considering long-term environmental studies, justifying the developments carried out in the framework of the present thesis.

The construction of the hydrodynamic module was an important team work (de Brye et al., 2010; Kärnä et al., 2011a). My main contribution in this task is the development of the flux-limiting wetting-drying method (Gourgue et al., 2009). This method proved very promising but has the drawback to be limited to explicit time integration methods. Indeed, the version of SLIM used in this doctoral dissertation is not sufficiently efficient to deal with the small time steps required by such methods. The simulations would last too long. That is why the modified bathymetry method is used for the simulations of this work, although this method features some physical limitations. However, the next version of SLIM, which is still under development at the time of writing this conclusion, is built with the ambition to increase the computational efficiency. In that case, the flux-limiting method could become an attractive solution for this new version. Moreover, only explicit schemes benefit from large parallel computing that are necessary when considering three-dimensional simulations of real applications. The wetting-drying method for the three-dimensional component of SLIM could therefore be based on the flux-limiting method.

The construction of the transport tracer module was another important team work. Together with the hydrodynamic module, it allowed to start some basic environmental applications, such as the estimation of timescales (Blaise et al., 2010b; de Brauwere et al., 2011a; de Brye et al., 2011a) or the study of fecal bacteria pollution (de Brauwere et al., 2009, 2011b). However, in order to perform more sophisticated environmental studies, a sediment module was needed. The development of the first version of this module is the second important contribution of this thesis, and probably the most important (Gourgue et al., 2011a). In addition to being part of a two-dimensional depth-averaged model, this first version is based on very simple parameterizations, involving only one type of sediments. Its computational cost remains therefore relatively low. When applied to the Scheldt Estuary and tidal rivers, and despite its relative simplicity, this sediment module produces results that compare

rather satisfactorily with available measurement data and outputs from a more sophisticated three-dimensional model. The good behavior of the model is an important result by itself. Moreover, among other things, this study also emphasized the important role that biological activity plays on sediment dynamics.

If we want to study in more details the sediment dynamics of the Scheldt Estuary with SLIM, a more sophisticated version of the sediment module is probably needed. This second version should probably involve different types of sediments, according to their size. The properties of large sediments (sand) and finer sediments (silt and clay) are indeed very different. And the spatial heterogeneity of the sediment size distribution is probably a better explanation to the spatial heterogeneity of the sediment properties than the parameterizations proposed in Chapter 5. On the other side, if we want to use the sediment concentrations as state variables for new environmental studies, the first version of the module is probably sufficient. A module with only one type of sediments has the advantage to be a cheap solution, and the results presented in Chapter 5 nevertheless cover the main features of the sediment dynamics of the Scheldt.

The development of a second version of the fecal bacteria module (de Brauwere et al., 2011c) constitutes the first environmental study involving the computing of sediment concentrations in the Scheldt using SLIM. In the first version of the fecal bacteria module, an arbitrary part of the bacteria was removed of the domain, supposedly due to sedimentation. Although very rough, this parameterization produces rather good results in the riverine part (de Brauwere et al., 2011b), but less in the area of the main estuarine turbidity maximum. This research study has been launched in parallel of the development of the sediment module, but is not ended yet. Nevertheless, we hope that an explicit treatment of the sediment processes will improve the model behavior in an area where they are of crucial importance.

The development of the biogeochemical module of SLIM is another ongoing project. At present, the number of variables is still not determined. The suspended sediment concentration could either be a model proxy in order to estimate the luminosity in the water column, or be a real variable of the module with strong interactions with the other ones. In the second case, it could be very interesting to study further the influence of biological activity on the sediment dynamics.

Finally, we aim to model the trace metal pollution in the Scheldt Estuary. The trace metal module is mainly based on the concept of the

partition coefficient K_{D}, which is the ratio between trace metal particles adsorbed on suspended sediments and trace metal particles dissolved in the water column. The first interest in modeling trace metal dynamics will be to calibrate the existing formulations of K_{D}, mostly functions of salinity and sometimes of the suspended sediment concentration. The second interest will be to study further the dynamics inside the Estuary. Hopefully, this project will constitute my main subject of research in the close future. An introduction to this work is proposed in the next section.

As we can see, even if this thesis is an achievement by itself, it is also an introduction to more challenging environmental studies in which I look forward to taking part...

Perspectives: a trace metal model

This final section aims to show the type of problems that can be addressed now that the objectives of this thesis have been achieved. It is illustrated by the case of the trace metal dynamics.

Trace metal particles exist in two different forms in the water column: either dissolved in the water column (the dissolved phase) or adsorbed on suspended sediments (the adsorbed phase). Particles can pass from a phase to the other according to physico-chemical adsorption/desorption processes. The adsorbed phase is naturally subject to sedimentation processes, so that adsorbed trace metal may also be found in the bottom layer. There exist two simple approaches to model the trace metal transport in aquatic systems.

The first one is called here the A-approach and is schematically presented in Figure 6.1. The variables are C_{md}, the depth-averaged concentration of dissolved trace metal in the water column [$\mathrm{kg\,m^{-3}}$], C_{ma}, the depth-averaged concentration of adsorbed trace metal in the water column [$\mathrm{kg\,kg^{-1}}$][1], and C_{mb}, the concentration of trace metal adsorbed in the fresh layer [$\mathrm{kg\,kg^{-1}}$]. The concentration of trace metal adsorbed in the parent layer C_{mp} is only an input of the model.

The concentration of trace metal dissolved in the water column can be considered as a simple active tracer that is transported as salinity is in equation (4.17), with an additional reactive term to take into account

[1] kg of trace metal per kg of sediments

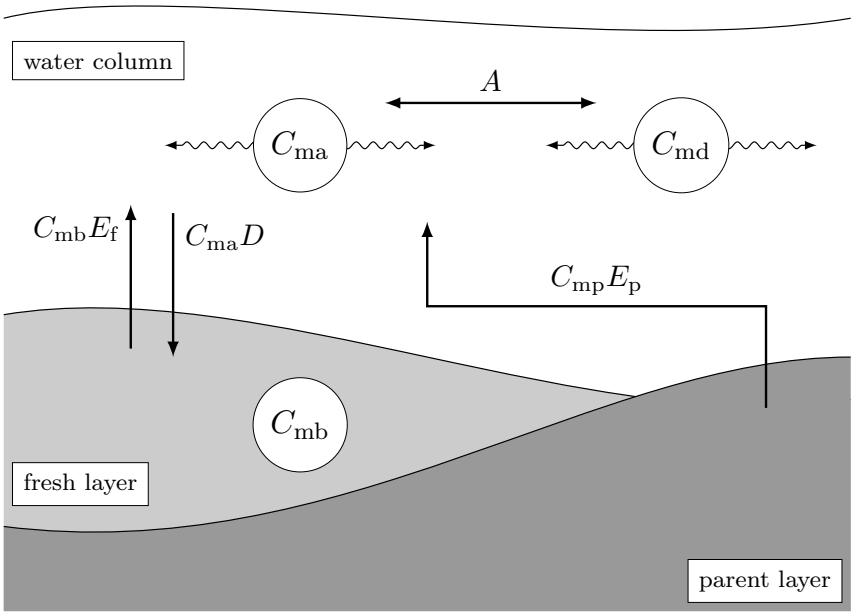

Figure 6.1: Schematic representation of the A-approach to model trace metal transport; C_{md} is the depth-averaged concentration of dissolved trace metal in the water column, C_{ma} is the depth-averaged concentration of adsorbed trace metal in the water column, C_{mb} is the concentration of trace metal adsorbed in the fresh layer, and C_{mp} is the concentration of trace metal adsorbed in the parent layer; A is the adsorption rate of trace metal; E_f is the erosion rate of sediments from the fresh layer, E_p is the erosion rate of sediments from the parent layer, and D is the deposition rate of sediments on the fresh layer.

the trace metal flux between the dissolved and adsorbed phases:

$$\frac{\partial}{\partial t}(HC_{\mathrm{md}}) + \boldsymbol{\nabla} \cdot (H\boldsymbol{u}C_{\mathrm{md}}) = \boldsymbol{\nabla} \cdot (H\kappa\boldsymbol{\nabla}C_{\mathrm{md}}) - A, \tag{6.1}$$

where A is the adsorption rate of trace metal. It is positive when trace metal adsorbs on suspended sediments and negative when it desorbs from them. Since the trace metal adsorbed on suspended sediments is transported according to the sediment dynamics and not according to the flow, the variable that is advected and dispersed as a simple active tracer is not C_{ma}, but the product $(C_{\mathrm{ss}}C_{\mathrm{ma}})$. Additional terms take into account the erosion and deposition processes, and the trace metal flux between the dissolved and adsorbed phases:

$$\begin{aligned}\frac{\partial}{\partial t}(HC_{\mathrm{ss}}C_{\mathrm{ma}}) + \boldsymbol{\nabla} \cdot (H\boldsymbol{u}C_{\mathrm{ss}}C_{\mathrm{ma}}) = \boldsymbol{\nabla} \cdot \big(H\kappa\boldsymbol{\nabla}(C_{\mathrm{ss}}C_{\mathrm{ma}})\big) \\ + A + C_{\mathrm{mb}}E_{\mathrm{f}} + C_{\mathrm{mp}}E_{\mathrm{p}} - C_{\mathrm{ma}}D.\end{aligned} \tag{6.2}$$

The bottom trace metal is not transported horizontally and only exchange of adsorbed trace metal with the water column, through erosion and deposition of contaminated sediments, allows to evolve its concentration:

$$\frac{\partial}{\partial t}(C_{\mathrm{sb}}C_{\mathrm{mb}}) = C_{\mathrm{ma}}D - C_{\mathrm{mb}}E_{\mathrm{f}}. \tag{6.3}$$

The main problem of the A-approach to model the trace metal transport is that the adsorption rate A appearing in equations (6.1) and (6.2) is very difficult to evaluate and virtually impossible to parameterize. However, a few manipulations allow to circumvent this problem (De Smedt et al., 1998; Wu et al., 2005), leading to the equations of the K_{D}-approach, which is schematically presented in Figure 6.2.

A new variable is defined, C_{ms}, which is the depth-averaged total concentration of trace metal in suspension in the water column:

$$C_{\mathrm{ms}} = C_{\mathrm{md}} + C_{\mathrm{ss}}C_{\mathrm{ma}}. \tag{6.4}$$

To differentiate the dissolved and adsorbed trace metal phases in suspension, the partition coefficient K_{D} is introduced:

$$K_{\mathrm{D}} = \frac{C_{\mathrm{ma}}}{C_{\mathrm{md}}}. \tag{6.5}$$

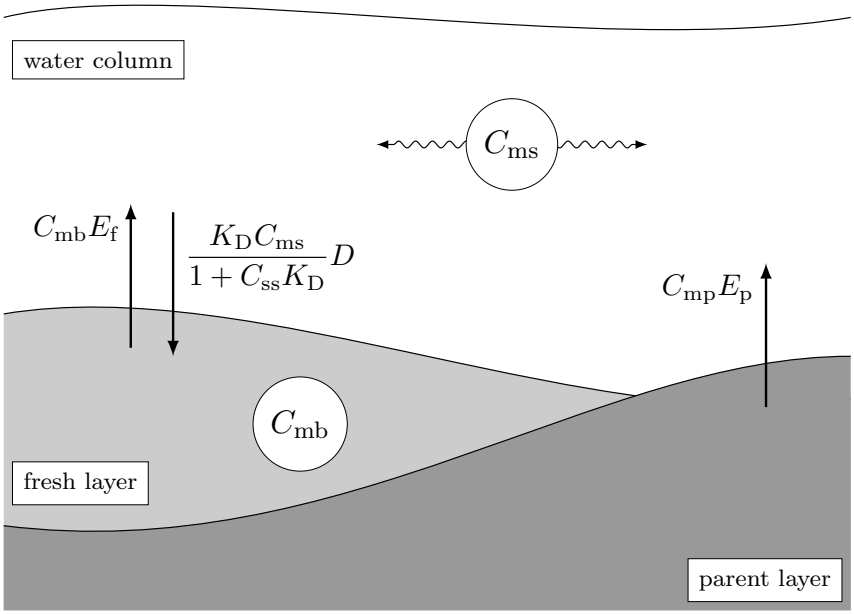

Figure 6.2: Schematic representation of the K_{D}-approach to model trace metal transport; C_{ms} is the depth-averaged total concentration of trace metal in suspension in the water column, C_{mb} is the concentration of trace metal adsorbed in the fresh layer, and C_{mp} is the concentration of trace metal adsorbed in the parent layer; K_{D} is the partition coefficient; C_{ss} is the concentration of suspended sediments, E_{f} is the erosion rate of sediments from the fresh layer, E_{p} is the erosion rate of sediments from the parent layer, and D is the deposition rate of sediments on the fresh layer.

Adding equation (6.1) to equation (6.2) allows to eliminate the adsorption rate A:

$$\frac{\partial}{\partial t}(HC_{\mathrm{ms}}) + \boldsymbol{\nabla}\cdot(H\boldsymbol{u}C_{\mathrm{ms}}) = \boldsymbol{\nabla}\cdot(H\kappa\boldsymbol{\nabla}C_{\mathrm{ms}}) + C_{\mathrm{mb}}E_{\mathrm{f}} + C_{\mathrm{mp}}E_{\mathrm{p}} - C_{\mathrm{ma}}D. \quad (6.6)$$

Moreover, the concentrations of the dissolved and adsorbed phases may be expressed exclusively in terms of C_{ss} and K_{D} using equations (6.4)

and (6.5):

$$C_{\mathrm{md}} = \frac{C_{\mathrm{ms}}}{1 + K_{\mathrm{D}} C_{\mathrm{ss}}}, \tag{6.7}$$

$$C_{\mathrm{ma}} = \frac{K_{\mathrm{D}} C_{\mathrm{ms}}}{1 + K_{\mathrm{D}} C_{\mathrm{ss}}}. \tag{6.8}$$

Incorporating these relations into equations (6.6) and (6.3) leads to the governing equations of the trace metal module:

$$\frac{\partial}{\partial t}(H C_{\mathrm{ms}}) + \boldsymbol{\nabla} \cdot (H \boldsymbol{u} C_{\mathrm{ms}}) = \boldsymbol{\nabla} \cdot (H \kappa \boldsymbol{\nabla} C_{\mathrm{ms}}) + C_{\mathrm{mb}} E_{\mathrm{f}} + C_{\mathrm{mp}} E_{\mathrm{p}} - \frac{K_{\mathrm{D}} C_{\mathrm{ms}}}{1 + C_{\mathrm{ss}} K_{\mathrm{D}}} D, \tag{6.9}$$

$$\frac{\partial}{\partial t}(C_{\mathrm{sb}} C_{\mathrm{mb}}) = \frac{K_{\mathrm{D}} C_{\mathrm{ms}}}{1 + C_{\mathrm{ss}} K_{\mathrm{D}}} D - C_{\mathrm{mb}} E_{\mathrm{f}}, \tag{6.10}$$

where the partition coefficient K_{D} must be parameterized. The drawback of the K_{D}-approach is that it considers instantaneous equilibrium between dissolved and adsorbed phases. However, unlike the adsorption rate A, it is possible to define rather good parameterizations of K_{D}. Therefore, at present, the K_{D}-approach is the only one that is acceptable. Several parameterizations of K_{D} have already been proposed, as function of the salinity (Wu et al., 2005), the SSC (Mwanuzi and De Smedt, 1999), or both of them. Our model will allow to compare these parameterizations and to calibrate them for the Scheldt Estuary.

A preliminary simulation of Cu (copper) has been performed using the parameterization proposed by Mwanuzi and De Smedt (1999):

$$K_{\mathrm{D}} = K_{\mathrm{D},0} \left(\frac{C_{\mathrm{ss}}}{C_{\mathrm{ss},0}} \right)^{b}, \tag{6.11}$$

with

$$K_{\mathrm{D},0} = 10^{7.515}\,\mathrm{m^3\,kg^{-1}}, \tag{6.12}$$

$$b = -0.749. \tag{6.13}$$

In the Scheldt, the major sources of Cu are the antifouling products of ships and the waste water treatment plants. However, in this very first

simulation, as the research data has not started yet, the only source of Cu that is considered is the parent layer, where a concentration of $10^{-5}\,\mathrm{kg\,kg^{-1}}$ is imposed. This value is based on concentrations in the adsorbed phase measured by Baeyens et al. (1998a) during the period 1981-1983. The first results are presented on Figure 6.3.

Of course, no interpretation can be drawn from this first simulation. The only objective was to illustrate the introduction to this future project based on the results of my doctoral research.

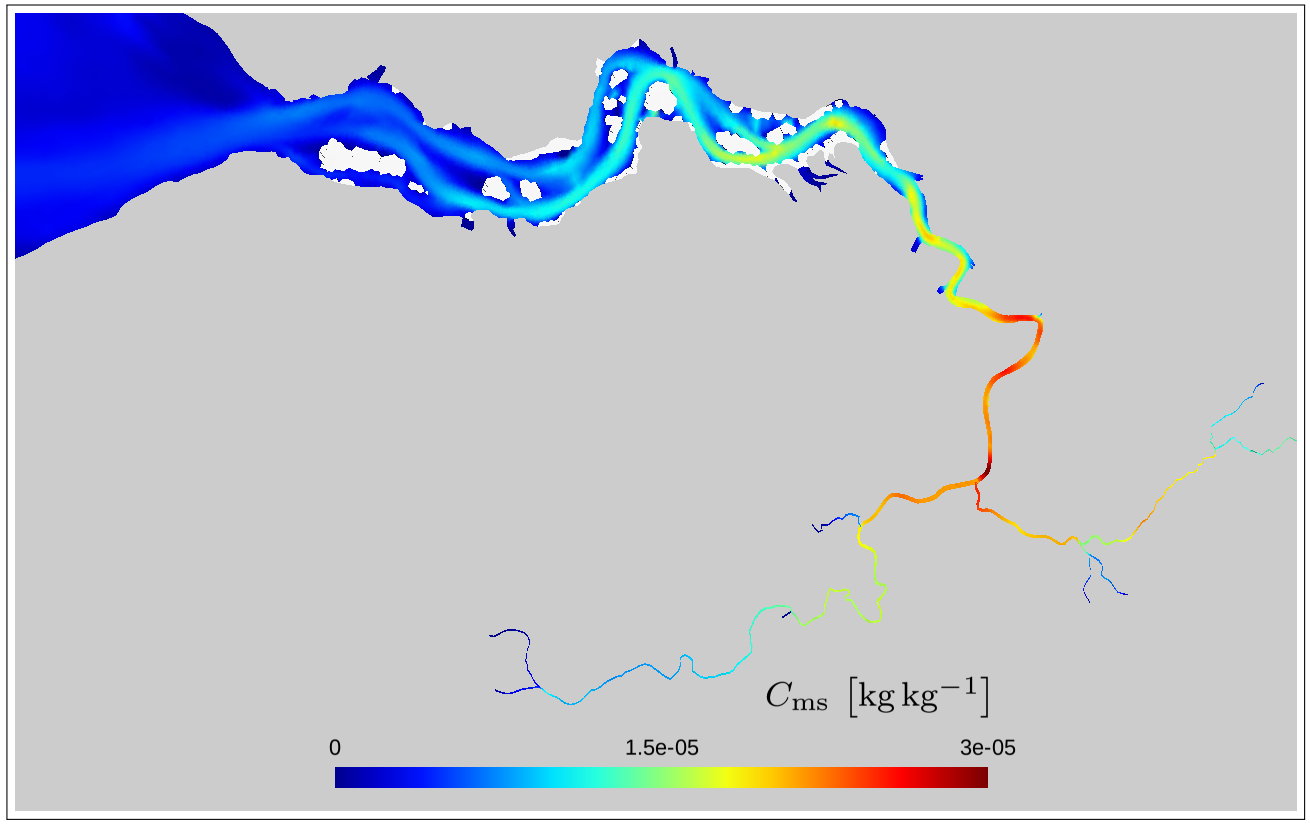

Figure 6.3: Snapshot from a first simulation of trace metal dynamics.

Appendix A

Analytical expressions in wetting-drying test cases

First Balzano test case

In the first Balzano test case, the bathymetry h is defined as follows:

$$h = x/2760 \qquad \forall x, \tag{A.1}$$

where x is the coordinate in the main direction of the basin.

Second Balzano test case

In the second Balzano test case, the bathymetry h is defined as follows:

$$h = \begin{cases} x/2760 & \text{if } x \leq 3600 \text{ m} \\ 30/23 & \text{if } 3600 \text{ m } \leq x \leq 4800 \text{ m} \\ x/1380 & \text{if } 4800 \text{ m } \leq x \leq 6000 \text{ m} \\ x/2760 & \text{if } x \geq 6000 \text{ m}, \end{cases} \tag{A.2}$$

where x is the coordinate in the main direction of the basin.

Third Balzano test case

In the third Balzano test case, the bathymetry h is defined as follows:

$$h = \begin{cases} x/2760 & \text{if } x \leq 3600 \text{ m} \\ -x/2760 + 60/23 & \text{if } 3600 \text{ m} \leq x \leq 4800 \text{ m} \\ x/920 - 100/23 & \text{if } 4800 \text{ m} \leq x \leq 6000 \text{ m} \\ x/2760 & \text{if } x \geq 6000 \text{ m}, \end{cases} \tag{A.3}$$

where x is the coordinate in the main direction of the basin.

Thacker test case

In the Thacker test case, the bathymetry h is defined as follows:

$$\frac{h}{h_0} = \frac{R^2 - r^2}{R^2}, \tag{A.4}$$

where h_0 is the water depth in the center of the basin at rest, R is the basin radius at rest, and r is the local distance to the center of the basin. If the problem dealed with is non dissipative, the elevation of the free surface η is described by the following expression:

$$\frac{\eta}{h_0} = \frac{\sqrt{1 - A^2}}{1 - A\cos(\omega t)} - 1 - \frac{r^2}{R^2}\left(\frac{1 - A^2}{\left(1 - A\cos(\omega t)\right)^2} - 1\right), \tag{A.5}$$

with

$$A = \frac{(h_0 + \eta_0)^2 - h_0^2}{(h_0 + \eta_0)^2 + h_0^2}, \tag{A.6}$$

$$\omega^2 = \frac{8gh_0}{R^2}, \tag{A.7}$$

where η_0 is the initial elevation of the free surface in the center. The parameters are chosen to obtain a period of oscillations equal to 12 h:

$$\begin{aligned} R &= 430.694 \text{ km}, \\ h_0 &= 50 \text{ m}, \\ \eta_0 &= 2 \text{ m}. \end{aligned}$$

Appendix B

One-dimensional section-averaged primitive equations

The equations governing the one-dimensional component of the model are:

$$\frac{\partial A}{\partial t} + \frac{\partial}{\partial x}(Au) = 0, \tag{B.1}$$

$$\frac{\partial u}{\partial t} + u\frac{\partial u}{\partial x} + g\frac{\partial \eta}{\partial x} = \frac{1}{A}\frac{\partial}{\partial x}\left(A\nu\frac{\partial u}{\partial x}\right) - \frac{\tau_\mathrm{b}}{\rho H}, \tag{B.2}$$

$$\frac{\partial (AS)}{\partial t} + \frac{\partial}{\partial x}(AuS) = \frac{\partial}{\partial x}\left(A\kappa\frac{\partial S}{\partial x}\right), \tag{B.3}$$

$$\frac{\partial (AC_\mathrm{ss})}{\partial t} + \frac{\partial}{\partial x}(AuC_\mathrm{ss}) = \frac{\partial}{\partial x}\left(A\kappa\frac{\partial C_\mathrm{ss}}{\partial x}\right) + b(E_\mathrm{p} + E_\mathrm{f} - D), \tag{B.4}$$

$$\frac{\partial (bC_\mathrm{sb})}{\partial t} = b(D - E_\mathrm{f}), \tag{B.5}$$

where t is still the elapsed time and x is the longitudinal coordinate. The variable of the continuity equation (B.1) is the cross-section area A [m^2]. The variable of the momentum conservation equation (B.2) is the section-averaged longitudinal velocity [$\mathrm{m\,s}^{-1}$], and the effective water

depth is computed as follows

$$H = \frac{A}{b}, \tag{B.6}$$

where b [m] is the river width:

$$b = \frac{\partial A}{\partial \eta}. \tag{B.7}$$

River widths and sections data for different values of the local elevation are given as topological inputs of the model (de Brye et al., 2010). The variables of the tracer equations (B.3) to (B.5) are the same as in the two-dimensional model, except that they are here averaged over the section (S and C_{ss}) and the bottom width (C_{sb}). The parametrizations are exactly the same.

The equations (B.1) to (B.5) are solved using SLIM and using a discontinuous Galerkin discretization with linear shape functions for every variable. The temporal integration is performed the same way as in the two-dimensional component and the vertical exchange processes of the sediment equations are also solved as pointwise ordinary differential equations.

Bibliography

Abbot, M. B. and Price, W. A., editors (1994). *Coastal, Estuarial and harbour engineers' reference book*. E & FN Spon.

Abualtayef, M., Kuroiwa, M., Tanaka, K., Matsubara, Y., and Nakahira, J. (2008). Three-dimensional hydrostatic modeling of a bay coastal area. *Journal of Marine Science and Technology*, 13:40–49.

Aizinger, V. and Dawson, C. (2002). A discontinuous Galerkin method for two-dimensional flow and transport in shallow water. *Advances in Water Resources*, 25:67–84.

Aizinger, V. and Dawson, C. (2007). The local discontinuous Galerkin method for three-dimensional shallow water flow. *Computer Methods in Applied Mechanics and Engineering*, 196:734–746.

Amante, C. and Eakins, B. W. (2008). ETOPO1 1 arc-minute global relief model: Procedures, data sources and analysis. Technical report, National Geophysical Data Center, NESDIS, NOAA, US Department of Commerce, Boulder, CO.

Arndt, S., Regnier, P., and Vanderborght, J.-P. (2009). Seasonally-resolved nutrient export fluxes and filtering capacities in a macrotidal estuary. *Journal of Marine Systems*, 78:42–58.

Arndt, S., Vanderborght, J.-P., and Regnier, P. (2007). Diatom growth response to physical forcing in a macrotidal estuary: Coupling hydrodynamics, sediment transport, and biogeochemistry. *Journal of Geophysical Research*, 112:C05045.

Ascher, U. M., Ruuth, S. J., and Spiteri, R. J. (1997). Implicit-explicit Runge-Kutta methods for time-dependent partial differential equations. *Applied Numerical Mathematics*, 25:151–167.

Baeyens, W., Elskens, M., Gillain, G., and Goeyens, L. (1998a). Biogeochemical behaviour of Cd, Cu, Pb and Zn in the Scheldt estuary during the period 1981-1983. *Hydrobiologia*, 366:15–44.

Baeyens, W., Monteny, F., Van Ryssen, R., and Leermakers, M. (1998b). A box-model of metal flows through the Scheldt estuary (1981-1983 and 1992-1995). *Hydrobiologia*, 366:109–128.

Baeyens, W., van Eck, B., Lambert, C., Wollast, R., and Goeyens, L. (1998c). General description of the Scheldt estuary. *Hydrobiologia*, 366:1–14.

Balzano, A. (1998). Evaluation of methods for numerical simulation of wetting and drying in shallow water flow models. *Coastal Engineering*, 34:83–107.

Begnudelli, L. and Sanders, B. F. (2007). Conservative wetting and drying methodology for quadrilateral grid finite-volume models. *Journal of Hydraulic Engineering*, 133:312–322.

Berx, B. and Hughes, S. L. (2009). Climatology of surface and near-bed temperature and salinity on the north-west European continental shelf for 1971-2000. *Continental Shelf Research*, 29:2286–2292.

Blaise, S., Comblen, R., Legat, V., Remacle, J.-F., Deleersnijder, E., and Lambrechts, J. (2010a). A discontinuous finite element baroclinic marine model on unstructured prismatic meshes. Part I: space discretization. *Ocean Dynamics*, 60:1371–1393.

Blaise, S., de Brye, B., de Brauwere, A., Deleersnijder, E., Delhez, E. J. M., and Comblen, R. (2010b). Capturing the residence time boundary layer - application to the Scheldt Estuary. *Ocean Dynamics*, 60:535–554.

Burchard, H., Bolding, K., and Villarreal, M. R. (2004). Three-dimensional modelling of estuarine turbidity maxima in a tidal estuary. *Ocean Dynamics*, 54:250–265.

Butcher, J. C. (1996). A history of Runge-Kutta methods. *Applied Numerical Mathematics*, 20:247–260.

Cancino, L. and Neves, R. (1999). Hydrodynamic and sediment suspension modelling in estuarine systems. Part II: Application to the Western Scheldt and Gironde estuaries. *Journal of Marine Systems*, 22:117–131.

Casulli, V. (2009). A high-resolution wetting and drying algorithm for free-surface hydrodynamics. *International Journal for Numerical Methods in Fluids*, 60:391–408.

Casulli, V. and Zanolli, P. (2002). Semi-implicit modeling of nonhydrostatic fee-surface flows for environmental problems. *Mathematical and Computer Modelling*, 36:1131–1149.

Chen, C., Liu, H., and Beardsley, R. C. (2003). An unstructured grid, finite-volume, three-dimensional, primitive equations ocean model: application to coastal ocean and estuaries. *Journal of Atmospheric and Oceanic Technology*, 20:159–186.

Chen, M. S. (2009). Particle flocculation and distribution in estuarine environment. In *Proceedings of the 33rd IAHR Congress, Water engineering for a sustainable environment*, pages 5030–5037, Vancouver, BC, Canada. International Association of Hydraulic Engineering and Research.

Chen, M. S. and Wartel, S. (2009). Estuarine hydrodynamics and energy. In Tan, S. K. and Huang, Z., editors, *Proceedings of the 5th international Conference on Asian and Pacific coasts*, volume 1, pages 216–222, Singapore.

Chen, M. S., Wartel, S., and Temmerman, S. (2005a). Seasonal variation of floc characteristics on tidal flats, the Scheldt estuary. *Hydrobiologia*, 540:181–195.

Chen, M. S., Wartel, S., van Eck, B., and van Maldegem, D. (2005b). Suspended matter in the Scheldt estuary. *Hydrobiologia*, 540:79–104.

Christian, C. D. and Palmer, G. N. (1997). A deforming finite element mesh for use in moving one-dimensional boundary wave problems. *International Journal for Numerical Methods in Fluids*, 25:407–420.

Comblen, R., Blaise, S., Legat, V., Remacle, J.-F., Deleersnijder, E., and Lambrechts, J. (2010a). A discontinuous finite element baroclinic marine model on unstructured prismatic meshes. Part II: implicit/explicit time discretization. *Ocean Dynamics*, 60:1395–1414.

Comblen, R., Lambrechts, J., Remacle, J.-F., and Legat, V. (2010b). Practical evaluation of five partly discontinuous finite element pairs for the non-conservative shallow water equations. *International Journal for Numerical Methods in Fluids*, 63:701–724.

Cushman-Roisin, B. (1994). *Introduction to geophysical fluid dynamics*. Prentice Hall.

Danilov, S., Kivman, G., and Schröter, J. (2005). Evaluation of an eddy-permitting finite-element ocean model in the North Atlantic. *Ocean Modelling*, 10:35–49.

Dawson, C. and Aizinger, V. (2005). A discontinuous Galerkin method for three-dimensional shallow water equations. *Journal of Scientific Computing*, 22-23:245–267.

de Brauwere, A., de Brye, B., Blaise, S., and Deleersnijder, E. (2011a). Residence time, exposure time and connectivity in the Scheldt Estuary. *Journal of Marine Systems*, 84:85–95.

de Brauwere, A., de Brye, B., Servais, P., Passerat, J., and Deleersnijder, E. (2011b). Modelling *Escherichia coli* concentrations in the tidal Scheldt river and estuary. *Water Research*, 45:2724–2738.

de Brauwere, A., De Ridder, F., Gourgue, O., Lambrechts, J., Comblen, R., Pintelon, R., Passerat, J., Servais, P., Elskens, M., Baeyens, W., Kärnä, T., de Brye, B., and Deleersnijder, E. (2009). Design of a sampling strategy to optimally calibrate a reactive transport model: Exploring the potential for *Escherichia coli* in the Scheldt Estuary. *Environmental Modelling & Software*, 24:969–981.

de Brauwere, A., Gourgue, O., de Brye, B., Servais, P., Ouattara, N. K., and Deleersnijder, E. (2011c). Modelling *Escherichia coli* dynamics in the Scheldt land-sea continuum. Part II. The tidal Scheldt River and Estuary. *Journal of Marine Systems*, in preparation.

de Brye, B., de Brauwere, A., Gourgue, O., Delhez, E. J. M., and Deleersnijder, E. (2011a). Water renewal timescales in the Scheldt Estuary. *Journal of Marine Systems*, accepted for publication.

de Brye, B., de Brauwere, A., Gourgue, O., Kärnä, T., Lambrechts, J., Comblen, R., and Deleersnijder, E. (2010). A finite-element, multi-scale model of the Scheldt tributaries, river, estuary and ROFI. *Coastal Engineering*, 57:850–863.

de Brye, B., Schellen, S., Sassi, M. G., Vermeulen, B., Kärnä, T., Deleersnijder, E., and Hoitink, A. J. F. (2011b). Preliminary results of a finite-element, multi-scale model of the Mahakam Delta (Indonesia). *Ocean Dynamics*, 61:1197–1120.

De Smedt, F., Vuksanovic, V., Van Meerbeeck, S., and Reyns, D. (1998). A time-dependent flow model for heavy metals in the Scheldt estuary. *Hydrobiologia*, 366:143–155.

Delhez, E. J. M. and Wolk, F. (2011). Diagnosis of the transport of adsorbed material in the Scheldt estuary. *Journal of Marine Systems*, submitted.

Egbert, G. D., Bennett, F., and Foreman, M. G. G. (1994). TOPEX/POSEIDON tides estimated using a global inverse model. *Journal of Geophysical Research*, 99(C12):24821–24852.

Einstein, H. A. and Krone, R. B. (1962). Experiments to determine modes of cohesive sediment transport in salt water. *Journal of Geophysical Research*, 67:1451–1461.

Ern, A., Piperno, S., and Djadel, K. (2008). A well-balanced Runge-Kutta discontinuous Galerkin method for the shallow-water equations with flooding and drying. *International Journal for Numerical Methods in Fluids*, 58:1–25.

Ertürk, Ş. N., Bilgili, A., Swift, M. R., Brown, W. S., Çelikkol, B., Ip, J. T. C., and Lynch, D. R. (2002). Simulation of the Great Bay Estuarine Sytem: tides with tidal flats wetting and drying. *Journal of Geophysical Research*, 107:C5 3038.

Fettweis, M., Sas, M., and Monbaliu, J. (1998). Seasonal, neap-string and tidal variation of cohesive sediment concentration in the Scheldt Estuary, Belgium. *Estuarine, Coastal and Shelf Science*, 47:21–36.

Fettweis, M. and Van den Eynde, D. (2003). The mud deposits and the high turbidity in the Belgian-Dutch coastal zone, southern bight of the North Sea. *Continental Shelf Research*, 23:669–691.

Fringer, O. B., Gerritsen, M., and Street, R. L. (2006). An unstructured-grid, finite-volume, nonhydrostatic, parallel coastal ocean simulator. *Ocean Modelling*, 14:139–173.

Garcia, M. H., editor (2006). *Sedimentation engineering*. Number 110 in Manuals and Reports on Engineering Practice. American Society of Civil Engineers.

Geuzaine, C. and Remacle, J.-F. (2009). Gmsh: a 3-D finite element mesh generator with built-in pre- and post-processing facilities. *International Journal for Numerical Methods in Engineering*, 79:1309–1331.

Gourgue, O., Baeyens, W., Chen, M., de Brauwere, A., de Brye, B., Deleersnijder, E., Elskens, M., and Legat, V. (2011a). A depth-averaged sediment transport model for environmental studies in the Scheldt Estuary and tidal river network. *Journal of Marine Systems*, submitted.

Gourgue, O., Comblen, R., Lambrechts, J., Kärnä, T., Legat, V., and Deleersnijder, E. (2009). A flux-limiting wetting-drying method for finite-element shallow-water models, with application to the Scheldt Estuary. *Advances in Water Resources*, 32:1726–1739.

Gourgue, O., Deleersnijder, E., Legat, V., Marchal, E., and White, L. (2011b). Free and forced thermocline oscillations in Lake Tanganyika. In Alpert, P. and Sholokhman, T., editors, *Factor separation in the atmosphere: applications and future prospects*, chapter 9, pages 146–162. Cambridge University Press.

Gourgue, O., Deleersnijder, E., and White, L. (2007). Toward a generic method for studying water renewal, with application to the epilimnion of Lake Tanganyika. *Estuarine, Coastal and Shelf Science*, 74:628–640.

Graf, W. H. and Altinakar, M. S. (1993). *Hydraulique fluviale*, volume 16 of *Traité de Génie Civil de l'Ecole polytechnique fédérale de Lausanne*. Presses polytechniques et universitaires romandes.

Griffies, S. M., Böning, C., Bryan, F. O., Chassignet, E. P., Gerdes, R., Hasumi, H., Hirst, A., Treguier, A.-M., and Webb, D. (2000). Developments in ocean climate modelling. *Ocean Modelling*, 2:123–192.

Haidvogel, D. B., McWilliams, J. C., and Gent, P. R. (1991). Boundary current separation in a quasigeostrophic, eddy-resolving ocean circulation model. *Journal of Physical Oceanography*, 22:882–902.

Ham, D. A., Pietrzak, J., and Stelling, G. S. (2005). A scalable unstructured grid 3-dimensional finite volume model for the shallow water equations. *Ocean Modelling*, 10:153–169.

Hanert, E., Legat, V., and Deleersnijder, E. (2002). A comparison of three finite elements to solve the linear shallow water equations. *Ocean Modelling*, 5:17–35.

Hanert, E., Roux, D. Y. L., Legat, V., and Deleersnijder, E. (2004). Advection schemes for unstructured grid ocean modelling. *Ocean Modelling*, 7:39–58.

Hanert, E., Roux, D. Y. L., Legat, V., and Deleersnijder, E. (2005). An efficient Eulerian finite element method for the shallow water equations. *Ocean Modelling*, 10:115–136.

Heniche, M., Secretan, Y., Boudreau, P., and Leclerc, M. (2000). A two-dimensional finite element drying-wetting shallow water model for rivers and estuaries. *Advances in Water Resources*, 23:359–372.

Ip, J. T. C., Lynch, D. R., and Friedrichs, C. T. (1998). Simulation of estuarine flooding and dewatering with application to Great Bay, New Hampshire. *Estuarine, Coastal and Shelf Science*, 47:119–141.

Ji, Z.-G., Morton, M. R., and Hamrick, J. M. (2001). Wetting and drying simulation of estuarine processes. *Estuarine, Coastal and Shelf Science*, 53:683–700.

Jiang, Y. W. and Wai, O. W. H. (2005). Drying-wetting approach for 3D finite element sigma coordinate model for estuaries with large tidal flats. *Advances in Water Resources*, 28:779–792.

Kalnay, E., Kanamitsu, M., Kistler, R., Collins, W., Deaven, D., Gandin, L., Iredell, M., Saha, S., White, G., Woollen, J., Zhu, Y., Chelliah, M., Ebisuzaki, W., Higgins, W., Janowiak, J., Mo, K. C., Ropelewski, C., Wang, J., Leetmaa, A., Reynolds, R., Jenne, R., and Joseph, D. (1996). The NCEP/NCAR 40-year reanalysis project. *Bulletin of the American Meteorological Society*, 77:437–471.

Kärnä, T., de Brye, B., Gourgue, O., Lambrechts, J., Comblen, R., Legat, V., and Deleersnijder, E. (2011a). A fully implicit wetting-drying method for DG-FEM shallow water models, with an application to the Scheldt Estuary. *Computer Methods in Applied Mechanics and Engineering*, 200:509–524.

Kärnä, T., Legat, V., Deleersnijder, E., and Burchard, H. (2011b). Coupling of a discontinuous Galerkin finite element marine modem with a finite difference turbulence closure model. *Ocean Modelling*, submitted.

Kubatko, E. J., Westerink, J. J., and Dawson, C. (2006). *hp* discontinuous Galerkin methods for advection dominated problems in shallow water flow. *Computer Methods in Applied Mechanics and Engineering*, 196:437–451.

Kundu, P. K. and Cohen, I. M. (2002). *Fluid mechanics*. Academic Press, second edition.

Lambrechts, J., Comblen, R., Legat, V., Geuzaine, C., and Remacle, J.-F. (2008a). Multiscale mesh generation on the sphere. *Ocean Dynamics*, 58:461–473.

Lambrechts, J., Hanert, E., Deleersnijder, E., Bernard, P.-E., Legat, V., Remacle, J.-F., and Wolanski, E. (2008b). A multi-scale model of the hydrodynamics of the whole Great Barrier Reef. *Estuarine, Coastal and Shelf Science*, 79:143–151.

Lambrechts, J., Humphrey, C., McKinna, L., Gourgue, O., Fabricius, K. E., Mehta, A. J., Lewis, S., and Wolanski, E. (2010). Importance of wave-induced bed liquefaction in the fine sediment budget of Cleveland Bay, Great Barrier Reef. *Estuarine, Coastal and Shelf Science*, 89:154–162.

Le Bars, Y., Lyard, F., Jeandel, C., and Dardengo, L. (2010). The AMANDES tidal model for the Amazon estuary and shelf. *Ocean Modelling*, 31:132–149.

Leclerc, M., Bellemare, J.-F., Dumas, G., and Dhatt, G. (1990). A finite element model of estuarian and river flows with moving boundaries. *Advances in Water Resources*, 13:158–168.

Leendertse, J. J. (1970). *Principles of computation*, volume 1 of *A water-quality simulation model for well-mixed estuaries and coastal seas*. The Rand Corporation.

Lin, B. and Falconer, R. A. (1997). Three-dimensional layer-integrated modelling of estuarine flows with flooding and drying. *Estuarine, Coastal and Shelf Science*, 44:737–751.

Lynch, D. R. and Gray, W. G. (1980). Finite element simulation of flow in deforming regions. *Journal of Computational Physics*, 36:135–153.

Majander, P. and Siikonen, T. (2002). Evaluation of Smagorinsky-based subgrid-scale models in a finite-volume computation. *International Journal for Numerical Methods in Fluids*, 40:735–774.

Manning, A. J., Langston, W. J., and Jonas, P. J. C. (2010). A review of sediment dynamics in the Severn Estuary: influence of flocculation. *Marine Pollution Bulletin*, 61:37–51.

Manning, A. J., van Kessel, T., Melotte, J., Sas, M., Winterwerp, H., and Pidduck, E. L. (2011). On the consequence of a new tidal dock on the sedimentation regime in the Antwerpen area of the Lower Sea Scheldt. *Continental Shelf Research*, 31:S150–S164.

Maßmann, S., Androsov, A., and Danilov, S. (2010). Intercomparison between finite element and finite volume approaches to model North Sea tides. *Continental Shelf Research*, 30:680–691.

Mercier, C. and Delhez, E. J. M. (2007). Diagnosis of the sediment transport in the Belgian Coastal Zone. *Estuarine, Coastal and Shelf Science*, 74:670–683.

Mietta, F., Chassagne, C., Manning, A. J., and Winterwerp, J. C. (2009). Influence of shear rate, organic matter content, pH and salinity on mud flocculation. *Ocean Dynamics*, 59:751–763.

Mwanuzi, F. and De Smedt, F. (1999). Heavy metal distribution model under estuarine mixing. *Hydrological processes*, 13:789–804.

Nielsen, C. and Apelt, C. (2003). Parameters affecting the performance of wetting and drying in a two-dimensional finite element long wave hydrodynamic model. *Journal of Hydraulic Engineering*, 129:628–636.

Oey, L.-Y. (2006). An OGCM with movable land-sea boundaries. *Ocean Modelling*, 13:176–195.

Okubo, A. (1971). Oceanic diffusion diagrams. *Deep-Sea Research*, 18:789–802.

Otto, L., Zimmerman, J. T. F., Furnes, G. K., Mork, M., Saetre, R., and Becker, G. (1990). Review of the physical oceanography of the North Sea. *Netherlands Journal of Sea Research*, 26:161–238.

Ouboter, M. R. L., van Eck, B. T. M., J. A. G. Van Gils, J.-P. S., and Villars, M. T. (1998). Water quality modelling of the western Scheldt estuary. *Hydrobiologia*, 366:129–142.

Partheniades, E. (1965). Erosion and deposition of cohesive soils. *Journal of the Hydraulics Division*, 91:105–139.

Pejrup, M. and Mikkelsen, O. (2010). Factors controlling the field settling velocity of cohesive sediment in estuaries. *Estuarine, Coastal and Shelf Science*, 87:177–185.

Piggott, M. D., Gorman, G. J., Pain, C. C., Allison, P. A., Candy, A. S., Martin, B. T., and Wells, M. R. (2008). A new computational framework for multi-scale ocean modelling based on adapting unstructured meshes. *International Journal for Numerical Methods in Fluids*, 56:1003–1015.

Prasad, R. S. and Svendsen, I. A. (2003). Moving shoreline boundary condition for nearshore models. *Coastal Engineering*, 49:239–261.

Proudman, J. and Doodson, A. T. (1924). The principal constituent of the tides of the North Sea. *Philosophical Transactions of the Royal Society of London A*, 224:185–219.

Remacle, J.-F., Lambrechts, J., Seny, B., Marchandise, E., Johnen, A., and Geuzaine, C. (2010). Blossom-Quad: a non-uniform quadrilateral mesh generator using a minimum cost perfect matching algorithm. *International Journal for Numerical Methods in Engineering*, submitted.

Shahbazi, K. (2005). An explicit expression for the penalty parameter of the interior penalty method. *Journal of Computational Physics*, 205:401–407.

Shchepetkin, A. F. and O'Brien, J. J. (1996). A physically consistent formulation of lateral friction in shallow-water equation ocean models. *Monthly Weather Review*, 124:1285–1300.

Sielecki, A. and Wurtele, M. G. (1970). The numerical integration of the nonlinear shallow-water equations with sloping boundaries. *Journal of Computational Physics*, 6:219–236.

Sinha, B. and Pingree, R. D. (1997). The principal lunar semidiurnal tide and its harmonics: baseline solutions for M_2 and M_4 constituents on the North-West European Continental Shelf. *Continental Shelf Research*, 17:1321–1365.

Smagorinsky, J. (1963). General circulation experiments with the primitive equations. I. The basic experiments. *Monthly Weather Review*, 91:99–164.

Smith, S. D. and Banke, E. G. (1975). Variation of the sea surface drag coefficient with wind speed. *Quarterly Journal of the Royal Meteorological Society*, 101:665–673.

Soetaert, K. and Herman, P. M. J. (1995). Estimating estuarine residence time in the Westerschelde (The Netherlands) using a box model with fixed dispersion coefficients. *Hydrobiologia*, 311:215–224.

Soetaert, K., Middelburg, J. J., Heip, C., Meire, P., Van Damme, S., and Maris, T. (2006). Long-term change in dissolved inorganic nutrients in the heterotrophic Scheldt estuary (Belgium, The Netherlands). *Limnology and Oceanography*, 51:409–423.

Speziale, C. G. (1991). Analytical methods for the development of Reynolds-stress closures in turbulence. *Annual Review of Fluid Mechanics*, 23:107–157.

Steen, R. J. C. A., Evers, E. H. G., Van Hattum, B., Van Hattum, W. P., Cofino, W. P., and Brinkman, U. A. T. (2002). Net fluxes of pesticides from the Scheldt Estuary into the North Sea: a model approach. *Environmental Pollution*, 116:75–84.

Stolzenbach, K. D., Newman, K. A., and Wong, C. S. (1992). Aggregation of fine particles at the sediment-water interface. *Journal of Geophysical Research*, 97(C11):17889–17898.

Tao, J., Li, Q., Falconer, R. A., and Lin, B. (2001). Modelling and assessment of water quality indicators in a semi-enclosed shallow bay. *Journal of Hydraulic Research*, 39:611–617.

Thacker, W. C. (1981). Some exact solutions to the nonlinear shallow-water wave equations. *Journal of Fluid Mechanics*, 107:499–508.

Thieu, V., Billen, G., and Garnier, J. (2009). Nutrient transfer in three contrasting NW European watersheds: The Seine, Somme and Scheldt Rivers. A comparative application of the Seneque/Riverstrahler model. *Water Research*, 43:1740–1754.

Timmermann, R., Danilov, S., Schröter, J., Böning, C., Sidorenko, D., and Rollenhagen, K. (2009). Ocean circulation and sea ice distribution in a finite element global sea ice-ocean model. *Ocean Modelling*, 27:114–129.

van der Wal, D., van Kessel, T., Eleveld, M. A., and Vanlede, J. (2010). Spatial heterogeneity in estuarine mud dynamics. *Ocean Dynamics*, 60:519–533.

van Kessel, T., Vanlede, J., and de Kok, J. (2011). Development of a mud transport model for the Scheldt estuary. *Continental Shelf Research*, 31:S165–S181.

van Leussen, W. (1999). The variability of settling velocities of suspended fine-grained sediment in the Ems estuary. *Journal of Sea Research*, 41:109–118.

Vanderborght, J.-P., Folmer, I. M., Aguilera, D. R., Uhrenholdt, T., and Regnier, P. (2007). Reactive-transport modelling of C, N, and O_2 in a river-estuarine-coastal zone system: application to the Scheldt estuary. *Marine Chemistry*, 106:92–110.

Vanderborght, J.-P., Wollast, R., Loijens, M., and Regnier, P. (2002). Application of a transport-reaction model to the estimation of biogas fluxes in the Scheldt estuary. *Biogeochemistry*, 59:207–237.

Villars, M. T. and Vos, R. J. (1999). RESTWES: remote sensing as a tool for integrated monitoring of the Western Scheldt. WL Delft Hydraulics Report Z2472, Delft Hydraulics.

Vreugdenhil, C. B. (1994). *Numerical methods for shallow-water flow*, volume 13 of *Water Science and Technology Library*. Kluwer Academic Publishers.

Vuksanovic, V., De Smedt, F., and Van Meerbeeck, S. (1996). Transport of polychlorinated biphenyls (PCB) in the Scheldt Estuary simulated with the water uality model WASP. *Journal of Hydrology*, 174:1–18.

Walters, R. A. (2005). Coastal ocean models: two useful finite element methods. *Continental Shelf Research*, 25:775–793.

Walters, R. A. (2006). Design considerations for a finite element coastal ocean model. *Ocean Modelling*, 15:90–100.

Wang, Q., Danilov, S., and Schröter, J. (2009). Bottom water formation in the southern Weddell Sea and the influence of submarine ridges: Idealized numerical simulations. *Ocean Modelling*, 28:50–59.

White, L., Deleersnijder, E., and Legat, V. (2008a). A three-dimensional unstructured mesh finite element shallow-water model, with application to the flows around an island and in a wind-driven, elongated basin. *Ocean Modelling*, 22:26–47.

White, L., Legat, V., and Deleersnijder, E. (2008b). Tracer conservation for three-dimensional, finite-element, free-surface, ocean modeling on moving prismatic meshes. *Monthly Weather Review*, 136:420–442.

Winterwerp, J. C. (2002). On the flocculation and settling velocity of estuarine mud. *Continental Shelf Research*, 22:1339–1360.

Wolanski, E. (1995). Transport of sediment in mangrove swamps. *Hydrobiologia*, 295:31–42.

Wolanski, E. (2007). *Estuarine ecohydrology*. Elsevier.

Wu, Y., Falconer, R., and Lin, B. (2005). Modelling trace metal concentration distributions in estuarine waters. *Estuarine, Coastal and Shelf Science*, 64:699–709.

Xia, X. M., Li, Y., Yang, H., Wu, C. Y., Sing, T. H., and Pong, H. K. (2004). Observations on the size and settling velocity distributions of suspended sediment in the Pearl River Estuary, China. *Continental Shelf Research*, 24:1809–1826.

Yuan, D., Lin, B., and Falconer, R. (2008). Simulating moving boundary using a linked groundwater and surface water flow model. *Journal of Hydrology*, 349:524–535.

Zheng, L., Chen, C., and Liu, H. (2003). A modeling study of the Satilla River Estuary, Georgia. I: flooding-drying process and water exchange over the salt marsh-estuary-shelf complex. *Estuaries*, 26:651–669.